

**EXCEPTIONAL POINTS AND THEIR CONSEQUENCES IN
OPEN, MINIMAL QUANTUM SYSTEMS.**

by

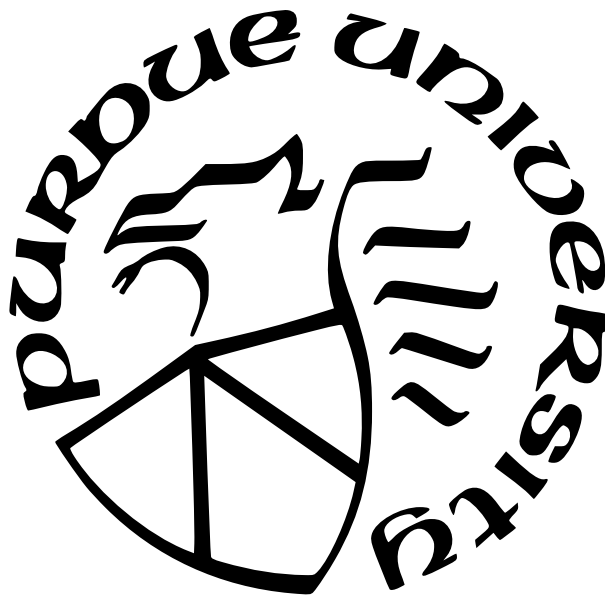
Jacob E. Muldoon

A Dissertation

Submitted to the Faculty of Purdue University

In Partial Fulfillment of the Requirements for the degree of

Doctor of Philosophy



Department of Physics

Indianapolis, Indiana

August 2022

**THE PURDUE UNIVERSITY GRADUATE SCHOOL
STATEMENT OF COMMITTEE APPROVAL**

Dr. Yogesh Joglekar, Chair

Department of Physics

Dr. Ricardo Decca

Department of Physics

Dr. Rui Cheng

Department of Physics

Dr. Gautam Vemuri

Department of Physics

Dr. Lukasz Cincio

Los Alamos National Laboratory

Approved by:

Dr. Horia Petrache

TABLE OF CONTENTS

LIST OF TABLES	6
LIST OF FIGURES	7
ABSTRACT	12
1 INTRODUCTION TO NON-HERMITIAN PHYSICS	13
1.1 Background and Terminology	13
1.2 Construction of Quantum Mechanics	15
1.2.1 Consequences of Non-Hermiticity	16
1.2.2 Degrees of Non-Hermiticity	18
\mathcal{PT} -Symmetry	19
Pseudo-Hermiticity and Quasi-Hermiticity	20
Passive \mathcal{PT} Systems	22
1.3 Fundamental Case: \mathcal{PT} -Dimer	23
1.4 Floquet Analysis for Non-Hermitian Physics	31
1.5 Physical Questions	32
2 OPEN QUANTUM MAPS	34
2.1 Quantum Maps	34
2.1.1 Operator Sum Representation	35
2.1.2 Vectorized Representation	36
2.1.3 Choi Representation	38
2.2 Kraus Maps	39
2.2.1 Markovianity	40
2.2.2 Lindblad Master Equation	42
2.3 Fundamental Case: Decohering Dimer	44
2.4 Floquet Analysis for Quantum Maps	48
2.4.1 Floquet Lindbladians with Periodic Potentials	51
2.4.2 Floquet Lindbladians with Periodic Dissipators	58

3	EXPERIMENTAL PLATFORM: CAVITY-COUPLED TRANSMON CIRCUITS	62
3.1	Quantization of the Transmon Circuit	62
3.1.1	Capacitors	63
3.1.2	Josephson Junctions	64
3.1.3	Deriving the Transmon Hamiltonian	65
3.2	Quantization of the Cavity	69
3.2.1	Maxwell's Equations	69
3.2.2	Deriving the Cavity Hamiltonian	70
3.3	Cavity-Circuit Interaction	71
3.3.1	Rotating Wave Approximation	72
3.4	Measuring Dissipation	73
3.4.1	Spontaneous Emission	74
3.4.2	Phase Noise	74
4	CONNECTING NON-HERMITIAN PHYSICS TO QUANTUM MAPS	76
4.1	Master Equations for Non-Hermitian Hamiltonians	76
4.1.1	The Renormalized Master Equation	79
4.2	Pseudo-Hermiticity from Vectorization	80
4.2.1	Intertwining Operators for Periodic Systems	81
4.3	Postselection of the Lindbladian	84
4.3.1	Transmon Qutrit Experimental Procedure	87
4.4	Comparing \mathcal{PT} -Symmetric and Lindbladian Behavior	88
4.4.1	Measurement with respect to an External Basis: Leggett-Garg Inequality	90
4.4.2	Measurement with respect to a Non-Orthogonal Basis: Jarzynski Equality	97
5	SUMMARY	104
	REFERENCES	105
A	PARTIAL TRACE OPERATION	109

VITA 111

LIST OF TABLES

1.1	Table comparing the effects of the operators \mathcal{P} , \mathcal{T} , and \mathcal{PT} on physically relevant quantities. \mathcal{P} negates vectors while leaving bi-vectors unchanged. \mathcal{T} negates fields sourced by a current.	20
2.1	Table comparing the useful properties of each of the representations of the quantum map \mathcal{M}	39

LIST OF FIGURES

- 1.1 **\mathcal{PT} -Dimer:** Illustrations commonly used for a \mathcal{PT} -symmetric, two level system. Figure 1.1a shows the cross-section of a system of two waveguides, where J is the evanescent coupling, and $\eta_{\pm} = \mu \pm i\gamma$ are the (complex) refractive indices for the two waveguides [4]. Figure 1.1b shows an energy level diagram for a driven two level atom (denoted by the dashed line box), where $\frac{J}{2}$ is a microwave drive, Δ is the energy level difference between $|f\rangle$ and $|e\rangle$, and γ is the decay rate of $|e\rangle$ into an auxiliary state [6], [15]. The Hamiltonians are provided below each model, and are an identity shift away from H_2 24
- 1.2 ϵ_{\pm} **when $\Delta = 0$:** Shows the energies ϵ_{\pm} as $\frac{\gamma}{J}$ is varied from $[0, 2]$. Fig.1.2a shows the real part in (blue), while the imaginary part is shown in (red). The presence of an exceptional point can clearly be seen at $\frac{\gamma}{J} = 1$, at which point ϵ_{\pm} and $|\epsilon_{\pm}\rangle$ are degenerate. Fig.1.2b shows $\langle\epsilon_+|\epsilon_-\rangle$ as a measure of non-orthogonality. We observe a linear increase in the overlap until reaching $\langle\epsilon_+|\epsilon_-\rangle = 1$ at the exceptional point, after which the overlap decays as $\frac{J}{\gamma}$ 25
- 1.3 **Progression of States:** Depiction of a Bloch sphere formed by $|\uparrow\rangle$ and $|\downarrow\rangle$ as H_2 varies from $\frac{\gamma}{J} \in [0, 10]$. Fig.1.3a shows points for $\frac{\Delta}{J} = 0$, while Fig.1.3b shows points for $\frac{\Delta}{J} = 0.25$. The spacing between points is $\frac{\gamma}{J} = 0.1$. At the Hermitian limit (black), the $|\epsilon_{\pm}\rangle$ are orthogonal at opposite points of the Bloch sphere aligned on the x -axis. For Fig.1.3a, as γ is increased in the \mathcal{PT} -symmetric phase (blue), the $|\epsilon_{\pm}\rangle$ approach $|\downarrow\rangle_y = [1 \quad -i]^T$ while $\langle\epsilon_+|\epsilon_-\rangle \rightarrow 1$, finally becoming degenerate at $\frac{\gamma}{J} = 1$. After passing the exceptional point (red), the $|\epsilon_{\pm}\rangle$ asymptotically approach $|\uparrow\rangle$, where at $\frac{\gamma}{J} = \infty$ they become orthogonal once more. For Fig.1.3b, H_2 is always in the \mathcal{PT} -broken phase except at the Hermitian limit (the regions of $\frac{\gamma}{J} \leq 1$ and $\frac{\gamma}{J} \geq 1$ are denoted with the same colors as before). The corresponding $|\epsilon_{\pm}\rangle$ (cyan and magenta) always exist in the direction opposite to their conjugate counterpart $|\epsilon_{\mp}\rangle$, but due to the normalization $\langle\langle\epsilon_i|\epsilon_j\rangle\rangle = \delta_{ij}$ are not bound to the Bloch sphere. Their projections onto the Bloch sphere are plotted in faded colors. 28
- 1.4 ϵ **Surface:** Shows the energies ϵ_{\pm} as $\frac{J}{\gamma}$ is varied from $[0, 2]$ and $\frac{\Delta}{\gamma}$ is varied from $[-2, 2]$. Fig.1.4a shows the real part, while Fig.1.4b shows the imaginary part. The presence of an exceptional point can again be seen at $\frac{\Delta}{\gamma} = 0, \frac{J}{\gamma} = 1$. Fig.1.2c shows $\langle\epsilon_+|\epsilon_-\rangle$ reaching $\langle\epsilon_+|\epsilon_-\rangle = 1$ at the exceptional point. 30
- 2.1 **Decohering Dimer:** Shows an energy level diagram for a decohering two level transmon, where $\frac{J}{2}$ is a microwave drive and Δ is the energy level difference between $|\uparrow\rangle$ and $|\downarrow\rangle$. There are 3 forms of dissipation present in the model consisting of spontaneous emission (γ_-), spontaneous absorption (γ_+), and phase noise (γ_z). Unlike in Fig.1.1b the dissipation of the Decohering Dimer is internal to the two level manifold, and thus the effects of decoherent jumps remain present [15]. 45

- 2.2 **Decohering Dimer Eigenvalues:** Shows the eigenvalue spectrum for a Decohering Dimer with $\gamma_z = .25$, $\gamma_+ = .75$, $\gamma_- = .5$ and varying J . Figure 2.2 shows the position of λ_j in the complex plane, while Figure 2.2b shows the eigenvalues of $\mathcal{V}_2 (e^{\lambda_j t})$ when $t = 1$. The region of the complex plane that the eigenvalues cannot exist in is shaded gray. The steady state $\lambda_{ss} = 0$ is marked in black. $\lambda_0 = -\frac{\gamma_+ + \gamma_- + \gamma_z}{2}$ is marked in red. The remaining pair λ_{\pm} is marked with the color gradient blue→yellow. λ_+ and λ_- initially lie on the real axis, but become degenerate at $\left| \frac{2J}{\lambda_0 + \gamma_z} \right| = 1$ after which they form a complex conjugate pair. The corresponding $e^{\lambda_+ t}$ and $e^{\lambda_- t}$ wind around the origin, but do not become degenerate at larger J . The non-orthogonal character of the ρ_j is tracked in Figure 2.2c. 47
- 2.3 **Evolution of the Decohering Dimer:** Shows the evolution of the state density $\rho(0) = |\uparrow\rangle\langle\uparrow|$ under \mathcal{L}_2 when $\gamma_z = 6$, $\gamma_+ = 1$, $\gamma_- = 1$, and $J = 1$. The outline of the Bloch sphere is shown with a transparent gradient. The steady state the system approaches at $t \rightarrow \infty$ is the maximally mixed state, shown here as the black dot at the center of the Bloch Sphere. As t increases $\mathcal{V}_2 |\rho(0)\rangle$ is traced using the color gradient line. The specific combination of coupling strength and decay rates means that \mathcal{L}_2 is critically damped, meaning that $\lambda_+ = \lambda_-$ and $\rho(t)$ will approach ρ_{ss} as fast as possible for the given γ_{μ} 49
- 2.4 **Periodic Driving with L_- Phase Diagram:** Shows the maximum inner product of eigen-densities $\max(\langle\rho_{F_i}|\rho_{F_j}\rangle)$ for periodic driving $J(t)$ and spontaneous emission rate γ with $\delta = 1$. Figure 2.4a shows the sinusoidal modulation, while Figure 2.4b shows the square wave modulation. The presence of exceptional point contours is clearly seen in both cases. We see that all of the contours converge at the point $\left(\frac{\Omega}{J}, \frac{\gamma}{J}\right) = (0, 4)$, which corresponds to the exceptional point of the static system \mathcal{L}_2 . We also see that there is a contour which approaches $\left(\frac{\Omega}{J}, \frac{\gamma}{J}\right) = (\infty, 2)$, which corresponds to the same exceptional point of \mathcal{L}_2 in the high frequency regime where the motion is averaged out. The rest of the contours converge toward the unitary limit as pairs symmetrically approaching the points $\left(\frac{\Omega}{J}, \frac{\gamma}{J}\right) = \left(\frac{1}{n}, 0\right)$ 53
- 2.5 **Evolution of Eigenvalues for V_F :** Shows the evolution of the eigenvalues of \mathcal{V}_{F-} as $\frac{\Omega}{J}$ increases from $0.2 \rightarrow 2$. The center of the allowed complex disk is marked by the black dot. The path traced through the phase diagram in Figure 2.5a is marked by the dashed line, while the evolution along the path is denoted by the gradient line in Figure 2.5b. 55

2.6	Periodic Driving with L_z Phase Diagram:	Shows the maximum inner product of eigen-densities $\max(\langle \rho_{Fi} \rho_{Fj} \rangle)$ for periodic driving $J(t)$ and phase noise rate γ with $\delta = 1$. Figure 2.6a shows the sinusoidal modulation, while Figure 2.6b shows the square wave modulation. Most of the properties of the phase diagram are the same as Figure 2.4, with identical limits on the exceptional point contours. The major difference lies in the degree of non-orthogonality in the overdamped regions. Here we see the system reach $\max(\langle \rho_{Fi} \rho_{Fj} \rangle) = 0$ within the overdamped region, signifying that all ρ_{Fj} have become orthogonal. These “maximally-orthogonal” contours extend all the way up to the static exceptional point at $(\frac{\Omega}{J}, \frac{\gamma}{J}) = (0, 4)$	57
2.7	Periodic Dissipation Phase Diagrams:	Shows the maximum inner product of eigen-densities $\max(\langle \rho_{Fi} \rho_{Fj} \rangle)$ for periodic dissipations $\gamma_-(t)$ and $\gamma_z(t)$ with $\delta = 1$. Figure 2.6a shows the sinusoidal modulation with $L_-(t)$, while Figure 2.6b shows the square wave modulation with $L_-(t)$. Figure 2.6c shows the sinusoidal modulation with $L_z(t)$, while Figure 2.6d shows the square wave modulation with $L_z(t)$. Both the exceptional point contours as well as the maximally-orthogonal contours continue on toward $\frac{\gamma}{J}$. The exceptional contours no longer converge on the static exceptional point, instead the widest point of each curve traces a path toward $(\frac{\Omega}{J}, \frac{\gamma}{J}) = (0, 4)$. In Figure 2.7d we see the result of this continuation causes the contour sets to cross over each other, forming a grid of small underdamped and overdamped regions.	59
2.8	Resonances $L_z(t)$ Phase Diagram:	Shows a close up of Figure 2.7d. We see that some of the exceptional point lines reach all the way to the unitary limit, while others fade into the underdamped region.	61
3.1	Transmon Schematic:	Circuit diagram for a transmon, consisting of a Josephson junction L_J that has been shunted by a capacitor C	63
3.2	Transmon Potential Approximations:	Shows the various potential approximations in Eq.3.12 when $\frac{E_J}{8E_C} = 16$. The proper potential Eq.3.12a is shown in black. The harmonic potential Eq.3.12b is shown in blue. The anharmonic potential Eq.3.12c is shown in red. In addition, the first four energy levels are plotted for the harmonic and anharmonic oscillators, with blue dashes for the harmonic oscillator, and red dots for the anharmonic oscillator. We see that the energy levels of the harmonic oscillator are evenly spaced, while the energy levels of the anharmonic oscillator are unevenly distributed. This unevenness allows us to drive specific pairs of levels when coupled to the cavity.	67

4.1	<p>Intertwining Operators and Eigen-Measurements of Square Wave: Shows the expectation values $\langle Q_j \rangle$ for the four eigen-measurements of $\mathcal{H}_2(t)$ under square wave modulation with $\frac{\gamma}{J} = 0.5$, $JT = 1$, and $\rho(0) = \uparrow\rangle\langle\uparrow$. Figure 4.1a shows η_1, Figure 4.1b shows η_2, Figure 4.1c shows Q_3, and Figure 4.1d shows Q_4. In each figure, the solid line shows the real-time value of $\langle Q_j \rangle$, while the dashed line shows the trend predicted by $e^{\lambda_{F_j} T}$. We see that at stroboscopic points the two trends converge in all four figures, while only η_1 is a constant of motion at all times.</p>	83
4.2	<p>Intertwining Operators and Eigen-Measurements of Kicked Potential: Shows the expectation values $\langle Q_j \rangle$ for the four eigen-measurements of $\mathcal{H}_2(t)$ under non-Hermitian δ potential kicks with $\frac{\gamma}{J} = 0.5$, $JT = 1$, and $\rho(0) = \uparrow\rangle\langle\uparrow$. Figure 4.2a shows η_1, Figure 4.2b shows η_2, Figure 4.2c shows Q_3, and Figure 4.2d shows Q_4. In each figure, the solid line shows the real-time value of $\langle Q_j \rangle$, while the dashed line shows the trend predicted by $e^{\lambda_{F_j} T}$. We see that at stroboscopic points the two trends converge in all four figures, while only η_1 is a constant of motion at all times.</p>	85
4.3	<p>Transmon Qutrit Postselection Scheme: Illustration depicting a ideal transmon qutrit. The system consists of three energy levels with unequal spacing, allowing the excited states $f\rangle$ and $e\rangle$ to be driven independent of the ground state $g\rangle$. The ideal system has only one Lindblad dissipator of the form $L_{ge} = g\rangle\langle e$, allowing the detection of quantum jumps simply by non-zero measurement of $g\rangle$.</p>	86
4.4	<p>Equivalence of Renormalized Non-Hermitian Hamiltonian and Postselected Lindbladian Evolutions: Phase Diagrams comparing the renormalized Liouvillian evolved $\tilde{\rho}$ (Figure 4.4a,d,g) vs the postselected Lindbladian evolved $\bar{\rho}$ (Figure 4.4b,e,h). The difference between the two is then plotted in Figure 4.4c,f,i. Figure 4.4a,b compares $\langle\sigma_x\rangle$, Figure 4.4d,e compares $\langle\sigma_y\rangle$, and Figure 4.4g,h compares $\langle\sigma_z\rangle$. We see from the difference plots that the expectation values are equal. Since the identity element is identical in both cases, all of the elements of the 2×2 state density matrix must be identical, and the evolutions are equivalent. The initial parameters are $\rho(0) = f\rangle\langle f$ and $\frac{\Delta}{\gamma_{ge}} = 0.5$.</p>	89
4.5	<p>K_3 Parameter Comparison: Phase Diagrams comparing K_3 calculated from the renormalized Liouvillian evolved $\tilde{\rho}$ (Figure 4.5a) vs the postselected Lindbladian evolved $\bar{\rho}$ (Figure 4.5c). The full Lindbladian evolution is shown for reference in Figure 4.5b. We can clearly see the presence of oscillatory behavior near the unitary limit $\frac{J}{\gamma} \rightarrow \infty$. As we approach the exceptional point $\frac{J}{\gamma} = 1$ the timescale of the oscillations increase, while the peak K_3 during the oscillation approaches the algebraic limit $K_3 \rightarrow 3$, and achieves the limit at the exceptional point. In the \mathcal{PT}-broken regime we observe $K_3 \rightarrow 0$, signifying the system becoming highly uncorrelated.</p>	93

- 4.6 **K_3 Parameter Maximization:** Phase Diagram showing K_3 maximized for each $\frac{J}{\gamma}$ utilizing the optimal Q and $\rho(0)$ listed in Eq.4.37. The \mathcal{PT} -symmetric regime is identical to before. On the other hand, the \mathcal{PT} -broken regime now hosts a single major wavefront where $K_3 \approx 3$. The height of K_3 increases as the perturbation off of $|\epsilon_- \rangle$ is reduced, however doing so pushes the peak of the wavefront out to longer times. 95
- 4.7 **Effect of Non-removable Quantum Jumps on K_3 :** Phase Diagram showing K_3 maximized for each $\frac{J}{\gamma}$ utilizing the optimal Q and $\rho(0)$ listed in Eq.4.37. This time we have included non-removable jumps originating from the dissipators L_{ef} and L_{efz} , with $\frac{\gamma_{ef}}{\gamma_{ge}} = \frac{\gamma_{efz}}{\gamma_{ge}} = 10^{-2}$. The effect of L_{ef} is shown in Figure 4.7b and the effect of L_{efz} is shown in Figure 4.7b. A section of Figure 4.6 near the exceptional point is provided in 4.7a for reference. We see that K_3 near the exceptional point has been forced to $K_3 = 1$, and the surrounding K_3 have been depressed. The only regions with $K_3 \approx 3$ are with strong dissipation. 98
- 4.8 **Exponentiated Work for Jarzynski's Equality:** Phase Diagram showing $\langle e^{-\beta W} \rangle$ with $\frac{J_{max}}{\gamma} = 3$, $\gamma\beta = 1$, and ρ_0 in the thermal state. Above the exceptional point $\frac{J_{min}}{\gamma} = 1$ the function $\langle e^{-\beta W} \rangle$ approaches the predicted value of 1, while below the exceptional point the path traced by $J(t)$ encircles the exceptional point and large oscillations in $\langle e^{-\beta W} \rangle$ occur. However, the transition is smooth and we see deviations from the predicted value grow before the exceptional point is encircled. After passing the opposite exceptional point $\frac{J_{min}}{\gamma} = -1$, we see thin resonance lines appear. 103

ABSTRACT

Open quantum systems have become a rapidly developing sector for research. Such systems present novel physical phenomena, such as topological chirality, enhanced sensitivity, and unidirectional invisibility resulting from both their non-equilibrium dynamics and the presence of exceptional points.

We begin by introducing the core features of open systems governed by non-Hermitian Hamiltonians, providing the \mathcal{PT} -dimer as an illustrative example. Proceeding, we introduce the Lindblad master equation which provides a working description of decoherence in quantum systems, and investigate its properties through the Decohering Dimer and periodic potentials. We then detail our preferred experimental apparatus governed by the Lindbladian. Finally, we introduce the Liouvillian, its relation to non-Hermitian Hamiltonians and Lindbladians, and through it investigate multiple properties of open quantum systems.

1. INTRODUCTION TO NON-HERMITIAN PHYSICS

Over the last quarter-century, non-Hermitian physics has burgeoned into a heavily researched field of study [1]. Initially conceived as an extension to the construction of quantum mechanics [2], non-Hermitian physics has matured into the study of non-conservative but coherent evolution. Today the concepts of non-Hermitian systems have permeated into every branch of physics, spanning semi-classical optical arrays and the transient dynamics of open quantum systems, as well as proving equivalent constructions for classical dissipative systems such as friction and electrical circuits [1].

In this preliminary chapter, we investigate the fundamental construction of quantum mechanics to develop the principles of non-Hermitian physics. We then explore these concepts through the most fundamental case: a two level system known as the \mathcal{PT} -Dimer. Finally, we introduce the Floquet Theorem to expand our analytic techniques to time dependent systems.

1.1 Background and Terminology

In their 1998 paper [2], Bender and Boettcher demonstrated that a class of Hamiltonians extending from the quantum harmonic oscillator (QHO) possessed both purely real spectra and a positive Hilbert space. These Hamiltonians took the form $H = p^2 + x^2(ix)^\epsilon$ where p is the momentum operator, x is the position operator, and ϵ is a real valued parameter. Such systems break many of the conventions of quantum mechanics: (1) they are non-Hermitian when $\epsilon \neq 2\mathbb{Z}$, (2) they do not commute with the parity operator (\mathcal{P}), and (3) they do not commute with the time-reversal operator (\mathcal{T}). Yet these systems do commute with the \mathcal{PT} operator, and contain purely real spectra if $\epsilon \geq 0$. From this seminal work we receive the notions of \mathcal{PT} -symmetry:

- The \mathcal{PT} -symmetric regime, where the spectrum of H is purely real. In this regime, all states are oscillatory.

- The \mathcal{PT} -broken regime, where the spectrum of H contains at least one pair of complex-conjugate energies. In this regime, states with complex energies exhibit exponential growth or decay.
- These two regimes are separated by a transition point referred to as the \mathcal{PT} -threshold. At the source of this transition is the presence of an exceptional point, where two modes of the Hamiltonian become degenerate.

which we still use today in the analysis of general non-Hermitian systems.

The early years of \mathcal{PT} -symmetry were marked by an explosion of theoretical work, but little experimental evidence. The dilemma therein lay in the construction of the complex valued potentials that appeared in non-Hermitian Hamiltonians. These difficulties were eventually alleviated through the field of optics, where complex refractive indices had been used for years as an effective model for absorptive materials. In 2010, Christodoulides et al. reported the experimental observation of \mathcal{PT} -symmetric and \mathcal{PT} -broken modes in an optically coupled waveguide array, using Fe-doped LiNbO_3 as a loss mechanism and an Ar^+ pump laser as a gain mechanism [3]. From this and other experiments in optical lattices, we obtained the notions of gain and loss in \mathcal{PT} -symmetry

- Loss describes potentials which lead to a decrease of detection probability as the system evolves. These are normally associated with Block diagonalized potentials with negative imaginary parameters.
- Gain describes potentials which lead to an increase of detection probability as the system evolves. These are normally associated with Block diagonalized potentials with positive imaginary parameters.

Today, non-Hermitian physics has broadened beyond \mathcal{PT} -symmetric interactions. Passive \mathcal{PT} systems, where a \mathcal{PT} -symmetric system has been shifted by a global decay rate so only loss potentials are needed, can be used to study the presence and interactions between exceptional points [4]. Open systems, such as in ultra-cold atoms [5] and superconducting qubits [6], allow us to study passive \mathcal{PT} systems by selecting for coherent evolution paths of

the state density matrix [7]. Such open systems are governed by the Lindblad master equation, and grant the opportunity to observe exceptional point signatures in a purely quantum setting [6]. In the classical regime, dissipation in optics, electrical circuits, and mechanical systems can be rewritten as equivalent Schrödinger equations, yielding \mathcal{PT} -symmetric interpretations for coupled-laser noise, LC-circuits, and coupled oscillator arrays [1].

1.2 Construction of Quantum Mechanics

To identify the consequences of non-Hermitian physics we now follow the construction of quantum mechanics [8], while removing the restriction that the Hamiltonian be Hermitian [1]. We begin by defining the state $|\psi\rangle$ which contains the information about the current configuration of a quantized system, and exists in a positive definite Hilbert space \mathfrak{H}_ψ . The state $|\psi\rangle$ may depend on a number of continuous variables (time t , position \vec{x} , momentum \vec{p}), discrete variables (occupation number n), or numeric parameters (coupling strength J), etc. and is mathematically equivalent to a vector.

The dynamics of $|\psi\rangle$ are governed by the Schrödinger equation

$$i\partial_t |\psi\rangle = H |\psi\rangle \quad (1.1a)$$

$$-i\partial_t \langle\psi| = \langle\psi| H^\dagger \quad (1.1b)$$

where H is the Hamiltonian operator. It is often useful to split H into its Hermitian and anti-Hermitian components $H = H_h + i\Gamma$ if both are present. As $|\psi\rangle$ is equivalent to a vector, operators may be represented as square matrices of the same rank as $|\psi\rangle$. The Schrödinger equation yields solutions of the form

$$|\psi(t)\rangle = U |\psi(t_0)\rangle \quad (1.2a)$$

$$\langle\psi(t)| = \langle\psi(t_0)| U^\dagger \quad (1.2b)$$

$$U = \mathcal{T}_o e^{-i\int_{t_0}^t dt' H(t')} \xrightarrow{\partial_t H=0} e^{-i(t-t_0)H} \quad (1.2c)$$

The actions of H and U on an arbitrary $|\psi\rangle$ will (in general) be complicated, and so we decompose H into its eigenstate basis

$$H = \sum_j \epsilon_j |\epsilon_j\rangle \langle\langle \epsilon_j| \quad (1.3a)$$

$$H^\dagger = \sum_j \epsilon_j^* |\epsilon_j\rangle\rangle \langle \epsilon_j| \quad (1.3b)$$

where $|\epsilon_j\rangle$ are the right energy-eigenstates, $\langle\langle \epsilon_j|$ are the left energy-eigenstates, and ϵ_j are the associated energies. Note that $|\epsilon_j\rangle$ are members of the Hilbert space of the Hamiltonian \mathfrak{H}_H , while $|\epsilon_j\rangle\rangle$ are instead members of the dual space \mathfrak{H}_H^* . For Hermitian quantum mechanics, the two spaces are equivalent, but for non-Hermitian Hamiltonians $(|\epsilon_j\rangle)^\dagger = \langle \epsilon_j| \neq \langle\langle \epsilon_j|$.

1.2.1 Consequences of Non-Hermiticity

Due to the inequivalences $H^\dagger \neq H$ and $(|\epsilon_j\rangle)^\dagger \neq |\epsilon_j\rangle\rangle$, a few consequences arise in the standard definition of states. First the eigenstates lose their orthogonality condition which is replaced by a bi-orthogonality condition with the left-eigenstates

$$\langle \epsilon_i | \epsilon_j \rangle \neq \delta_{ij} \quad (1.4a)$$

$$\langle\langle \epsilon_i | \epsilon_j \rangle\rangle \neq \delta_{ij} \quad (1.4b)$$

$$\langle\langle \epsilon_i | \epsilon_j \rangle = \delta_{ij} \quad (1.4c)$$

which allows us to form projectors $|\epsilon_j\rangle \langle\langle \epsilon_j|$. Second, the violation of the spectral theorem

$$\langle \epsilon_i | (H^\dagger - H) | \epsilon_j \rangle = (\epsilon_i^* - \epsilon_j) \langle \epsilon_i | \epsilon_j \rangle \quad (1.5)$$

removes the restriction that the energies be real valued. Third, as H is no longer Hermitian U is not expected to be a unitary matrix. Fourth, the norm and energy of a given state is expected to vary with time

$$\partial_t \langle \psi_i | \psi_j \rangle = i \langle \psi_i | (H^\dagger - H) | \psi_j \rangle \neq 0 \quad (1.6)$$

$$\partial_t \langle \psi_i | H | \psi_j \rangle = i \langle \psi_i | (H^\dagger - H) H | \psi_j \rangle + \langle \psi_i | \partial_t(H) | \psi_j \rangle \quad (1.7)$$

and therefore there is a flow of both probability and energy into/out of the system, identifying such Hamiltonians as describing non-conservative dynamics. Finally, at the exceptional point n different eigenstates become degenerate and H is no longer diagonalizable, marking the exceptional point as n^{th} order. This is then reflected in U which terminates at the n^{th} order correction. As a direct result of this point, the time evolution of a general state requires Jordan generalized eigenvectors to describe [1].

The Jordan Normal Form of H is a direct sum of Jordan blocks

$$HV = VJ \quad (1.8)$$

$$J = \bigoplus_j J_j = \begin{bmatrix} \epsilon_0 & 0 & 0 & 0 & 0 \\ 0 & \epsilon_1 & 0 & 0 & 0 \\ 0 & 0 & \epsilon_2 & 1 & 0 \\ 0 & 0 & 0 & \epsilon_2 & 1 \\ 0 & 0 & 0 & 0 & \epsilon_2 \end{bmatrix} \quad (1.9)$$

where j counts the unique eigenvalues of H . Each individual Jordan block is an $n \times n$ matrix $J_j = \epsilon_j \mathbb{1} + D_1$ where n is the order of the exceptional point and D_1 are the elements of the first superdiagonal of the matrix. The first Jordan vector $|\epsilon_{j,1}\rangle$ to appear will be equal to the degenerate eigenvector of H , while subsequent Jordan vectors are obtained from

$$(H - \epsilon_j \mathbb{1}) |\epsilon_{j,k_j}\rangle = |\epsilon_{j,k_j-1}\rangle \quad (1.10a)$$

$$(H - \epsilon_j \mathbb{1})^{k_j} |\epsilon_{j,k_j}\rangle = 0 \quad (1.10b)$$

$$\langle\langle \epsilon_{j,k_j} | (H - \epsilon_j \mathbb{1})^{k_j} = 0 \quad (1.10c)$$

To determine the time evolution of a general state, we utilize the property

$$f(J) = \begin{bmatrix} f(\epsilon_0) & 0 & 0 & 0 & 0 \\ 0 & f(\epsilon_1) & 0 & 0 & 0 \\ 0 & 0 & f(\epsilon_2) & \frac{1}{1!} \partial_\epsilon f(\epsilon_2) & \frac{1}{2!} \partial_\epsilon^2 f(\epsilon_2) \\ 0 & 0 & 0 & f(\epsilon_2) & \frac{1}{1!} \partial_\epsilon f(\epsilon_2) \\ 0 & 0 & 0 & 0 & f(\epsilon_2) \end{bmatrix} \quad (1.11)$$

to write the time evolution as

$$|\psi(t)\rangle = U |\psi(t_0)\rangle = \sum_j \sum_{k_j=1}^{n_j} \sum_{k_i=1}^{k_j} \frac{t^{k_j-k_i}}{(k_j-k_i)!} e^{-\epsilon_j t} |\epsilon_{j,k_i}\rangle \langle\langle \epsilon_{j,k_j} | \psi(t_0)\rangle\rangle \quad (1.12)$$

1.2.2 Degrees of Non-Hermiticity

While all non-Hermitian systems will have the properties described above, the active interests of the field are in systems that retain real spectra for some subset of the parameter region away from the Hermitian limit, or that allow us to study the properties of such systems. Hamiltonians that retain purely real spectra will be oscillatory under time evolution, and therefore a general preparation state $|\psi\rangle$ is stable and can be observed over long time frames. On the other hand, systems that avoid implementing gain potentials also avoid the difficulties associated with such terms, such as exponentially growing norms and non-linear or noisy effects in real world implementations. These pure-loss systems allow the study of geometric properties such as exceptional point contours over short time frames. We now categorize the three major classes of non-Hermitian systems studied today.

\mathcal{PT} -Symmetry

The class of \mathcal{PT} -symmetric systems consists of all Hamiltonians that commute with an anti-linear \mathcal{PT} operator

$$[H, \mathcal{PT}] = 0 \quad (1.13a)$$

$$\mathcal{PT}H\mathcal{T}^{-1}\mathcal{P}^{-1} = H \quad (1.13b)$$

In the most general construction, \mathcal{P} is some involutory operator ($\mathcal{P}^2 = \mathbb{1}$) that is usually chosen as one of the symmetries of the Hermitian component of the Hamiltonian. On the other hand, \mathcal{T} is an anti-unitary operator [9]

$$\mathcal{T} = U\mathcal{K} \quad (1.14a)$$

$$\mathcal{T}|\psi\rangle = \mathcal{T}\sum_{\mathbf{j}}c_{\mathbf{j}}|\mathbf{j}\rangle = \sum_{\mathbf{j}}c_{\mathbf{j}}^*\mathcal{T}|\mathbf{j}\rangle \quad (1.14b)$$

where \mathcal{K} is the complex conjugation operator ($\mathcal{K}\iota\mathcal{K} = -\iota$), and U is a unitary matrix. Usually we can choose $U = \mathbb{1}$ for simplicity and require $\mathcal{P}H\mathcal{P} = H^*$, though it is sometimes physically relevant to choose a specific U ($\mathcal{T} = e^{-i\pi S^y}\mathcal{K}$ for particles with spin \vec{S}).

Two major properties arise as a result of this commutation property. First, we obtain the similarity transformation

$$H^* = \mathcal{P}UH(\mathcal{P}U)^{-1} \quad (1.15)$$

This implies that \mathcal{PT} -symmetric systems must have eigenvalues that are real or come in complex conjugate pairs as similar matrices must share a set eigenvalues. Second and more subtly, due to the interaction of the anti-linear \mathcal{PT} with the complex spectrum of H

$$H(\mathcal{PT}|\epsilon_{\mathbf{j}}\rangle) = \mathcal{P}TH|\epsilon_{\mathbf{j}}\rangle \quad (1.16a)$$

$$= \epsilon_{\mathbf{j}}^*(\mathcal{PT}|\epsilon_{\mathbf{j}}\rangle) \quad (1.16b)$$

$$H|\epsilon_{\mathbf{j}}\rangle = \epsilon_{\mathbf{j}}^*|\epsilon_{\mathbf{j}}\rangle \quad (1.16c)$$

Table 1.1. Table comparing the effects of the operators \mathcal{P} , \mathcal{T} , and \mathcal{PT} on physically relevant quantities. \mathcal{P} negates vectors while leaving bi-vectors unchanged. \mathcal{T} negates fields sourced by a current.

	\mathcal{P}	\mathcal{T}	\mathcal{PT}
Time	$t \rightarrow t$	$t \rightarrow -t$	$t \rightarrow -t$
Position	$\vec{x} \rightarrow -\vec{x}$	$\vec{x} \rightarrow \vec{x}$	$\vec{x} \rightarrow -\vec{x}$
Energy	$E \rightarrow E$	$E \rightarrow E$	$E \rightarrow E$
Linear Momentum	$\vec{p} \rightarrow -\vec{p}$	$\vec{p} \rightarrow -\vec{p}$	$\vec{p} \rightarrow \vec{p}$
Angular Momentum	$\vec{L} \rightarrow \vec{L}$	$\vec{L} \rightarrow -\vec{L}$	$\vec{L} \rightarrow -\vec{L}$
Electric Field	$\vec{E} \rightarrow -\vec{E}$	$\vec{E} \rightarrow \vec{E}$	$\vec{E} \rightarrow -\vec{E}$
Magnetic Field	$\vec{B} \rightarrow \vec{B}$	$\vec{B} \rightarrow -\vec{B}$	$\vec{B} \rightarrow -\vec{B}$
Spin	$\vec{S} \rightarrow \vec{S}$	$\vec{S} \rightarrow -\vec{S}$	$\vec{S} \rightarrow -\vec{S}$

and so H and \mathcal{PT} will only share an eigenbasis while H has a purely real spectrum.

The main draw of \mathcal{PT} -symmetry among non-Hermitian systems is that it prompts a physically motivated construction of the non-Hermitian Hamiltonian. \mathcal{P} is chosen as the parity operator ($\vec{x} \rightarrow -\vec{x}$), while \mathcal{T} is chosen as the time reversal operator ($t \rightarrow -t$). For a physically motivated Hamiltonian $H = \frac{p^2}{2m} + V(x)$, Eq.1.13a requires that the potential energy $V(x)$ take the form

$$H = \frac{p^2}{2m} + V_1(x) + iV_{-1}(x) \quad (1.17)$$

where $\mathcal{P}V_1(x)\mathcal{P} = V_1(x)$ and $\mathcal{P}V_{-1}(x)\mathcal{P} = -V_{-1}(x)$. Table 1.1 lists some of the most commonly employed transformation properties when designing \mathcal{PT} -symmetric perturbations.

Pseudo-Hermiticity and Quasi-Hermiticity

The second major class of non-Hermitian systems are defined by the intertwining relation [10]

$$\eta H = H^\dagger \eta \quad (1.18)$$

for some set of Hermitian operators η . From Eq.1.1 it follows that such operators define conserved quantities of H

$$\partial_t \langle \psi | \eta | \psi \rangle = -i \langle \psi | (\eta H - H^\dagger \eta) | \psi \rangle = 0 \quad (1.19)$$

From Eq.1.3, we can construct one set of η from the left-eigenstates of H

$$\eta_{\epsilon_j} = \begin{cases} |\epsilon_j\rangle\rangle \langle\langle \epsilon_j| & \epsilon_j \in \mathbb{R} \\ \frac{|\epsilon_j\rangle\rangle \langle\langle \epsilon_{j*}| + |\epsilon_{j*}\rangle\rangle \langle\langle \epsilon_j|}{2} & \epsilon_j \notin \mathbb{R} \\ \frac{|\epsilon_j\rangle\rangle \langle\langle \epsilon_{j*}| - |\epsilon_{j*}\rangle\rangle \langle\langle \epsilon_j|}{2i} & \epsilon_j \notin \mathbb{R} \end{cases} \quad (1.20)$$

and since Eq.1.18 is linear in η we can construct any other set from linear combinations of η_{ϵ_j} . From here we can define two useful restrictions on the η operators.

First, if we construct η to be invertible then we can rewrite Eq.1.18 as a similarity transformation

$$H^\dagger = \eta H \eta^{-1} \quad (1.21)$$

Just as in Eq.1.15 this requires that the spectrum of H consists of purely real or complex conjugate paired eigenvalues. Systems satisfying this restriction are referred to as η -pseudo-Hermitian [1], [10]–[13], and demonstrate all of the unique properties of \mathcal{PT} -symmetric systems. In fact, many \mathcal{PT} -symmetric systems are \mathcal{P} -pseudo-Hermitian.

Furthermore, if we can construct at least one η to be positive-definite that η can be decomposed as a principal root

$$\eta = \xi^\dagger \xi \quad (1.22)$$

Substituting into Eq.1.21 yields

$$h = \xi H \xi^{-1} = (\xi^\dagger)^{-1} H^\dagger \xi^\dagger = (\xi H \xi^{-1})^\dagger = h^\dagger \quad (1.23)$$

Therefore, whenever a positive-definite η exists there is a similarity transformation (referred to as the Dyson map [13]) between the non-Hermitian system H and a Hermitian system

h , restricting H to purely real spectra. In addition, the Hermitian system h will possess orthogonal eigenstates $|\lambda_j\rangle = \xi|\epsilon_j\rangle$, and so the eigenstates of H will be orthogonal under the metric η

$$\langle \epsilon_i | \epsilon_j \rangle_\eta = \langle \epsilon_i | \xi^\dagger \xi | \epsilon_j \rangle = \langle \lambda_i | \lambda_j \rangle = \delta_{ij} \quad (1.24)$$

From these properties, the region where an η -pseudo-Hermitian H possesses a positive definite η is the equivalent of the \mathcal{PT} -symmetric region, the region where a positive definite η is no longer constructible is the \mathcal{PT} -broken region, and the transition point corresponds to the \mathcal{PT} -threshold [11]–[13].

Before moving forward, we will note the use of the term Quasi-Hermitian within the broader field [11]–[13]. Quasi-Hermitian systems are non-Hermitian systems which possess purely real spectra for their entire parameter space. Specifically, quasi-hermiticity is defined by positive-definite (but not necessarily invertible) η which span the entire parameter space, while pseudo-hermiticity is defined by invertible (but not necessarily positive-definite) η . Such a definition makes quasi-hermiticity a subset of pseudo-hermiticity for any finite rank H . However, for systems with infinite rank (such as systems with continuous variables) the positive-definite η may be defined using unbounded operators which cannot be inverted (ex: ∂_x), and so it is in such infinite systems where the distinction becomes important.

Passive \mathcal{PT} Systems

The third class of non-Hermitian systems commonly studied are passive \mathcal{PT} systems [4], [14]. Such systems are constructed from a \mathcal{PT} -symmetric system that has been shifted by a global decay rate

$$H_{p\mathcal{PT}} = H_{\mathcal{PT}} - i\gamma_p \mathbb{1} \quad (1.25)$$

As a result, Eq.1.15 is broken and the system will not maintain real spectra. However, the geometric properties of the original system will remain intact, allowing one to study the exceptional points and \mathfrak{H}_H of the original system.

The main advantage of studying passive \mathcal{PT} systems is the reduction / removal of gain potentials from the original model. Unlike loss potentials, a system with excess gain will eventually saturate resulting in non-linear dynamics in real-world experiments. Because of these non-linear effects, experimental validations of \mathcal{PT} -symmetry have required that the apparatus be run in the low gain limit where the gain can be approximated as a linear potential [1], [3], [7], [14]. By removing the gain elements, experimental teams can trade observation time for better signal-to-noise ratios.

1.3 Fundamental Case: \mathcal{PT} -Dimer

Let us consider the simplest possible non-Hermitian model and determine under what conditions the model will demonstrate \mathcal{PT} -symmetric behavior. For a rank 2 Hamiltonian $H_{2general}$, a general parametrization would be

$$H_{2general} = \sum_{j=0}^3 a_j \sigma_j = \begin{bmatrix} a_0 + a_3 & a_1 - \imath a_2 \\ a_1 + \imath a_2 & a_0 - a_3 \end{bmatrix} \quad (1.26)$$

where a_j are complex coefficients and σ_j are the Pauli matrices. The eigenvalues of the general model are $\epsilon_{2general} = a_0 \pm \sqrt{a_1^2 + a_2^2 + a_3^2}$, which are real only when

$$\text{Im}(a_0) = 0 \quad (1.27a)$$

$$\text{Im}(a_1^2 + a_2^2 + a_3^2) = 0 \quad (1.27b)$$

$$\text{Re}(a_1^2 + a_2^2 + a_3^2) \geq 0 \quad (1.27c)$$

Condition 1.27a is simply a complex identity shift and can be used to displace a \mathcal{PT} -symmetric system into a passive \mathcal{PT} system. Condition 1.27b separates trivially-broken models from models with \mathcal{PT} -symmetric and \mathcal{PT} -broken regimes. Since the coefficients $a_j = \text{Re}(a_j) + \imath \text{Im}(a_j)$ are complex, Condition 1.27b can be rewritten as $\text{Re}([a_1 \ a_2 \ a_3]) \cdot \text{Im}([a_1 \ a_2 \ a_3]) = 0$ using vectors formed from the real and imaginary components. Thus, the Hermitian and anti-Hermitian components of $H_{2general}$ must be orthogonal to demon-

strate \mathcal{PT} -symmetric behavior. Finally, Condition 1.27c separates the \mathcal{PT} -symmetric and \mathcal{PT} -broken regimes for non-trivial models.

If we take these conditions into consideration, we can simplify $H_{2general}$ to the point of unitary invariance. The reduced form is

$$H_2 = \frac{1}{2} \begin{bmatrix} \Delta + i\gamma & J \\ J & -\Delta - i\gamma \end{bmatrix} = \frac{J}{2} \sigma_x + \frac{(\Delta + i\gamma)}{2} \sigma_z \quad (1.28)$$

where Δ is the energy difference between the states in the z -basis, J is the coupling strength between the two levels, and γ is the non-Hermitian perturbation strength. We refer to this as the \mathcal{PT} -Dimer, and it is the model upon which much of the novel material of this work is constructed. Since we have aligned the anti-Hermitian components with the z -axis, $\frac{\Delta}{J} = 0$ is required for real eigenvalues to emerge. The factor of $\frac{1}{2}$ is set by convention so that the period when $\Delta = \gamma = 0$ is $T = 2\pi$. Figure 1.1 provides two commonly employed experimental models which differ from H_2 by an identity shift.

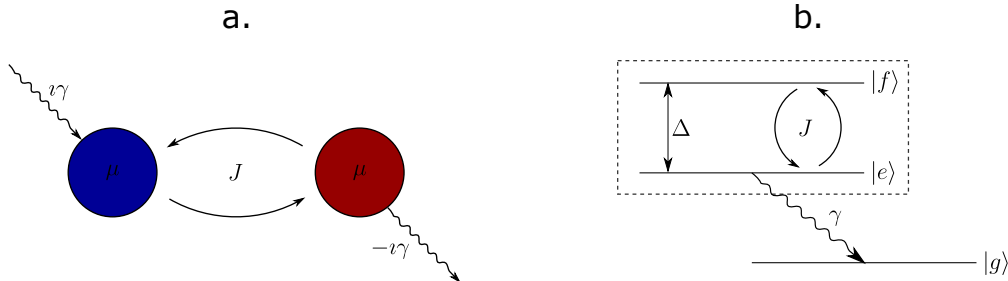


Figure 1.1. \mathcal{PT} -Dimer: Illustrations commonly used for a \mathcal{PT} -symmetric, two level system. Figure 1.1a shows the cross-section of a system of two waveguides, where J is the evanescent coupling, and $\eta_{\pm} = \mu \pm i\gamma$ are the (complex) refractive indices for the two waveguides [4]. Figure 1.1b shows an energy level diagram for a driven two level atom (denoted by the dashed line box), where $\frac{J}{2}$ is a microwave drive, Δ is the energy level difference between $|f\rangle$ and $|e\rangle$, and γ is the decay rate of $|e\rangle$ into an auxiliary state [6], [15]. The Hamiltonians are provided below each model, and are an identity shift away from H_2 .

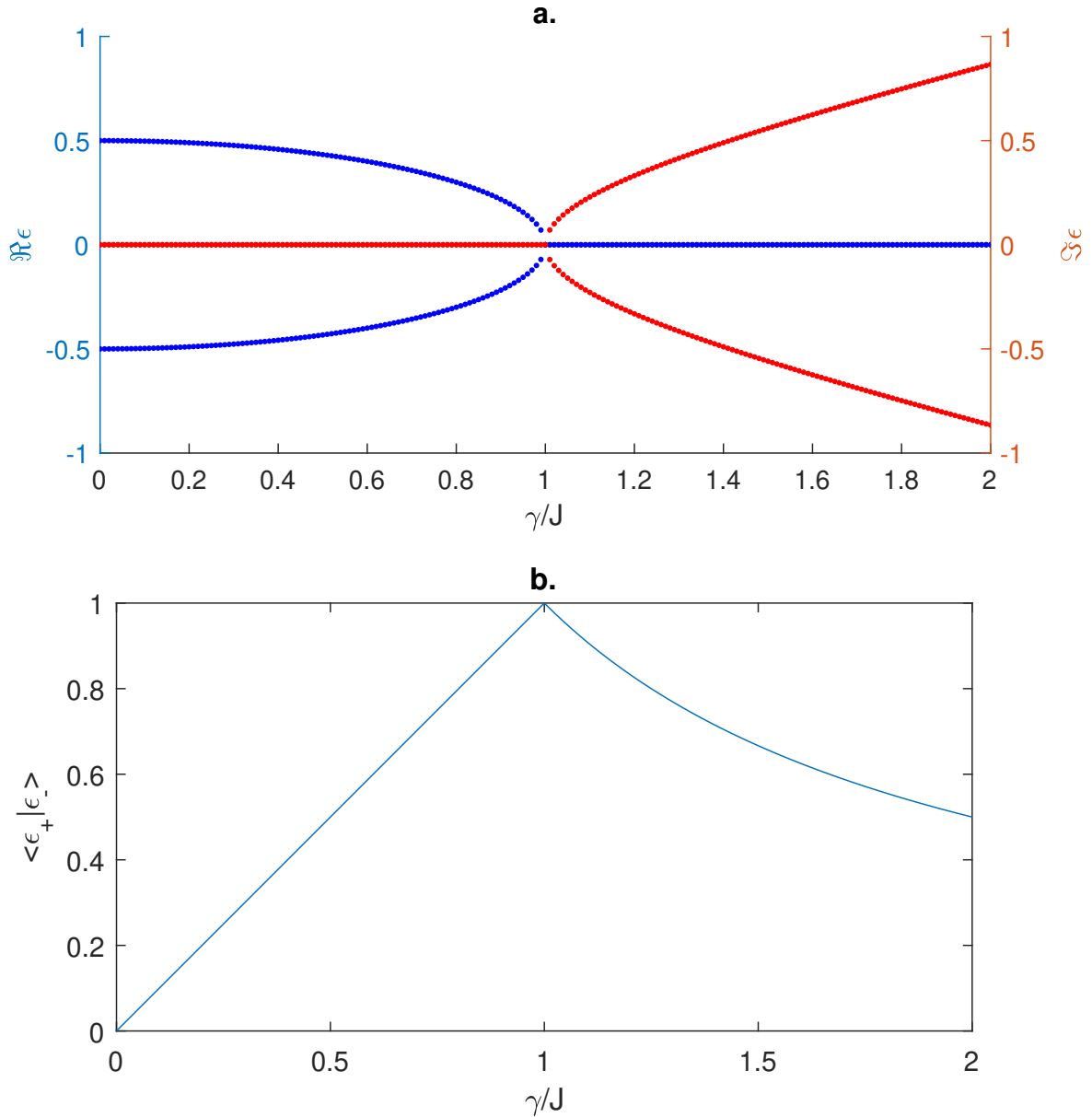


Figure 1.2. ϵ_{\pm} when $\Delta = 0$: Shows the energies ϵ_{\pm} as $\frac{\gamma}{J}$ is varied from $[0, 2]$. Fig.1.2a shows the real part in (blue), while the imaginary part is shown in (red). The presence of an exceptional point can clearly be seen at $\frac{\gamma}{J} = 1$, at which point ϵ_{\pm} and $|\epsilon_{\pm}\rangle$ are degenerate. Fig.1.2b shows $\langle \epsilon_+ | \epsilon_- \rangle$ as a measure of non-orthogonality. We observe a linear increase in the overlap until reaching $\langle \epsilon_+ | \epsilon_- \rangle = 1$ at the exceptional point, after which the overlap decays as $\frac{J}{\gamma}$.

The energies and eigenstates for H_2 are

$$\epsilon_{\pm} = \pm \frac{\sqrt{J^2 + (\Delta + i\gamma)^2}}{2} \quad (1.29a)$$

$$|\epsilon_{\pm}\rangle = \frac{1}{A} \left(\frac{\Delta + i\gamma + 2\epsilon_{\pm}}{J} |\uparrow\rangle + |\downarrow\rangle \right) \quad (1.29b)$$

$$\langle\langle \epsilon_{\pm}| = \frac{JA}{4\epsilon_{\pm}} \left(\langle\uparrow| + \frac{-\Delta - i\gamma + 2\epsilon_{\pm}}{J} \langle\downarrow| \right) \quad (1.29c)$$

where A is the normalization such that $\langle \epsilon_j | \epsilon_j \rangle = 1$. Note that when H_2 is in the \mathcal{PT} -symmetric phase ($\Delta = 0$, $|\frac{\gamma}{J}| < 1$) the eigenstates take a simplified form

$$|\epsilon_{\pm}\rangle = \frac{1}{\sqrt{2}} \left(\pm e^{\pm i\theta} |\uparrow\rangle + |\downarrow\rangle \right) \quad \iff \quad \Delta = 0, \left| \frac{\gamma}{J} \right| < 1 \quad (1.30a)$$

$$\langle\langle \epsilon_{\pm}| = \frac{\sec(\theta)}{\sqrt{2}} \left(\langle\uparrow| \pm e^{\mp i\theta} \langle\downarrow| \right) \quad \iff \quad \Delta = 0, \left| \frac{\gamma}{J} \right| < 1 \quad (1.30b)$$

where $\theta = \sin^{-1}(\frac{\gamma}{J}) = \cos^{-1} \left(\sqrt{1 - \left(\frac{\gamma}{J}\right)^2} \right)$.

Figure 1.2 shows the progression of the energy levels when $\Delta = 0$ as $\frac{\gamma}{J}$ is increased from $0 \rightarrow 2$, with $\text{Re}(\epsilon_{\pm})$ in blue and $\text{Im}(\epsilon_{\pm})$ in red. From Eq.1.29a and Fig.1.2 we detect exceptional points at the coordinates $(\Delta = 0, \frac{\gamma}{J} = \pm 1)$, where the right-eigenstates and left-eigenstates coalesce on opposite sides of the Bloch sphere. Fig.1.2a shows that in the region $(\Delta = 0, |\frac{\gamma}{J}| < 1)$ H_2 is in the \mathcal{PT} -symmetric phase and ϵ_{\pm} are purely real, while in the region $(\Delta = 0, |\frac{\gamma}{J}| > 1)$ H_2 is in the \mathcal{PT} -broken phase and ϵ_{\pm} are complex. Fig.1.2b measures the non-orthogonality of the eigenstates $\langle \epsilon_+ | \epsilon_- \rangle$. Here we see that the $|\epsilon_{\pm}\rangle$ become degenerate in addition to ϵ_{\pm} .

The time evolution operator for the system is $U_2 = e^{-itH_2}$. However, since H_2 is finite rank we can eventually decompose H_2^n in terms of the lower powers of H_2 . For our model $H_2^2 = \epsilon_{\pm}^2 \mathbb{1}$, and so U_2 can be decomposed as

$$U_2 = \cos(\epsilon_{\pm} t) \mathbb{1} - \frac{i}{\epsilon_{\pm}} \sin(\epsilon_{\pm} t) H_2 \quad (1.31)$$

which can be further reduced when $\Delta = 0$

$$U_2 = \begin{cases} \cos(|\epsilon_{\pm}| t)\mathbb{1} - \frac{i}{|\epsilon_{\pm}|} \sin(|\epsilon_{\pm}| t)H_2 & \forall \quad \left|\frac{\gamma}{J}\right| < 1 \\ \mathbb{1} - itH_2 & \forall \quad \left|\frac{\gamma}{J}\right| = 1 \\ \cosh(|\epsilon_{\pm}| t)\mathbb{1} - \frac{i}{|\epsilon_{\pm}|} \sinh(|\epsilon_{\pm}| t)H_2 & \forall \quad \left|\frac{\gamma}{J}\right| > 1 \end{cases} \quad (1.32)$$

We see here that the expansion of U_2 terminates at $n = 2$ for the exceptional point, again marking the exceptional point as 2^{nd} order.

From the perspective of \mathcal{PT} -Symmetry, the principal anti-linear symmetry responsible for this behavior is the \mathcal{PT} operator

$$\mathcal{PT} = \begin{bmatrix} 0 & 1 \\ 1 & 0 \end{bmatrix} \mathcal{K} \quad (1.33)$$

where \mathcal{P} exchanges z -eigenstates ($|\uparrow\rangle \leftrightarrow |\downarrow\rangle$), and \mathcal{T} is the complex conjugation operator (\mathcal{K}). The eigenvalues and eigenstates of \mathcal{PT} are identical to σ_x . However, from the relation $\mathcal{PT}^2 = \mathbb{1}$

$$|\phi\rangle = \mathcal{PT}^2 |\phi\rangle = \mathcal{PT} (\lambda |\phi\rangle) = |\lambda|^2 |\phi\rangle \quad (1.34)$$

we find that $\lambda = e^{i\phi}$ is a phase factor. Including this phase with the eigenstates yields the basis

$$|1\rangle = |\rightarrow\rangle = \frac{1}{\sqrt{2}} \begin{bmatrix} 1 \\ 1 \end{bmatrix}, \quad |2\rangle = i|\leftarrow\rangle = \frac{i}{\sqrt{2}} \begin{bmatrix} 1 \\ -1 \end{bmatrix} \quad (1.35)$$

each with eigenvalue $\lambda = 1$. Linear combinations of $|1\rangle$ and $|2\rangle$ are also eigenstates of \mathcal{PT} , but only if the linear coefficients are real valued. Therefore, all states along the xy -plane of the Bloch sphere are valid eigenstates of \mathcal{PT} , while any state where $\langle\psi|\sigma_z|\psi\rangle \neq 0$ cannot be recreated. Figure 1.3 shows the path taken by the eigenstates as $\frac{\gamma}{J}$ varies between $[0, 10]$. Fig.1.3a shows that in the \mathcal{PT} -symmetric phase ($\Delta = 0$, $|\frac{\gamma}{J}| \leq 1$) (blue) the eigenstates of H_2 lie along the xy -plane up until the exceptional point, where they deviate onto the yz -plane

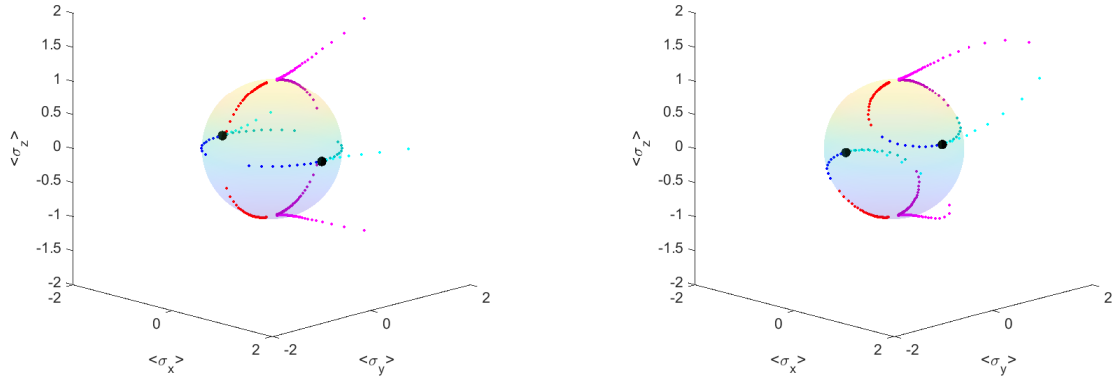


Figure 1.3. Progression of States: Depiction of a Bloch sphere formed by $|\uparrow\rangle$ and $|\downarrow\rangle$ as H_2 varies from $\frac{\gamma}{J} \in [0, 10]$. Fig.1.3a shows points for $\frac{\Delta}{J} = 0$, while Fig.1.3b shows points for $\frac{\Delta}{J} = 0.25$. The spacing between points is $\frac{\gamma}{J} = 0.1$. At the Hermitian limit (black), the $|\epsilon_{\pm}\rangle$ are orthogonal at opposite points of the Bloch sphere aligned on the x -axis. For Fig.1.3a, as γ is increased in the \mathcal{PT} -symmetric phase (blue), the $|\epsilon_{\pm}\rangle$ approach $|\downarrow\rangle_y = [1 \quad -i]^T$ while $\langle\epsilon_+|\epsilon_-\rangle \rightarrow 1$, finally becoming degenerate at $\frac{\gamma}{J} = 1$. After passing the exceptional point (red), the $|\epsilon_{\pm}\rangle$ asymptotically approach $|\uparrow\rangle$, where at $\frac{\gamma}{J} = \infty$ they become orthogonal once more. For Fig.1.3b, H_2 is always in the \mathcal{PT} -broken phase except at the Hermitian limit (the regions of $\frac{\gamma}{J} \leq 1$ and $\frac{\gamma}{J} \geq 1$ are denoted with the same colors as before). The corresponding $|\epsilon_{\pm}\rangle$ (cyan and magenta) always exist in the direction opposite to their conjugate counterpart $|\epsilon_{\mp}\rangle$, but due to the normalization $\langle\langle\epsilon_i|\epsilon_j\rangle\rangle = \delta_{ij}$ are not bound to the Bloch sphere. Their projections onto the Bloch sphere are plotted in faded colors.

for higher values of $\left|\frac{\gamma}{J}\right|$ (red) and no longer serve as a basis for \mathcal{PT} . In contrast, Fig.1.3b shows how when $\Delta \neq 0$ the model is trivially broken, as the eigenstates of H_2 are never in contact with the xy -plane.

From the perspective of Pseudo-hermiticity, we find two intertwining operators when $\Delta = 0$

$$\eta_1 = \sigma_x = \begin{bmatrix} 0 & 1 \\ 1 & 0 \end{bmatrix} \quad (1.36a)$$

$$\eta_2 = \mathbb{1} + \frac{\gamma}{J}\sigma_y = \begin{bmatrix} 1 & -\frac{\gamma}{J} \\ \frac{\gamma}{J} & 1 \end{bmatrix} \quad (1.36b)$$

Here we see that η_1 is simply \mathcal{P} , while η_2 has eigenvalues $\lambda = 1 \pm \frac{\gamma}{J}$ making it positive definite within the \mathcal{PT} -symmetric region. Within this region we can define the Dyson map

$$\begin{aligned} \xi_2 &= \frac{\sqrt{1 + \frac{\gamma}{J}} + \sqrt{1 - \frac{\gamma}{J}}}{2} \mathbb{1} + \frac{\sqrt{1 + \frac{\gamma}{J}} - \sqrt{1 - \frac{\gamma}{J}}}{2} \sigma_y \\ &= \begin{bmatrix} \frac{\sqrt{1 + \frac{\gamma}{J}} + \sqrt{1 - \frac{\gamma}{J}}}{2} & \frac{-i\sqrt{1 + \frac{\gamma}{J}} + i\sqrt{1 - \frac{\gamma}{J}}}{2} \\ \frac{i\sqrt{1 + \frac{\gamma}{J}} - i\sqrt{1 - \frac{\gamma}{J}}}{2} & \frac{\sqrt{1 + \frac{\gamma}{J}} + \sqrt{1 - \frac{\gamma}{J}}}{2} \end{bmatrix} \end{aligned} \quad (1.37)$$

$$h = \xi_2 H_2 \xi_2^{-1} = \sqrt{J^2 - \gamma^2} \sigma_x \quad (1.38)$$

The expectation values for each η_j are

$$\langle \epsilon_{\pm} | U^\dagger \eta_1 U | \epsilon_{\pm} \rangle = \langle \epsilon_{\pm} | \eta_1 U^{-1} U | \epsilon_{\pm} \rangle = \langle \epsilon_{\pm} | \eta_1 | \epsilon_{\pm} \rangle = \pm \sqrt{1 - \left(\frac{\gamma}{J}\right)^2} \quad (1.39a)$$

$$\langle \epsilon_{\pm} | \eta_2 | \epsilon_{\pm} \rangle = 1 - \left(\frac{\gamma}{J}\right)^2 \quad (1.39b)$$

These expectation values do not change with time so long as Δ , γ , and J are static, marking them as constants of motion.

Finally, we can consider an alternate perspective where J and Δ vary as γ is held constant. These conditions commonly occur in experimental settings where the gain or loss rate of the model is fixed by the physical construction of the \mathcal{PT} -dimer, while J and Δ can be modified by adjusting external fields [4]. Alternatively, such diagrams prove useful when periodically

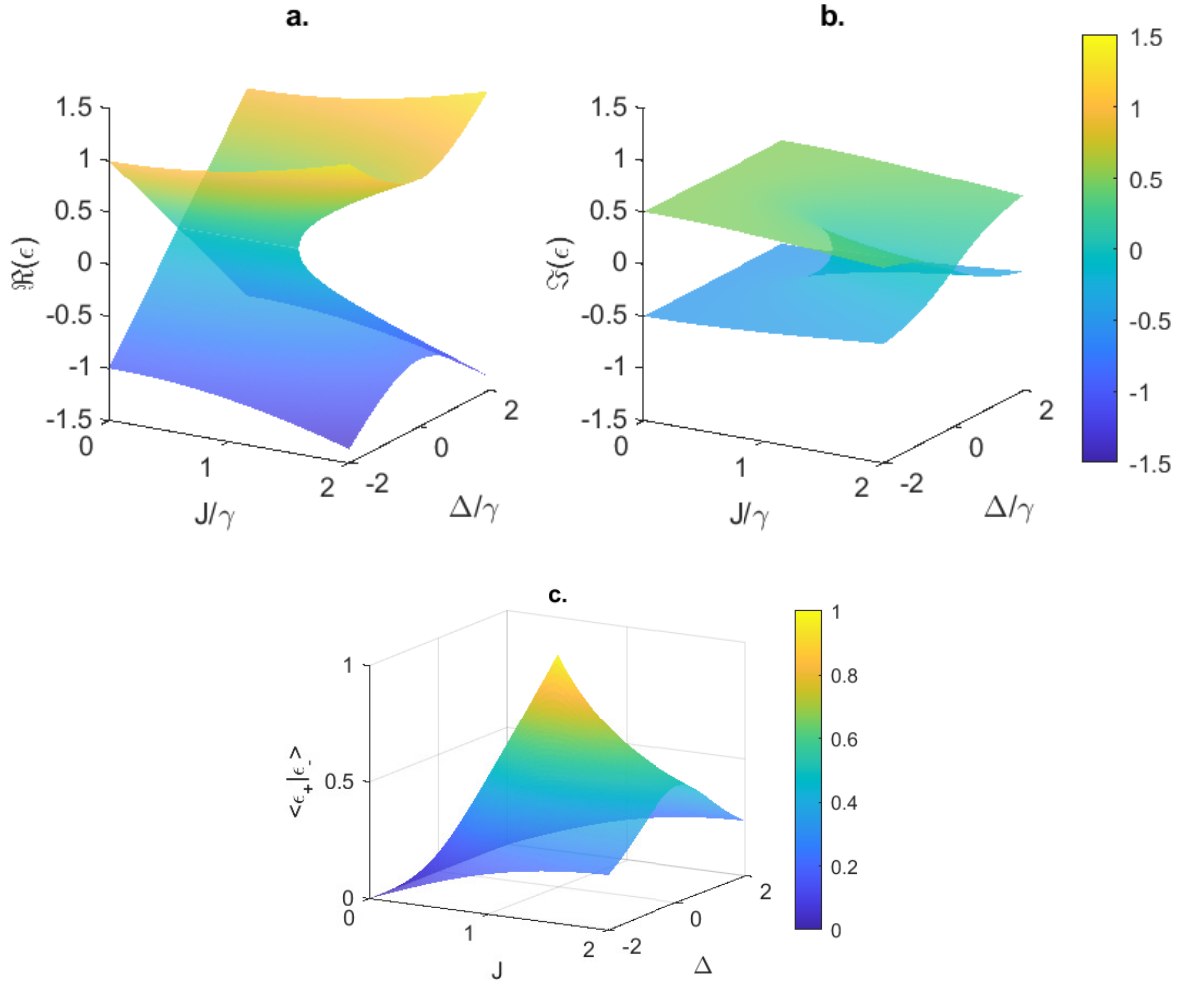


Figure 1.4. ϵ Surface: Shows the energies ϵ_{\pm} as $\frac{J}{\gamma}$ is varied from $[0, 2]$ and $\frac{\Delta}{\gamma}$ is varied from $[-2, 2]$. Fig.1.4a shows the real part, while Fig.1.4b shows the imaginary part. The presence of an exceptional point can again be seen at $\frac{\Delta}{\gamma} = 0, \frac{J}{\gamma} = 1$. Fig.1.2c shows $\langle \epsilon_+ | \epsilon_- \rangle$ reaching $\langle \epsilon_+ | \epsilon_- \rangle = 1$ at the exceptional point.

driving J and Δ in order to encircle exceptional points. Figure 1.4 shows the progression of the energy levels when γ is held constant ($\gamma = 1$) for varying values of J and Δ . We observe the exceptional point at $(\frac{\Delta}{\gamma} = 0, |\frac{J}{\gamma}| = 1)$. Moreover, we now see that the ϵ form a surface which intersects itself, with the intersection defining the non-trivial \mathcal{PT} -broken regime in $\text{Re}(\epsilon_{\pm})$ and the \mathcal{PT} -symmetric regime in $\text{Im}(\epsilon_{\pm})$. $|\psi\rangle$ traveling around the exceptional point due to a time dependent U are forced to follow the curvature of the surface through the intersection, resulting in the "Mode-Switching" phenomenon described in [4].

1.4 Floquet Analysis for Non-Hermitian Physics

So far we have investigated systems driven by static Hamiltonians $\partial_t H(t) = 0$, under which $U = \exp(-itH)$. As a result we are assured that U and H will share a basis since $[H, U] = 0$, and therefore finding the solutions of H amounts to finding the normal modes of the system as it evolves in time. We now need to consider systems where H varies in time, especially systems where the instantaneous Hamiltonian does not commute with the total time evolution $[H(t), U] \neq 0$. Such U must generally be diagonalized into a time dependent basis. However if the Hamiltonian is periodic in time with some period T then we can observe quasi-stable modes over timescales $\delta t_F \gg T$. Characterizing these quasi-stable modes is the focus of Floquet Analysis, which we will now apply in the context of non-Hermitian Hamiltonians [16].

Consider a time dependent $H(t)$ with period T parametrized as

$$H(t + nT) = H(t) \quad \forall \quad t \in [0, T], \quad n \in \mathbb{Z}^{0+} \quad (1.40)$$

The time evolution operator $U(t + nT)$ is then given by Eq.1.2. However, since $H(t + nT)$ is periodic we can split $U(t + nT)$ into a combination of regular $U(T)$ and particular $U(t)$

$$\begin{aligned} U(t + nT) &= \mathcal{T}_o e^{-i \int_0^{t+nT} dt' H(t')} \\ &= \mathcal{T}_o e^{-i \int_0^t dt' H(t')} \left(e^{-i \int_0^T dt' H(t')} \right)^n \end{aligned} \quad (1.41)$$

From this we define the Floquet Time Evolution operator U_F , as well as the Floquet Hamiltonian H_F

$$U_F = \mathcal{T}_0 e^{-i \int_0^T dt' H(t')} \quad (1.42)$$

$$H_F = \frac{i}{T} \ln(U_F) \quad (1.43)$$

In the Hermitian Floquet theorem, U_F is assured to be unitary and as such there is assured to be an H_F that is Hermitian. For the non-Hermitian construction, U_F is non-unitary but there will be an associated non-Hermitian H_F so long as U_F is invertible. If H_F exists, then the eigenvalues will lie in a strip of the complex plane $-\pi < \text{Im}(\epsilon_F) \leq \pi$. We can then derive the Floquet energies (quasi-energies) and associated Floquet states

$$U_F |\epsilon_{Fj}\rangle = e^{-i\epsilon_{Fj}T} |\epsilon_{Fj}\rangle \quad (1.44)$$

$$\langle\langle \epsilon_{Fj} | U_F = e^{-i\epsilon_{Fj}T} \langle\langle \epsilon_{Fj} | \quad (1.45)$$

The total time evolution can then be expressed as

$$U(t + nT) = \mathcal{T}_0 e^{-i \int_0^t dt' H(t')} (U_F)^{\frac{nT}{T}} \quad (1.46)$$

$$= P(t) (U_F)^{\frac{t+nT}{T}} \quad (1.47)$$

The operator $P(t) = \mathcal{T}_0 e^{-i \int_0^t dt' H(t')} (U_F)^{-\frac{t}{T}}$ is a periodic micro-motion operator ($P(T) = \mathbb{1}$) that perturbs the evolution of the Floquet states towards the expected state. The time evolution of a general state $|\psi\rangle$ can then be expressed as a linear combination of the perturbed Floquet states

$$U(t + nT) |\psi\rangle = \sum_j e^{-i\epsilon_{Fj}(t+nT)} P(t) |\epsilon_{Fj}\rangle \langle\langle \epsilon_{Fj} | \psi \rangle \quad (1.48)$$

1.5 Physical Questions

In this chapter we have provided a mathematically consistent description for open quantum systems in a non-Hermitian setting. Experimental demonstrations of \mathcal{PT} -Symmetric

behavior including purely real spectra, exceptional points, and non-orthogonal eigenstates have been observed in [3], [6], [17], [18]. What remains is how to interpret these non-Hermitian phenomena in a physically consistent model of quantum mechanics. Obviously the interpretation of complex components of ϵ_j as energy transfer to/from the system implies secondary systems that act as a source/sink respectively, all of which must be described by some set of unitary dynamics when considered together. In addition, the fact that the identity for a system changes implies that the trace of a density matrix defined by $\rho = \sum_j p_j |\epsilon_j\rangle \langle \epsilon_j|$ does not remain normalized to $\text{Tr}(\rho) = 1$, and so such a density matrix can no longer be interpreted as a statistical distribution of states.

In the following chapters we will investigate models of decoherent evolution, and find that under specific circumstances coherent but non-unitary dynamics arise. We will then relate these dynamics to non-Hermitian models and give a physical interpretation to \mathcal{PT} -Symmetry and Pseudo-hermiticity in their context.

2. OPEN QUANTUM MAPS

In Chapter 1 we found that non-Hermitian Hamiltonians described non-conservative processes which maintain coherence, and developed the mathematical tools to analyze such systems. This identification as non-conservative dynamics then naturally calls for a comparison to quantum maps, which have been used to describe decoherent processes for decades [19], [20]. In this chapter we will introduce the Gorini–Kossakowski–Sudarshan–Lindblad master equation (Lindbladian) in preparation for Chapter 4, where we show that under specific circumstances the Lindbladian is reduced to one of the possible master equations for non-Hermitian systems. Such circumstances allow for the study of non-Hermitian Hamiltonians through established Lindbladian experiments, and so we will develop our preferred experimental apparatus in the Chapter 3.

2.1 Quantum Maps

Central to the study of decoherent processes are quantum maps (quantum channels) [19], [21]. A quantum map is defined as a linear map between two state density operators

$$\rho_f = \mathcal{M}[\rho_0] \tag{2.1}$$

where $\mathcal{M}[\cdot]$ is a general map, ρ_0 is the initial state density, and ρ_f is the resulting state density. We can see that \mathcal{M} is a linear function that accepts operators as inputs and outputs another operator, and so is an operator on operator-spaces. We will refer to such “operators-of-operators” as *super-operators*, and will denote them in this work with caligraphic text (\mathcal{M} instead of M). We will note that in the general theory of quantum maps ρ_0 and ρ_f do not need to be the same rank, but for this work we are specifically interested in maps that are automorphic.

As for the state density operators, we normally declare that the operator-space uses an orthogonal Hilbert space as a basis. Doing so makes the definition of the state density unambiguous

$$\rho = \sum_{i,j} p_{ij} |\psi_i\rangle \langle \psi_j| \quad (2.2)$$

$$\text{Tr}(\rho) = \sum_j p_{jj} \quad (2.3)$$

where $|\psi_j\rangle\rangle = |\psi_j\rangle$ and $\langle \psi_i|\psi_j\rangle = \delta_{ij}$ since we have returned to the Hermitian regime. In addition, we normally set $\text{Tr}(\rho) = 1$ so that p_{jj} correspond to probabilities. From these definitions, we can express a measurement with respect to a Hermitian operator Q as

$$\langle Q \rangle = \frac{\text{Tr}(Q\rho)}{\text{Tr}(\rho)} \quad (2.4)$$

To proceed further we will need to specify the mathematical form of \mathcal{M} , however the map can take a few alternate representations (each with their own uses). At the end of this section, Table 2.1 will then compile the properties of each form.

2.1.1 Operator Sum Representation

From Eq.2.2 we can see that the standard representation of the state density operators are square matrices. As a result, for a map to access all of the elements of ρ individually the map must include a transformation from both the left and right of ρ . The map then takes the form of a sum of transformations

$$\rho_f = \sum_{\alpha=1}^{d_0^2} L_\alpha \rho_0 R_\alpha^\dagger \quad (2.5)$$

where L_α and R_α are matrices with dimensions $D_f \times D_0$. All quantum maps require a maximum of d_0^2 pairs of $\{L_\alpha, R_\alpha\}$ to fully describe the map, though some maps will require fewer. We will denote quantum maps in the operator sum representation by the attached square brackets $\mathcal{M}[\cdot]$.

The value of the Operator Sum representation is its simplicity. The form of the map mirrors the unitary evolution of the state density $\rho_f = U\rho_0U^\dagger$, a property which we will utilize in the next section to define Kraus operators. The form of Q in the Heisenberg representation can be quickly derived

$$Q_f = \sum_{\alpha=1}^{d_0^2} R_\alpha^\dagger Q_0 L_\alpha \quad (2.6)$$

Whether or not the map is trace preserving can be obtained as

$$\text{Tr}(\rho_f) = \text{Tr}(\rho_0) \iff \sum_{\alpha=1}^{d_0^2} R_\alpha^\dagger L_\alpha = \mathbb{1} \quad (2.7)$$

The map is only hermiticity preserving when

$$\rho_f^\dagger = \rho_f \quad \forall \quad \rho_0^\dagger = \rho_0 \iff L_\alpha = \pm R_\alpha \quad \forall \quad \alpha \quad (2.8)$$

and the map is only positive when

$$\rho_f \geq 0 \quad \forall \quad \rho_0 \geq 0 \iff L_\alpha = R_\alpha \quad \forall \quad \alpha \quad (2.9)$$

2.1.2 Vectorized Representation

Since the quantum map is linear in ρ , it stands to reason that the elements of ρ can be rearranged into a vector that is more easily addressed. One possible method for accomplishing this is to transform $|\psi_i\rangle\langle\psi_j| \rightarrow |\psi_j\rangle^* \otimes |\psi_i\rangle$, which will stack the columns of ρ on top of each other

$$\rho = \begin{bmatrix} a & b \\ c & d \end{bmatrix} \rightarrow |\rho\rangle = \begin{bmatrix} a \\ c \\ b \\ d \end{bmatrix} \quad (2.10)$$

We then denote the vectorized form of ρ using the ket notation. This transformation then alters transformation from the left and right as per

$$A\rho \rightarrow (\mathbb{1} \otimes A) |\rho\rangle \quad (2.11)$$

$$\rho A \rightarrow (A^T \otimes \mathbb{1}) |\rho\rangle \quad (2.12)$$

Thus the form of \mathcal{M} will be a $d_f^2 \times d_0^2$ matrix that is generally non-Hermitian and non-unitary

$$|\rho_f\rangle = \mathcal{M} |\rho_0\rangle = \sum_{\alpha}^{d_0^2} (R_{\alpha}^* \otimes L_{\alpha}) |\rho_0\rangle \quad (2.13)$$

We will denote quantum maps in the vectorized representation without attached square brackets.

The advantage of the Vectorized representation is that the map can be manipulated and analyzed using the standard linear algebra techniques [7], [19]. Since the state density operators transform as $\rho \rightarrow |\rho\rangle$, it follows that measurement operators Q transform as

$$Q = \begin{bmatrix} a & b \\ c & d \end{bmatrix} \rightarrow \langle Q| = \begin{bmatrix} a & b & c & d \end{bmatrix} \quad (2.14)$$

$$\langle Q\rangle = \langle Q|\rho\rangle \quad (2.15)$$

If $d_f = d_0$ then the exponential is well defined

$$e^{\mathcal{M}} = \sum_{n=0}^{\infty} \frac{1}{n!} \mathcal{M}^n \quad (2.16a)$$

and the logarithm of \mathcal{M} exists if \mathcal{M} is invertible, and is well defined if $\mathcal{M} > 0$

$$\ln(\mathcal{M}) = - \sum_{n=1}^{\infty} \frac{1}{n} (\mathbb{1} - \mathcal{M})^n \quad (2.16b)$$

Further, the normal modes of the map can be obtained through eigen-decomposition

$$\mathcal{M} |\rho_j\rangle = \lambda_j |\rho_j\rangle \quad (2.17a)$$

$$\langle\langle Q_j | \mathcal{M} = \lambda_j \langle\langle Q_j | \quad (2.17b)$$

where $|\rho_j\rangle$ correspond to eigen-densities of \mathcal{M} , while $\langle\langle Q_j |$ correspond to eigen-measurements for \mathcal{M} .

2.1.3 Choi Representation

The final form of \mathcal{M} we will investigate arises when applying the vectorization procedure to L_α and R_α rather than ρ and Q . Consider the $(d_f d_0) \times (d_f d_0)$ matrix constructed from the vectorized forms of L_α and R_α

$$\Upsilon_{\mathcal{M}} = \sum_{\alpha}^{d_0^2} |L_\alpha\rangle \langle R_\alpha^\dagger| \quad (2.18)$$

where $\langle R_\alpha^\dagger| = (|R_\alpha\rangle)^\dagger$. One can show that this matrix is equivalent to the action of $\mathcal{M}[\cdot]$ acting on one subsystem of a maximally entangled system plus ancilla

$$\Upsilon_{\mathcal{M}} = \sum_{i,j} |\psi_i\rangle \langle \psi_j| \otimes \mathcal{M}[|\psi_i\rangle \langle \psi_j|] = (\mathbb{1}_{d_0} \otimes \mathcal{M}) [|\Omega\rangle \langle \Omega|] \quad (2.19)$$

where $|\Omega\rangle = \sum_j |\psi_j\rangle \otimes |\psi_j\rangle$. Further, it can be shown that

$$\rho_f = \text{Tr}_{d_0} \left(\Upsilon_{\mathcal{M}} \left(\rho_0^T \otimes \mathbb{1}_{d_f} \right) \right) \quad (2.20)$$

where $\text{Tr}_{d_0}(\cdot)$ is the partial trace over the system that is not acted on by $\mathcal{M}[\cdot]$ (see Appendix A).

The value of the Choi representation lies in its mathematical properties [19], [20]. Like the Operator Sum representation, we can determine if \mathcal{M} is trace preserving through

$$\text{Tr}(\rho_f) = \text{Tr}(\rho_0) \iff \text{Tr}_{d_f}(\Upsilon_{\mathcal{M}}) = \mathbb{1}_{d_0} \quad (2.21)$$

Table 2.1. Table comparing the useful properties of each of the representations of the quantum map \mathcal{M} .

	Operator	Vectorized	Choi
Notation	$\mathcal{M}[\cdot]$	\mathcal{M}	$\Upsilon_{\mathcal{M}}$
ρ_f	$\mathcal{M}[\rho]$	$\mathcal{M} \rho\rangle$	$\text{Tr}_{d_0}\left(\Upsilon_{\mathcal{M}}\left(\rho_0^T \otimes \mathbb{1}_{d_f}\right)\right)$
$\langle Q \rangle$	$\text{Tr}(Q\mathcal{M}[\rho])$	$\langle Q \mathcal{M} \rho \rangle$	$\text{Tr}\left(\Upsilon_{\mathcal{M}}\left(\rho_0^T \otimes Q\right)\right)$
Exponent	x	$e^{\mathcal{M}}$	x
Logarithm	x	$\ln(\mathcal{M})$	x
Trace	$\sum_{\alpha=1}^{d_0^2} R_{\alpha}^{\dagger} L_{\alpha} = \mathbb{1}$	x	$\text{Tr}_{d_f}(\Upsilon_{\mathcal{M}}) = \mathbb{1}_{d_0}$
Hermiticity	$L_{\alpha} = \pm R_{\alpha}$	x	$\Upsilon_{\mathcal{M}}^{\dagger} = \Upsilon_{\mathcal{M}}$
Positivity	$L_{\alpha} = R_{\alpha}$	x	$\Upsilon_{\mathcal{M}} \geq 0$
Decomposition	x	Eigen- ρ , Eigen- Q	Minimal L_{α} , R_{α}

and the map is only hermiticity preserving when

$$\rho_f^{\dagger} = \rho_f \quad \forall \quad \rho_0^{\dagger} = \rho_0 \iff \Upsilon_{\mathcal{M}}^{\dagger} = \Upsilon_{\mathcal{M}} \quad (2.22)$$

The Choi representation can also be used to determine if the map is *completely positive* (positive semidefinite for all extended systems) through

$$\rho_f \geq 0 \quad \forall \quad \rho_0 \geq 0 \iff \Upsilon_{\mathcal{M}} \geq 0 \quad (2.23)$$

In addition, the Choi rank ($\text{rank}(\Upsilon_{\mathcal{M}})$) corresponds to the minimum pairs of L_{α} and R_{α} required to recreate the map, and the individual L_{α} and R_{α} are obtained from the eigen-decomposition of $\Upsilon_{\mathcal{M}}$.

2.2 Kraus Maps

We are now in a position to derive the quantum maps which govern physical systems. Starting from a state-density operator for the universe ρ_{uni} , we can split ρ_{uni} into a subsystem

we are interested in ρ and the surrounding environment, which we will consider to be in the ground state

$$\rho_{uni} = \rho \otimes |0\rangle \langle 0| \quad (2.24)$$

We specify that the environment must be in the ground state so that the environment is incapable of supplying energy to the system in question. ρ_{uni} is considered to be a completely closed system, and so it evolves under unitary evolution

$$\rho_{uni}(t) = U (\rho(t_0) \otimes |0\rangle \langle 0|) U^\dagger \quad (2.25)$$

From this point we remove the degrees of freedom for the environment by partial tracing over the states of the environment $|\alpha\rangle$, leaving us with a quantum map in the operator sum representation

$$\rho(t) = \mathcal{V}[\rho(t_0)] = \sum_{\alpha=0}^{d_e} K_\alpha \rho(t_0) K_\alpha^\dagger = \sum_{\mu=0}^{d_K} K_\mu \rho(t_0) K_\mu^\dagger \quad (2.26)$$

where $K_\alpha = \langle \alpha|U|0\rangle$ are referred to as Kraus operators. We write the second summation in Eq.2.26 as the maximum number of Kraus operators is $d_K \leq d_\rho^2$, and so the set of K_α may not be linearly independent. Instead, the index μ runs over the minimal set of Kraus operators. We can also see that \mathcal{V} is trace preserving, hermiticity preserving, and completely positive as per the properties of the Operator Sum representation.

2.2.1 Markovianity

We can see from the form of K_α that each of the Kraus operators is responsible for exciting the environment from the ground state to an excited state $|\alpha\rangle$. Since U is unitary and creates entanglements between the system and environment, this will be accompanied by a change in the purity of ρ . Beginning in a short timescale the change will be highly volatile, then will transition to a largely decoherent regime, before becoming oscillatory at

long times. The one exception is K_0 , which does not excite the environment and so drives coherent evolution within ρ .

The logical problem that this creates is that we would like to connect \mathcal{V} to a generating master equation \mathcal{L} in the same way that U and H are connected. However since U is unitary the entanglement between the system and environment will mean that $\rho(t + \delta t)$ generally depends on $\rho(t)$ and ρ at earlier times, since the information of such states exists in the environment. To overcome these complications, it is necessary that we take a Markov approximation of the model [22]–[25]. This approximation assumes:

$$\delta t_{mem} \gg \delta t_{msr} \gg \delta t_{dyn} \gg \delta t_{rch} \quad (2.27)$$

1. The environment is large enough, or sufficiently noisy enough, that there is a time scale δt_{mem} at which information in the environment is lost. Thus, any back-action of the environment on the system is generated from incoherent dynamics.
2. The timescale of measurements δt_{msr} is large enough that random noise is averaged over.
3. The timescale of the dynamics we are interested in studying δt_{dyn} is large compared to δt_{msr} , but small compared to the recoherence timescale δt_{rch} .

If the system satisfies these conditions we can approximate \mathcal{V} to be Markovian by requiring that the environment is reset to its ground state after any excitation occurs. Markovian maps are local in time so that $\rho(t + \delta t)$ depends on $\rho(t)$ alone. In addition, Markovian maps allow for sequential application of $\mathcal{V}[\cdot]$ to yield the proper evolved $\rho(t)$

$$\rho(t + 2dt) = \mathcal{V}[\rho(t + \delta t)] = \mathcal{V}[\mathcal{V}[\rho(t)]] \quad (2.28)$$

Not all Kraus maps are Markovian, but we can check whether a map is by using the Choi matrix so long as the map is known to be trace preserving and completely positive [25]

$$\|\Upsilon_{\mathcal{V}}\| = \text{Tr} \sqrt{\Upsilon_{\mathcal{V}}^\dagger \Upsilon_{\mathcal{V}}} \geq 1 \quad (2.29)$$

where $\|\Upsilon_{\mathcal{M}}\|$ is the trace norm of $\Upsilon_{\mathcal{M}}$. In the instance that $\|\Upsilon_{\mathcal{V}}\| = 1$ the map is Markovian. However if $\|\Upsilon_{\mathcal{V}}\| > 1$ then non-Markovian effects will be present and no master equation can be written.

2.2.2 Lindblad Master Equation

With the Markovian condition on \mathcal{V} we can now tackle defining a master equation for open systems. Our goal will be to define the generator of decoherent evolution \mathcal{L} , as well as relate this generator to the quantum von-Liouville equation $\imath\partial_t\rho = [H, \rho]$ which \mathcal{L} should approach for unitary evolution.

To begin, we expand the corrections to $\rho(t + \delta t)$ in orders of δt

$$\rho(t + \delta t) = \mathcal{V}[\rho(t)] = \sum_{\alpha=0}^{d_e} K_{\alpha}(\delta t)\rho(t)K_{\alpha}^{\dagger}(\delta t) \quad (2.30)$$

Since \mathcal{V} is Markovian, we expect the first order to yield the largest correction as $dt \rightarrow 0$. First, we separate the contribution of K_0 from the other K_{α} as K_0 should be associated with coherent evolution. We specify that $K_0 = \mathbb{1} + \delta t(-\imath H + C) + O(\delta t^2)$, where C is a correction operator which will be needed later. Expanding the Kraus operators in terms of $\sqrt{\delta t}$ yields corrections $K_{\alpha}(\delta t) = L_{\alpha,0} + \sqrt{\delta t}L_{\alpha,1} + O(\delta t)$ Substituting the first order corrections for K_{α} then yields

$$\rho(t + \delta t) = \rho(t) + \delta t \left(-\imath[H, \rho(t)] + \{C, \rho(t)\} + \sum_{\alpha=1}^{d_e} L_{\alpha,1}\rho(t)L_{\alpha,1}^{\dagger} \right) + O(\delta t^2) \quad (2.31)$$

Next, we require that \mathcal{V} be trace preserving. Since $\text{Tr}(\rho(t + \delta t)) = \text{Tr}(\rho(t)) = 1$, this requires that all correction orders obey $\text{Tr}(O(\delta t^n)) = \delta_{0n}$. This is only possible for all correction orders if $C = -\frac{1}{2}\sum_{\alpha=1}^{d_e} L_{\alpha,1}^{\dagger}L_{\alpha,1}$. As a final step, we remove the linearly dependent members of the $L_{\alpha,1}$ set by replacing them with the normalized set $\sqrt{\gamma_{\mu}}L_{\mu}$.

Finally, we are left with the Gorini– Kossakowski– Sudarshan– Lindblad master equation (Lindbladian)

$$\partial_t \rho = \mathcal{L}[\rho] = -i \underbrace{[H, \rho]}_{(1)} + \sum_{\mu} \gamma_{\mu} \underbrace{L_{\mu} \rho L_{\mu}^{\dagger}}_{(2)} - \frac{\gamma_{\mu}}{2} \underbrace{\{L_{\mu}^{\dagger} L_{\mu}, \rho\}}_{(3)} \quad (2.32)$$

where the set of L_{μ} are referred to as Lindblad dissipators, and γ_{μ} are the associated decay rates. Note that all the decay rates must be $\gamma_{\mu} \geq 0$ for \mathcal{L} to remain completely positive. The set of L_{μ} are usually normalized so that they are traceless and are Hilbert-Schmidt orthogonal

$$\text{Tr}(L_{\mu}) = 1 \quad (2.33a)$$

$$\text{Tr}(L_{\mu}^{\dagger} L_{\nu}) = \delta_{\mu\nu} \quad (2.33b)$$

The commutator(1) is identical to the quantum von-Liouville equation, and since H is Hermitian this term will generate unitary dynamics in $\rho(t)$. The second term(2) is similar to the Kraus map and so this term is responsible for the decoherent “jumps” that occur [7]. The anti-commutator(3) which was required for trace preservation of the map was an anti-Hermitian component of K_0 originally, and so this term will generate coherent but non-unitary dynamics.

By transforming $\mathcal{L}[\cdot]$ to the vectorized representation, we can quickly determine the eigen-densities and eigen-measurements

$$L_{\mu} |\rho_j\rangle = \lambda_j |\rho_j\rangle \quad (2.34a)$$

$$\langle\langle Q_j | L_{\mu} = \lambda_j \langle\langle Q_j | \quad (2.34b)$$

Since \mathcal{L} is trace preserving, we know that one $\langle\langle Q_{ss} | = \mathbb{1}$ with eigenvalue $\lambda_{ss} = 0$ since $\text{Tr}(\rho(t)) \rightarrow \langle\langle \mathbb{1} | \rho(t) \rangle\rangle$ in the vectorization representation. λ_{ss} will then have an associated eigen-density

$$\mathcal{L} |\rho_{ss}\rangle = 0 \quad (2.35)$$

which represents the steady state density of the system [7], [26], [27]. The rest of the λ_j will exist in the $\text{Re}(\lambda_j) \leq 0$ half plane, and must be purely real or come in complex conjugate pairs. The associated $|\rho_j\rangle$ will be Hermitian if λ_j is real, or come in Hermitian conjugate pairs if λ_j is complex. In addition, since $\langle \mathbb{1} |$ is a member of the $\langle\langle Q_j |$, and $\langle\langle Q_j |$ and $|\rho_j\rangle$ form a bi-orthogonal set, all $|\rho_j\rangle$ other than $|\rho_{ss}\rangle$ must obey

$$\text{Tr}(\rho_j) = 0 \quad \forall \quad j \neq ss \quad (2.36)$$

There are two circumstances in which the steady state properties are violated. The first is if complex conjugate pairs exist with $\text{Re}(\lambda_j) = 0$ [26], [27]. In these cases $\rho(t)$ will oscillate between multiple steady states. This behavior is expected in the unitary limit, but is rare when $\gamma_\mu \neq 0$. The second is if \mathcal{L} lies on an exceptional point [7]. Under this condition \mathcal{L} will have degenerate eigen-densities similar to the case found in non-Hermitian Hamiltonians. In these cases, we use the Jordan decomposition found in Ch.1 to determine the additional vectors needed for \mathcal{V} [1].

2.3 Fundamental Case: Decohering Dimer

We now consider the case of the Decohering Dimer \mathcal{L}_2 . For the Lindblad dissipators we will use the basis

$$L_z = \frac{1}{2}\sigma_z, \quad L_+ = \sigma_+, \quad L_- = \sigma_- \quad (2.37)$$

L_z corresponds to phase noise, and will cause $\langle \sigma_x \rangle$ and $\langle \sigma_y \rangle$ to decay toward zero. $L_-(L_+)$ corresponds to spontaneous emission (absorption), and will cause ρ to decay toward $|\downarrow\rangle\langle\downarrow|$ ($|\uparrow\rangle\langle\uparrow|$). For the Hermitian component of \mathcal{L}_2 , we choose

$$H = \frac{J}{2}\sigma_x \quad (2.38)$$

while a more general case would include the detuning potential $\frac{\Delta}{2}\sigma_z$. We choose this H as (much like the \mathcal{PT} -dimer) choosing a coupling orthogonal to the natural alignment of the

dissipators yields ideal properties for λ_j and ρ_j . Figure 2.1 shows a possible implementation of \mathcal{L}_2 in a two level transmon circuit

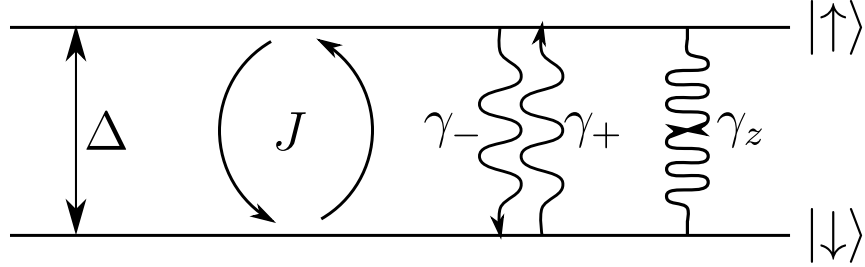


Figure 2.1. Decohering Dimer: Shows an energy level diagram for a decohering two level transmon, where $\frac{J}{2}$ is a microwave drive and Δ is the energy level difference between $|\uparrow\rangle$ and $|\downarrow\rangle$. There are 3 forms of dissipation present in the model consisting of spontaneous emission (γ_-), spontaneous absorption (γ_+), and phase noise (γ_z). Unlike in Fig.1.1b the dissipation of the Decohering Dimer is internal to the two level manifold, and thus the effects of decoherent jumps remain present [15].

The Lindbladian in the Operator Sum representation reads as

$$\mathcal{L}_2[\rho] = -\frac{iJ}{2}[\sigma_x, \rho] + \sum_{\mu=z,\pm} \gamma_\mu \mathcal{D}_\mu[\rho] \quad (2.39a)$$

$$\mathcal{D}_z[\rho] = \frac{1}{4}\sigma_z\rho\sigma_z - \frac{1}{4}\rho \quad (2.39b)$$

$$\mathcal{D}_+[\rho] = \sigma_+\rho\sigma_- + \frac{1}{4}(\sigma_z\rho + \rho\sigma_z) - \frac{1}{2}\rho \quad (2.39c)$$

$$\mathcal{D}_-[\rho] = \sigma_-\rho\sigma_+ - \frac{1}{4}(\sigma_z\rho + \rho\sigma_z) - \frac{1}{2}\rho \quad (2.39d)$$

and the vectorized representation reads as

$$\mathcal{L}_2 = \frac{1}{2} \begin{bmatrix} -2\gamma_- & -iJ & iJ & 2\gamma_+ \\ -iJ & -(\gamma_z + \gamma_+ + \gamma_-) & 0 & iJ \\ iJ & 0 & -(\gamma_z + \gamma_+ + \gamma_-) & -iJ \\ 2\gamma_- & iJ & -iJ & -2\gamma_+ \end{bmatrix} \quad (2.40)$$

As with all Lindbladian systems there is a steady state corresponding to $\lambda_{ss} = 0$ associated with $Q_{ss} = \mathbb{1}$

$$\rho_{ss} = \frac{1}{2} \begin{bmatrix} 1 + r \cos(\theta) & -ir \sin(\theta) \\ ir \sin(\theta) & 1 - r \cos(\theta) \end{bmatrix} \quad (2.41)$$

where $r = \frac{\gamma_+ - \gamma_-}{J^2 - \lambda_0(\gamma_+ + \gamma_-)}$ and $\tan(\theta) = \frac{J}{\lambda_0}$. We can see from the form of ρ_{ss} that the system always decays to a point that lies in the yz -plane. The constant $\lambda_0 = -\frac{\gamma_+ + \gamma_- + \gamma_z}{2}$ corresponds to the second eigenvalue, which is associated with

$$\rho_0 = \frac{1}{2} Q_0 = \frac{1}{2} \begin{bmatrix} 0 & 1 \\ 1 & 0 \end{bmatrix} \quad (2.42)$$

ρ_0 is unusual as it is the only self-orthogonal member of the biorthogonal sets ρ_j and Q_j . Its form implies that there is an exponential decay of $\langle \sigma_x \rangle$ with time, which explains why ρ_{ss} has no x -component.

The final two λ_j exist as a pair

$$\lambda_{\pm} = \lambda_0 - J e^{\pm \zeta} \quad (2.43a)$$

$$Q_{\pm} = \begin{bmatrix} r(\cos(\theta) - e^{\mp \zeta} \sin(\theta)) - 1 & -ie^{\mp \zeta} \\ ie^{\mp \zeta} & r(\cos(\theta) - e^{\mp \zeta} \sin(\theta)) + 1 \end{bmatrix} \quad (2.43b)$$

$$\rho_{\pm} = \frac{1}{4 \sinh(\zeta)} \begin{bmatrix} -e^{\pm \zeta} & i \\ -i & e^{\pm \zeta} \end{bmatrix} \quad (2.43c)$$

where $\cosh(\zeta) = -\frac{\lambda_0 + \gamma_z}{2J}$. When $\left| \frac{\gamma_z + \lambda_0}{2J} \right| > 1$ then λ_{\pm} are purely real and both ρ_{\pm} and Q_{\pm} are Hermitian. On the other hand, when $\left| \frac{\lambda_0 + \gamma_z}{2J} \right| < 1$ the $\lambda_{\pm}^* = \lambda_{\mp}$ and so both $\rho_{\pm}^{\dagger} = \rho_{\mp}$ and $Q_{\pm}^{\dagger} = Q_{\mp}$. At the point when $\left| \frac{\lambda_0 + \gamma_z}{2J} \right| = 1$ the pairs become degenerate and \mathcal{L} is not full rank.

Figure 2.2 shows the progression of λ_j as J increases from $0 \rightarrow 5$ for $\gamma_z = .25$, $\gamma_+ = .75$, and $\gamma_- = .5$. Figure 2.2a shows the λ_j , while Figure 2.2b shows the eigenvalues of \mathcal{V} ($e^{\lambda_j t}$) for $t = 1$. The steady state λ_{ss} is shown as the unmoving black dot. Since all of the

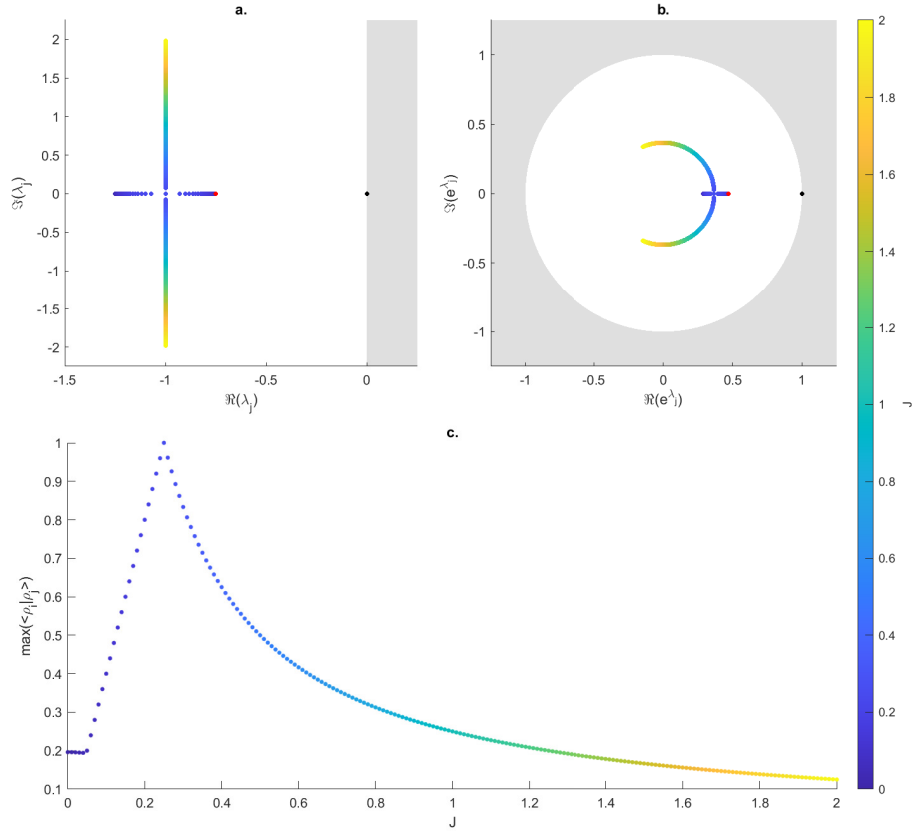


Figure 2.2. Decohering Dimer Eigenvalues: Shows the eigenvalue spectrum for a Decohering Dimer with $\gamma_z = .25$, $\gamma_+ = .75$, $\gamma_- = .5$ and varying J . Figure 2.2a shows the position of λ_j in the complex plane, while Figure 2.2b shows the eigenvalues of $\mathcal{V}_2(e^{\lambda_j t})$ when $t = 1$. The region of the complex plane that the eigenvalues cannot exist in is shaded gray. The steady state $\lambda_{ss} = 0$ is marked in black. $\lambda_0 = -\frac{\gamma_+ + \gamma_- + \gamma_z}{2}$ is marked in red. The remaining pair λ_{\pm} is marked with the color gradient blue \rightarrow yellow. λ_+ and λ_- initially lie on the real axis, but become degenerate at $\left| \frac{2J}{\lambda_0 + \gamma_z} \right| = 1$ after which they form a complex conjugate pair. The corresponding $e^{\lambda_+ t}$ and $e^{\lambda_- t}$ wind around the origin, but do not become degenerate at larger J . The non-orthogonal character of the ρ_j is tracked in Figure 2.2c.

γ_μ are constant, λ_0 is shown by the unmoving red dot. The remaining pair λ_\pm change as J is increased, and so are shown with the color gradient blue→yellow. The pair is initially real valued before becoming degenerate at $J = \frac{1}{4}$, and then split off the real axis as complex conjugates. The forbidden region of the Lindbladian is shown shaded gray. Finally, Figure 2.2c shows the overlap of eigen-densities $\max(\langle \rho_i | \rho_j \rangle)$. Unlike with the \mathcal{PT} -dimer, the system begins with a small degree of non-orthogonality. The maximum overlap then becomes dominated by $\langle \rho_+ | \rho_- \rangle$, raising as ρ_+ and ρ_- become degenerate. The behavior of the maximum overlap falls off as $J \rightarrow \infty$, signifying that \mathcal{L} is approaching the unitary limit.

Figure 2.3 shows time evolution of a general pure state density. The position of $\rho(t)$ within the Bloch sphere is tracked using the color gradient line. The chosen γ_μ and J are such that the evolution of the state density toward the steady state is critically damped. For higher values of J $\rho(t)$ will spiral around the steady state, while lower values will cause $\rho(t)$ to curve less but be pulled at a slower rate.

2.4 Floquet Analysis for Quantum Maps

Similar to non-Hermitian Hamiltonians, we can define a Floquet Analysis for quantum maps [16], [25]. For a quantum map parametrized by time dependent parameters the final map is the composition of the map at consecutive time instances, which is expressed most easily in the vectorized representation

$$\mathcal{M}_T(t) = \lim_{\delta t \rightarrow 0} \mathcal{M}(t, t - \delta t) \cdots \mathcal{M}(\delta t, 0) \quad (2.44a)$$

$$= \prod_0^t \mathcal{M}(t')^{dt'} \quad (2.44b)$$

$$\mathcal{V}(t) = \mathcal{T}_o e^{\int_0^t dt' \mathcal{L}(t')} \quad (2.44c)$$

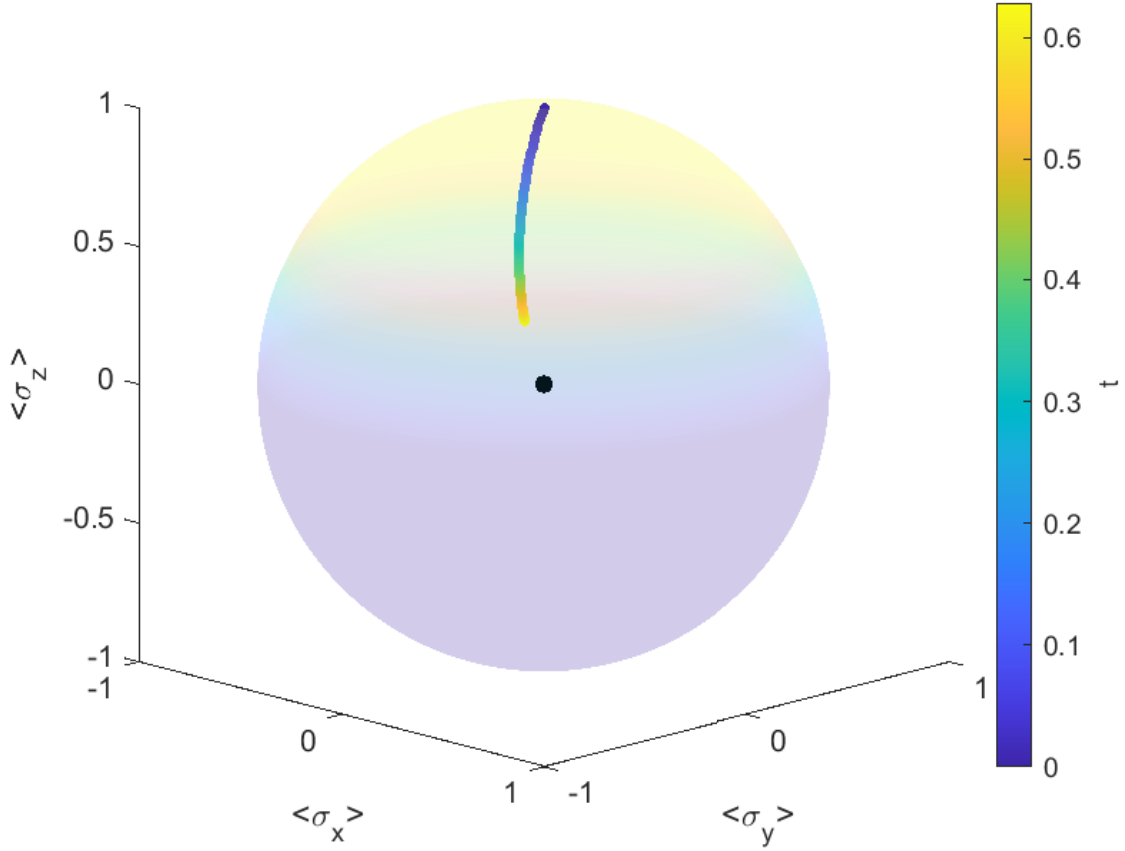


Figure 2.3. Evolution of the Decohering Dimer: Shows the evolution of the state density $\rho(0) = |\uparrow\rangle\langle\uparrow|$ under \mathcal{L}_2 when $\gamma_z = 6$, $\gamma_+ = 1$, $\gamma_- = 1$, and $J = 1$. The outline of the Bloch sphere is shown with a transparent gradient. The steady state the system approaches at $t \rightarrow \infty$ is the maximally mixed state, shown here as the black dot at the center of the Bloch Sphere. As t increases $\mathcal{V}_2|\rho(0)\rangle$ is traced using the color gradient line. The specific combination of coupling strength and decay rates means that \mathcal{L}_2 is critically damped, meaning that $\lambda_+ = \lambda_-$ and $\rho(t)$ will approach ρ_{ss} as fast as possible for the given γ_μ

If the Lindbladian is periodic in time ($\mathcal{L}(t + nT) = \mathcal{L}(t)$) then we can define a Floquet map \mathcal{V}_F , Floquet-densities ρ_{Fj} , and Floquet-measurements Q_{Fj}

$$\mathcal{V}_F = \mathcal{T}_0 e^{-\int_0^T dt' \mathcal{L}(t')} \quad (2.45)$$

$$\mathcal{V}(t + nT) = \mathcal{P}(t) (\mathcal{V}_F)^{\frac{t+nT}{T}} \quad (2.46)$$

$$\mathcal{V}_F |\rho_{Fj}\rangle = e^{\lambda_{Fj} T} |\rho_{Fj}\rangle \quad (2.47)$$

$$\langle\langle Q_{Fj} | \mathcal{V}_F = e^{\lambda_{Fj} T} \langle\langle Q_{Fj} | \quad (2.48)$$

which we can use to express the evolution of a general state density

$$|\rho(t)\rangle = \mathcal{V}(t + nT) |\rho(0)\rangle = \sum_j e^{\lambda_{Fj}(t+nT)} \mathcal{P}(t) |\rho_{Fj}\rangle \langle\langle Q_{Fj} | \rho(0)\rangle \quad (2.49)$$

The one major difference that exists for Floquet maps is the existence of a Floquet Lindbladian [25]

$$\mathcal{L}_F \stackrel{?}{=} \frac{1}{T} \ln(\mathcal{V}_F) \quad (2.50)$$

For the Hamiltonian case U_F and H_F were simply operators, and so the only restriction on the existence of H_F was that U_F be invertible. However, for the Lindbladian case \mathcal{V}_F must additionally be trace preserving, hermiticity preserving, completely positive, and Markovian. The first two restrictions are generally not in question so long as the instantaneous maps also preserve trace and hermiticity. On the other hand, the complete positivity condition can sometimes create issues when \mathcal{L}_F would require a (usually small) negative decay rate to approximate \mathcal{V} . The most common issue to arise however is the Markovianity condition, as the composition of instantaneous Markovian maps may not be Markovian itself. Due to these complications we typically analyze the properties of \mathcal{V}_F directly.

2.4.1 Floquet Lindbladians with Periodic Potentials

For our first investigation into the dynamics of Floquet Lindbladians we will focus on models in which the elements of the Hamiltonian are periodic in time. We will utilize the same 2×2 Hamiltonian with two separate periodic functions

$$H(t) = -\frac{1}{2}J(t)\sigma_x \quad (2.51)$$

$$J(t) = \begin{cases} J(1 - \delta \sin^2(\frac{\Omega}{2}t)) \\ J(1 - \delta \text{Sq}(t - \frac{\pi}{\Omega})) \end{cases} = \begin{cases} J & t < \frac{\pi}{\Omega} \\ J(1 - \delta) & t \geq \frac{\pi}{\Omega} \end{cases} \quad (2.52)$$

where $\Omega = \frac{2\pi}{T}$, $\delta \in [0, 2]$ is a parameter controlling the minimum of the coupling, and $\text{Sq}(t)$ is the function of a square wave. We will also separately use two different static Lindblad dissipators, L_- at first and L_z second. We note here that whenever a single dissipator is present the dissipator L_+ yields identical results to L_- when $|\uparrow\rangle$ is exchanged with $|\downarrow\rangle$.

First we will consider periodic modulation with spontaneous emission. The instantaneous Lindbladian $\mathcal{L}_2(t)$ in the Operator Sum representation reads as

$$\mathcal{L}_2(t)[\rho] = -i\frac{J(t)}{2}[\sigma_x, \rho] + \gamma_- \mathcal{D}_-[\rho] \quad (2.53a)$$

$$\mathcal{D}_-[\rho] = \sigma_- \rho \sigma_+ - \frac{1}{4}(\sigma_z \rho + \rho \sigma_z) - \frac{1}{2}\rho \quad (2.53b)$$

and the vectorized representation reads as

$$\mathcal{L}_2(t) = \frac{1}{2} \begin{bmatrix} -2\gamma_- & -iJ(t) & iJ(t) & 0 \\ -iJ(t) & -\gamma_- & 0 & iJ(t) \\ iJ(t) & 0 & -\gamma_- & -iJ(t) \\ 2\gamma_- & iJ(t) & -iJ(t) & 0 \end{bmatrix} \quad (2.54)$$

For \mathcal{V}_F , we need to solve Eq.2.45 to obtain an analytic form. However an analytic expression for the Dyson series under sinusoidal modulation has not been found, and so we obtain \mathcal{V}_F numerically by discretizing the integral into

$$\mathcal{V}_F = \prod_{k=1}^n \left(\sum_j e^{\frac{2\pi k}{n} \frac{\lambda_j(k)}{\Omega}} |\rho_j(k, t)\rangle \langle\langle Q_j(k, t)| \right) \quad (2.55)$$

At a discretization of $n = 100$ we obtain a close approximation of \mathcal{V}_F , though the error is higher for low $\frac{\Omega}{J}$ and large $\frac{\gamma}{J}$. We then calculate the eigenvalues $e^{\lambda_{Fj} \frac{2\pi}{\Omega}}$ and eigen-densities $|\rho_{Fj}\rangle$. In the case of the square wave modulation \mathcal{V}_F is explicitly calculable, but a simple representation like we saw with the static \mathcal{L}_2 is not available.

Based on the behavior of Figure 2.2c, we expect that $\max(\langle\rho_{Fi}|\rho_{Fj}\rangle)$ will show the system is non-orthogonal whenever $\gamma \neq 0$. The greatest non-orthogonality is expected between two eigen-densities ρ_{F+} and ρ_{F-} which will become degenerate at specific combinations of $\frac{\Omega}{J}$ and $\frac{\gamma}{J}$, while at the points $\max(\langle\rho_{F+}|\rho_{F+}\rangle) \approx 0$ small non-orthogonalities between ρ_{Fss} , ρ_{F+} , and ρ_{F-} will keep $\max(\langle\rho_{F+}|\rho_{F+}\rangle) \neq 0$. However, in the case of ρ_{F0} , we notice that $\rho_0 = \frac{1}{2}Q_0 = \frac{1}{2}\sigma_x$ is a self-orthogonal eigen-density for all instantaneous $\mathcal{L}_2(t)$, and therefore we can determine that \mathcal{V}_F will have an eigen-density corresponding to $\rho_{F0} = \rho_0$.

Figure 2.4a shows the phase diagram for periodic driving $J(t)$ and spontaneous emission rate γ for $\delta = 1$. Within the phase diagram we see the presence of exceptional points at the bright yellow lines where $\max(\langle\rho_{Fi}|\rho_{Fj}\rangle) = 1$. Along these contours ρ_{F+} and ρ_{F-} are degenerate and the system is critically damped. Between the contours lie regions of underdamped and overdamped oscillations, with the underdamped regions in contact with the unitary limit. We see all of the exceptional point contours of \mathcal{V}_F converge at the point $(\frac{\Omega}{J}, \frac{\gamma}{J}) = (0, 4)$. This convergence is a signature of the lone exceptional point of the static system \mathcal{L}_2 . Similarly, we can see the signature of the same exceptional point of \mathcal{L}_2 through the contour that approaches $(\frac{\Omega}{J}, \frac{\gamma}{J}) = (\infty, 4 - 2\delta)$. This exceptional contour exists in the high frequency limit where the changes in $J(t)$ are averaged over, resulting in an effective $J(t) \approx J \frac{2-\delta}{2}$. The rest of the exceptional point contours form into pairs as they approach the unitary limit $\frac{\gamma}{J} = 0$, where they approach points $(\frac{\Omega}{J}, \frac{\gamma}{J}) = (\frac{2-\delta}{n}, 0)$, $\forall n \in \mathbb{Z}^+$. This effect can be understood as a Lindbladian extension of the Bloch-Siegert shift [28] resulting

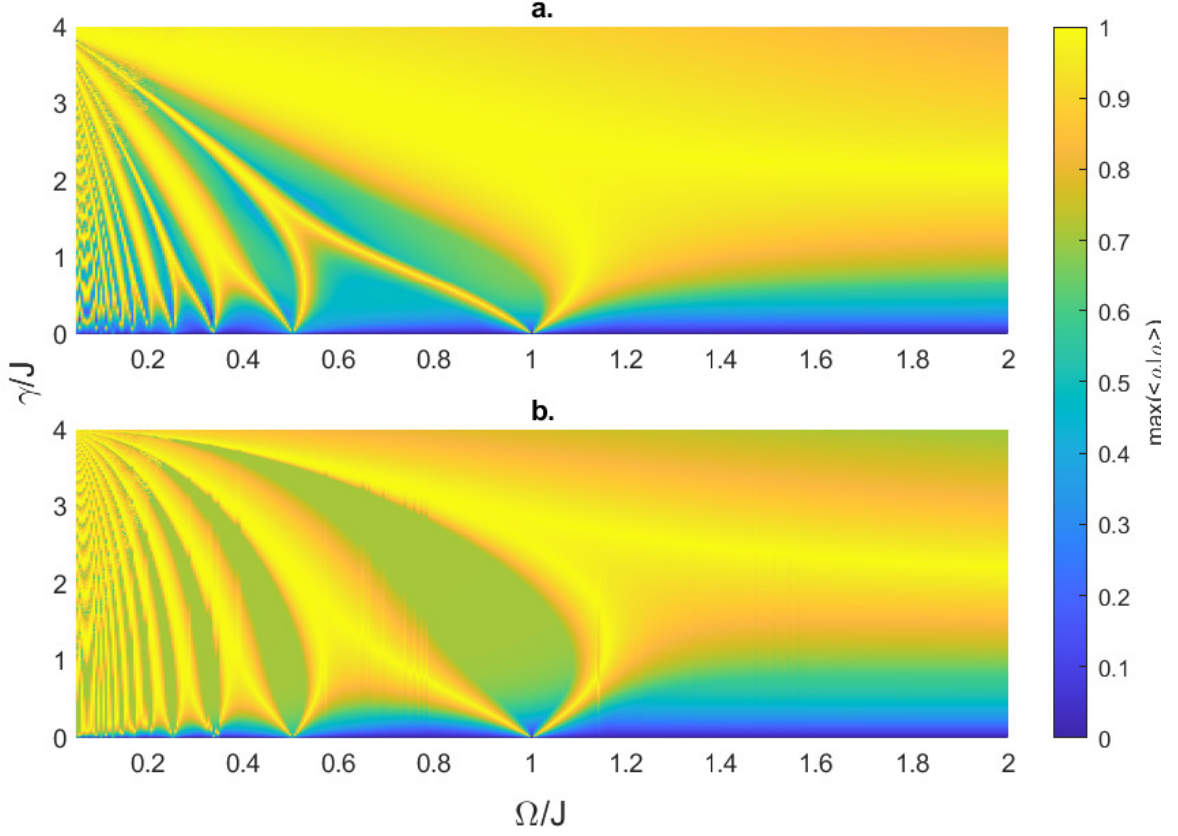


Figure 2.4. Periodic Driving with L_- Phase Diagram: Shows the maximum inner product of eigen-densities $\max(\langle \rho_{Fi} | \rho_{Fj} \rangle)$ for periodic driving $J(t)$ and spontaneous emission rate γ with $\delta = 1$. Figure 2.4a shows the sinusoidal modulation, while Figure 2.4b shows the square wave modulation. The presence of exceptional point contours is clearly seen in both cases. We see that all of the contours converge at the point $(\frac{\Omega}{J}, \frac{\gamma}{J}) = (0, 4)$, which corresponds to the exceptional point of the static system \mathcal{L}_2 . We also see that there is a contour which approaches $(\frac{\Omega}{J}, \frac{\gamma}{J}) = (\infty, 2)$, which corresponds to the same exceptional point of \mathcal{L}_2 in the high frequency regime where the motion is averaged out. The rest of the contours converge toward the unitary limit as pairs symmetrically approaching the points $(\frac{\Omega}{J}, \frac{\gamma}{J}) = (\frac{1}{n}, 0)$.

from multiphoton resonances in the traditional Rabi problem [29]–[31]. The fact that these contours approach the unitary limit allows for the exploration of exceptional point effects at lower $\frac{\gamma}{J}$ than would be possible in static systems. Furthermore, we can alter the shape of the contours within the phase diagram by changing δ . Decreasing δ will cause the underdamped regions to expand within the phase diagram rescaled by $\frac{\Omega}{J} \rightarrow \frac{\Omega}{J(2-\delta)}$, while increasing δ will cause the overdamped regions to expand.

Figure 2.5a shows the lower section of Figure 2.4a, with the dashed line at $\frac{\gamma}{J} = 0.125$ marking a path which crosses multiple exceptional point contours in the phase diagram. Figure 2.5b shows the real and imaginary components of $e^{\lambda_{F0} \frac{2\pi}{\Omega}}$, $e^{\lambda_{F+} \frac{2\pi}{\Omega}}$, and $e^{\lambda_{F-} \frac{2\pi}{\Omega}}$ along this path. We see that $e^{\lambda_{F0} \frac{2\pi}{\Omega}}$ follows a simple exponential decay as $\frac{\Omega}{J} \rightarrow 0$, beginning near the steady state $e^{\lambda_{Fss} \frac{2\pi}{\Omega}} = 1$ and decaying toward 0. Next, we see that $e^{\lambda_{F+} \frac{2\pi}{\Omega}}$ and $e^{\lambda_{F-} \frac{2\pi}{\Omega}}$ are initially a complex conjugate pair in the high frequency limit. The pair then spiral inward as $\frac{\Omega}{J} \rightarrow 0$ before becoming degenerate on the negative real axis. This case is notable as it was impossible with the static \mathcal{L}_2 , and signifies that \mathcal{L}_F would require λ_{F+} and λ_{F-} that are complex but become degenerate at opposing $\text{Im}(\lambda_{F\pm}) = \pm\pi$. After the exceptional point the $\lambda_{F\pm}$ would not form a conjugate pair after diverging. A way of rationalizing this is that $\lambda_{F\pm}$ which exist on different Riemann sheets become degenerate, resulting in $\lambda_{F\pm}$ being bound to the lines $\text{Im}(\lambda_{F\pm}) = \pm\pi$ while they are in the overdamped region **Schnell**. We see this behavior present in Figure 2.5b, where after entering the overdamped region $e^{\lambda_{F+} \frac{2\pi}{\Omega}}$ and $e^{\lambda_{F-} \frac{2\pi}{\Omega}}$ briefly diverge along the negative real axis before rebounding to coalesce again closer to $e^{\lambda_F \frac{2\pi}{\Omega}} = 0$. At this point, the system enters a different underdamped region and the behavior repeats again on the positive real axis. This cycle repeats as $\frac{\Omega}{J} \rightarrow 0$ while the eigenvalues spiral inward, with overdamped regions of odd n on the negative real axis and even n on the positive axis.

Taking a path further from the unitary limit results in larger deviations along the real axis, but pulls the entire structure inward making the paths overlap and harder to resolve. In fact, this exponential reduction of $e^{\lambda_{F+} \frac{2\pi}{\Omega}}$ and $e^{\lambda_{F-} \frac{2\pi}{\Omega}}$ eventually pulls the eigenvalues below the point where floating point errors begin to appear. This manifests in Fig.2.4 where we begin to see visible errors for low $\frac{\Omega}{J}$ but large $\frac{\gamma}{J}$, compounding with the errors induced by our discretization process.

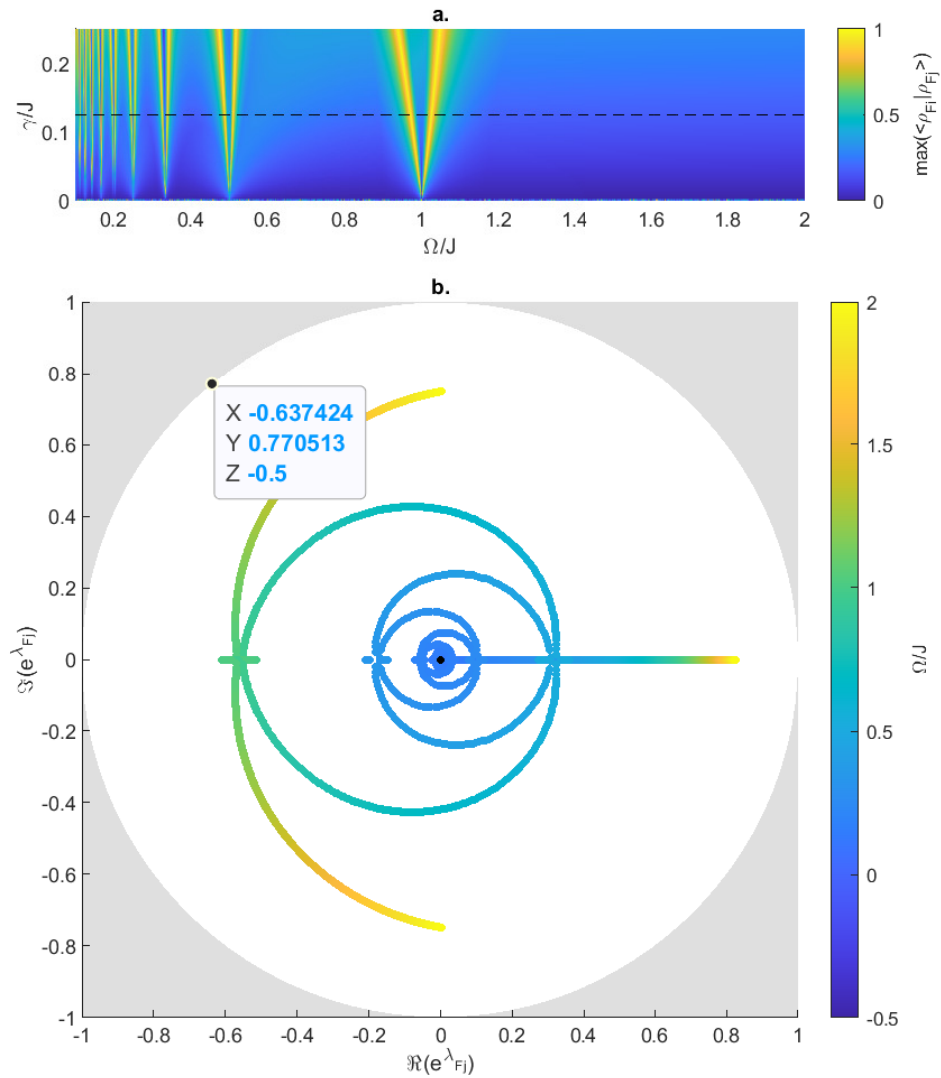


Figure 2.5. Evolution of Eigenvalues for V_F : Shows the evolution of the eigenvalues of \mathcal{V}_{F-} as $\frac{\Omega}{J}$ increases from $0.2 \rightarrow 2$. The center of the allowed complex disk is marked by the black dot. The path traced through the phase diagram in Figure 2.5a is marked by the dashed line, while the evolution along the path is denoted by the gradient line in Figure 2.5b.

Similarly one could take a path with constant $\frac{\Omega}{J}$ and linearly increasing $\frac{\gamma}{J}$ and see the same behavior as one passes over the large contour “bundle” near the point $(\frac{\Omega}{J}, \frac{\gamma}{J}) = (0, 4)$. In this case however, the cycle will repeat a finite number of times before diverging permanently.

Our second investigation will utilize the phase noise dissipator L_z . The instantaneous Lindbladian $\mathcal{L}_2(t)$ in the Operator Sum representation reads as

$$\mathcal{L}_2(t)[\rho] = -\imath J(t)[\sigma_x, \rho] + \gamma_z \mathcal{D}_z[\rho] \quad (2.56a)$$

$$\mathcal{D}_z[\rho] = \frac{1}{4}\sigma_z\rho\sigma_z - \frac{1}{4}\rho \quad (2.56b)$$

and the vectorized representation reads as

$$\mathcal{L}_2(t) = \frac{1}{2} \begin{bmatrix} 0 & -\imath J(t) & \imath J(t) & 0 \\ -\imath J(t) & -\gamma_z & 0 & \imath J(t) \\ \imath J(t) & 0 & -\gamma_z & -\imath J(t) \\ 0 & \imath J(t) & -\imath J(t) & 0 \end{bmatrix} \quad (2.57)$$

We use the same discretization method for calculating \mathcal{V}_F as before. As before, we also expect an eigen-density matching $\rho_{F0} = \rho_0$ to appear. We also can find that $\rho_{Fss} = \frac{1}{2}\mathbb{1}$ from Eq.2.41. Therefore, ρ_{F+} and ρ_{F-} are completely responsible for the non-orthogonality of the system.

Figure 2.6 shows the phase for periodic driving $J(t)$ and phase noise dissipation rate γ for $\delta = 1$. We see the same behavior of the exceptional points while the paths of the contours are slightly altered. The contours once again approach the static \mathcal{L}_2 exceptional point at $(\frac{\Omega}{J}, \frac{\gamma}{J}) = (0, 4)$ as a bundle, and we see the presence of the high frequency contour approaching $(\frac{\Omega}{J}, \frac{\gamma}{J}) = (\infty, 4 - 2\delta)$. We also see the exceptional contours form pairs approaching the resonance points $(\frac{\Omega}{J}, \frac{\gamma}{J}) = (\frac{2-\delta}{n}, 0)$.

In addition, we see that the phase diagram contains a new feature. We see deep blue paths stretching from the static exceptional point to the harmonic points through the overdamped regions. This indicates that at points within the overdamped region all of the eigen-densities have become orthogonal once again. These “maximally-orthogonal” contours present an

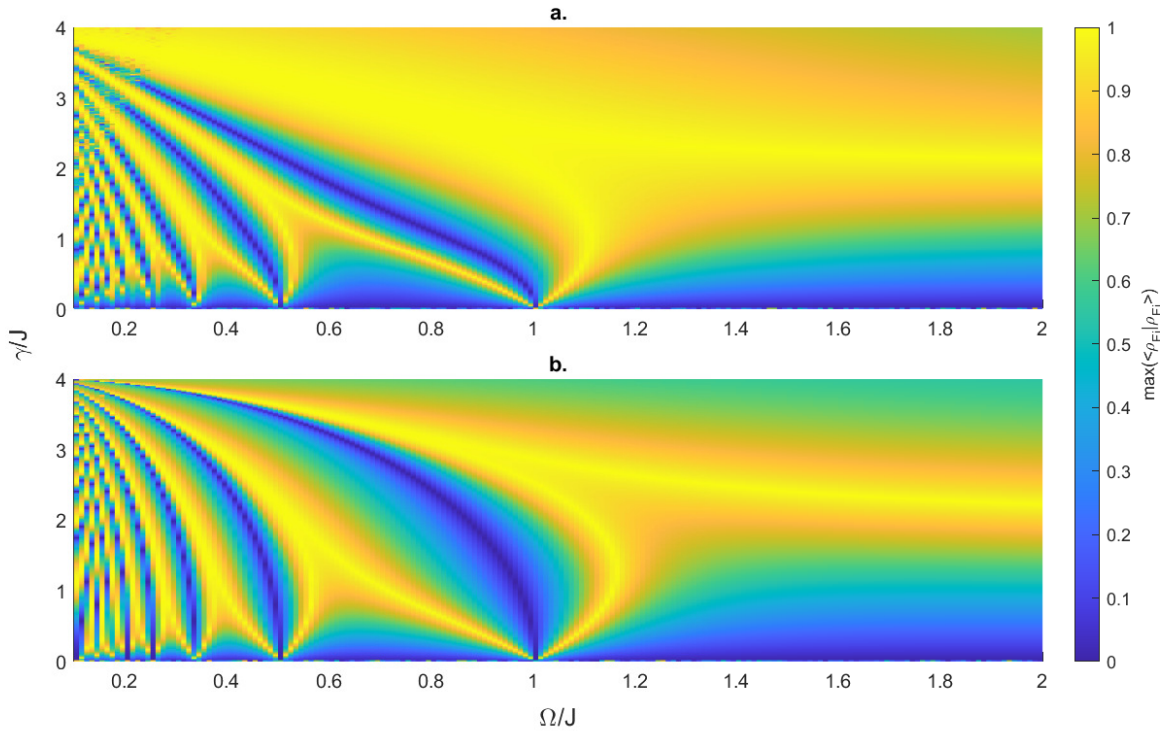


Figure 2.6. Periodic Driving with L_z Phase Diagram: Shows the maximum inner product of eigen-densities $\max(\langle \rho_{F_i} | \rho_{F_j} \rangle)$ for periodic driving $J(t)$ and phase noise rate γ with $\delta = 1$. Figure 2.6a shows the sinusoidal modulation, while Figure 2.6b shows the square wave modulation. Most of the properties of the phase diagram are the same as Figure 2.4, with identical limits on the exceptional point contours. The major difference lies in the degree of non-orthogonality in the overdamped regions. Here we see the system reach $\max(\langle \rho_{F_i} | \rho_{F_j} \rangle) = 0$ within the overdamped region, signifying that all ρ_{F_j} have become orthogonal. These “maximally-orthogonal” contours extend all the way up to the static exceptional point at $(\frac{\Omega}{J}, \frac{\gamma}{J}) = (0, 4)$.

opportunity for simplified quantum-process tomography under significant decay strength as each eigen-density is its own measurement operator.

2.4.2 Floquet Lindbladians with Periodic Dissipators

We now switch from periodic driving to periodic dissipation. We will use the same periodic functions as with the driving cases

$$\gamma(t) = \begin{cases} \gamma(1 - \delta \sin^2(\frac{\Omega}{2}t)) \\ \gamma(1 - \delta \text{Sq}(t - \frac{2\pi}{\Omega})) \end{cases} \quad (2.58)$$

Note that due to the complete positivity requirement that $\delta \in [0, 1]$ when considering the dissipators. The Floquet Lindbladian in the Operator Sum representation reads as

$$\mathcal{L}_2(t)[\rho] = -i\frac{J}{2}[\sigma_x, \rho] + \gamma_-(t)\mathcal{D}_-(t)[\rho] \quad (2.59a)$$

$$\mathcal{D}_-(t)[\rho] = \sigma_- \rho \sigma_+ - \frac{1}{4}(\sigma_z \rho + \rho \sigma_z) - \frac{1}{2}\rho \quad (2.59b)$$

and the vectorized representation reads as

$$\mathcal{L}_2(t) = \frac{1}{2} \begin{bmatrix} -2\gamma_-(t) & -iJ & iJ & 0 \\ -iJ & -\gamma_-(t) & 0 & iJ \\ iJ & 0 & -\gamma_-(t) & -iJ \\ 2\gamma_-(t) & iJ & -iJ & 0 \end{bmatrix} \quad (2.60)$$

Figure 2.7 shows the phase diagrams for periodic dissipation $\gamma_-(t)$ and $\gamma_z(t)$ under fixed coupling J for $\delta = 1$. Unlike in the case of periodic driving, here we see that the exceptional point contours do not converge to a single point. Instead, they form a set of splines that run from the unitary limit up toward $\frac{\gamma}{J} \rightarrow \infty$. We can still see the influence of the exceptional point of the static \mathcal{L}_2 in two ways. The first is that the high frequency limit contour approaches $(\frac{\Omega}{J}, \frac{\gamma}{J}) = (\infty, 8)$ due to an average $\gamma_-(t) \approx \gamma \frac{2-\delta}{2}$. The second is that each spline has narrow sections at low and high $\frac{\gamma}{J}$, while the spline widens in the middle (represented

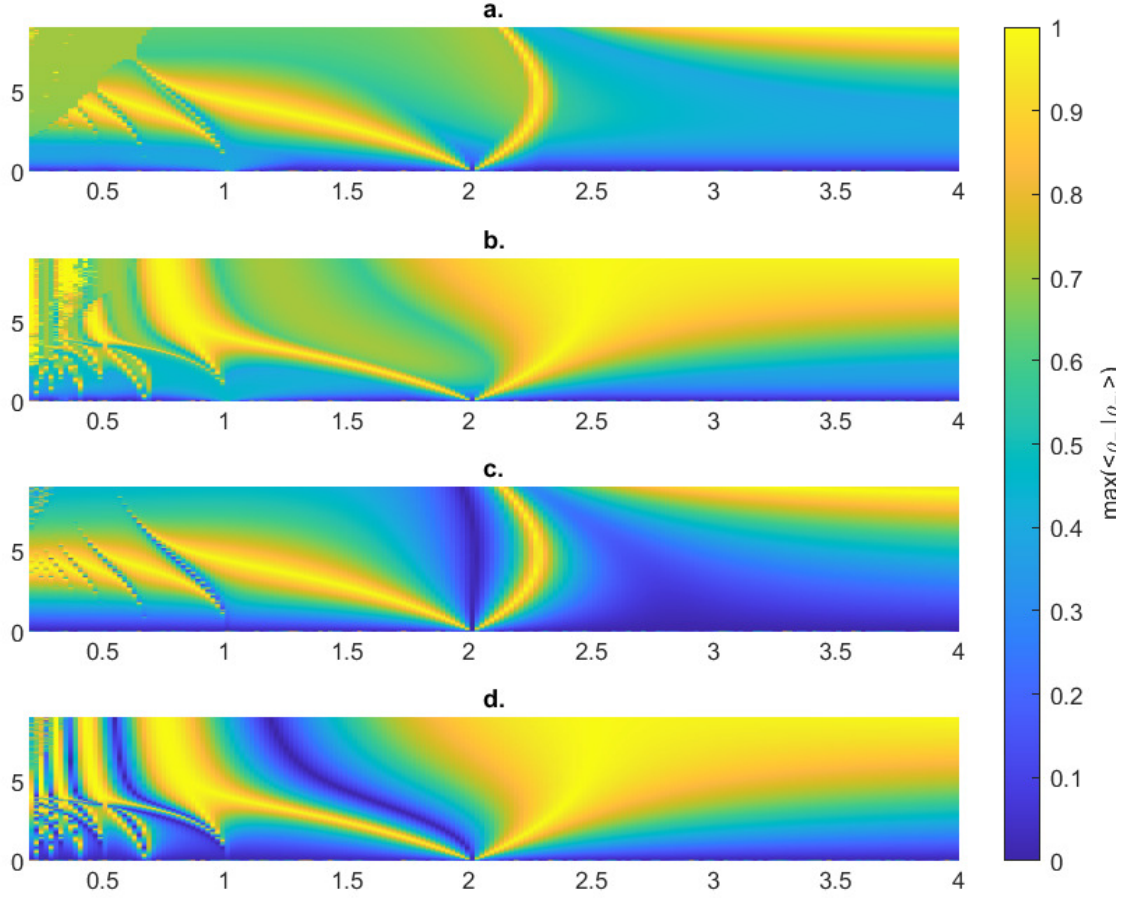


Figure 2.7. Periodic Dissipation Phase Diagrams: Shows the maximum inner product of eigen-densities $\max(\langle \rho_{Fi} | \rho_{Fj} \rangle)$ for periodic dissipations $\gamma_-(t)$ and $\gamma_z(t)$ with $\delta = 1$. Figure 2.6a shows the sinusoidal modulation with $L_-(t)$, while Figure 2.6b shows the square wave modulation with $L_-(t)$. Figure 2.6c shows the sinusoidal modulation with $L_z(t)$, while Figure 2.6d shows the square wave modulation with $L_z(t)$. Both the exceptional point contours as well as the maximally-orthogonal contours continue on toward $\frac{\gamma}{J}$. The exceptional contours no longer converge on the static exceptional point, instead the widest point of each curve traces a path toward $(\frac{\Omega}{J}, \frac{\gamma}{J}) = (0, 4)$. In Figure 2.7d we see the result of this continuation causes the contour sets to cross over each other, forming a grid of small underdamped and overdamped regions.

by a wider yellow section in 2.7). These wide sections converge on the point $\left(\frac{\Omega}{J}, \frac{\gamma}{J}\right) = (0, 4)$ in the low frequency limit. Figure 2.7cd we see once again the emergence of the maximally-orthogonal contours, though in the case of periodic dissipation they are capable of continuing toward $\frac{\gamma}{J} \rightarrow \infty$. We also see in the square wave modulation that the maximal-orthogonal contours converge on the static limit. To do this, the maximal-orthogonal contours must cross several sets of exceptional contours, leading to an interwoven grid of underdamped and overdamped regions. Because of this, the region near the static exceptional point can be used to cross from the underdamped to overdamped region with small parameter changes.

Figure 2.8 shows a magnified version of Figure 2.7d. Here we can see that the structure of the resonances with periodic dissipation is different than under periodic driving. Rather than all resonances reaching the unitary limit, they are split into two distinct categories. Resonances of the type $\left(\frac{\Omega}{J}, \frac{\gamma}{J}\right) = \left(\frac{2(2-\delta)}{2n+1}, 0\right)$, $\forall n \in \mathbb{Z}^+$ describe a true exceptional contour and reach the unitary limit. On the other hand, resonances of the type $\left(\frac{\Omega}{J}, \frac{\gamma}{J}\right) = \left(\frac{2-\delta}{n}, 0\right)$ never reach $\max(\langle \rho_{Fi} | \rho_{Fj} \rangle) = 1$ and so do not define a proper exceptional point contour. Because of this, they become increasingly orthogonal near the unitary limit and disappear into the underdamped region.

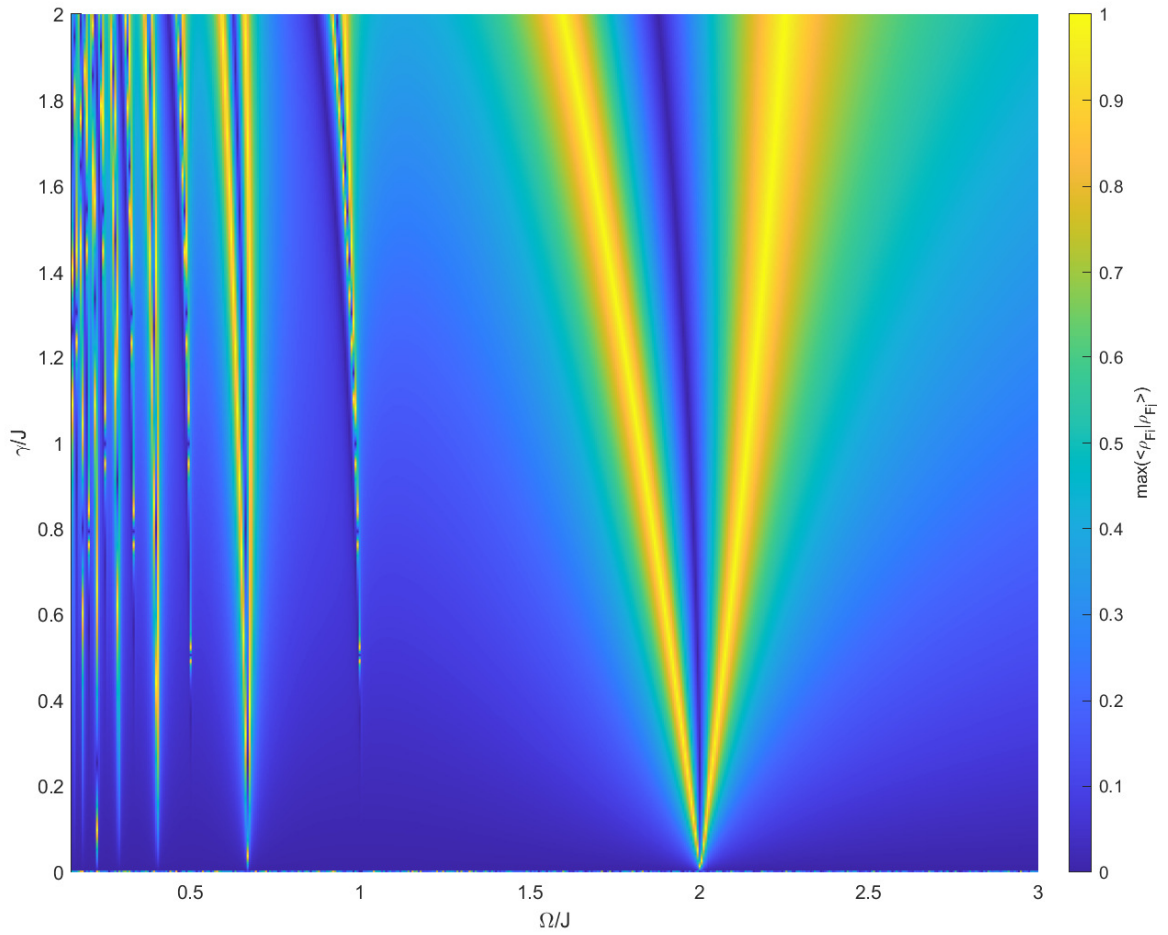


Figure 2.8. Resonances $L_z(t)$ Phase Diagram: Shows a close up of Figure 2.7d. We see that some of the exceptional point lines reach all the way to the unitary limit, while others fade into the underdamped region.

3. EXPERIMENTAL PLATFORM: CAVITY-COUPLED TRANSMON CIRCUITS

With Kraus maps providing an effective theory of quantum decoherence, we now seek a physical system governed by the Lindblad master equation through which we can study the models and measurement techniques we have covered. There are many such systems including evanescently coupled waveguides [5] and superconducting circuit arrays [32], [33]. In our case, the experimental platform that we are most familiar with consists of a superconducting transmon circuit placed within a large cavity [15]. The lowest energy levels of the transmon form an effective d_{tr} -level system, for which we will normally choose a qubit or qutrit construction. The circuit is then coupled to the ground level of the electromagnetic field within the cavity, resulting in a frequency shift dependent on the state of the qubit. In this chapter we will build up the physical framework for how these devices combine to produce a working quantum platform.

3.1 Quantization of the Transmon Circuit

A transmon is a type of superconducting circuit formed when a Josephson junction is shunted by a capacitor. Figure 3.1 shows the schematic for a simple transmon, where the capacitor C is marked by the parallel plates, and the Josephson junction L_j is marked by the boxed cross.

To find an effective Hamiltonian for the circuit, we will make use of some concepts from Electrodynamics. We define the voltage V along a circuit path to be the integral of the electric field \vec{E} along the path. We define the current I along a circuit path to be the integral of the magnetic field \vec{B} encoupassing the path in a plane perpendicular to a point

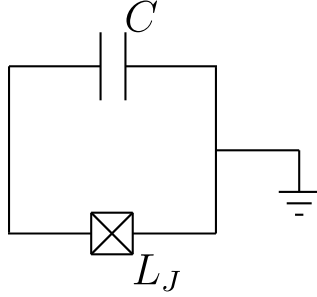


Figure 3.1. Transmon Schematic: Circuit diagram for a transmon, consisting of a Josephson junction L_J that has been shunted by a capacitor C .

along the path. We can further define the accumulation of V (I) with time as the circuit's branch flux Φ (charge Q) respectively.

$$V(t) = \int_a^b \vec{E} \cdot d\vec{r} \quad (3.1a)$$

$$I(t) = \oint_{\vec{l}} \vec{B} \cdot d\vec{l} \quad (3.1b)$$

$$\Phi(t) = \int_{-\infty}^t dt' V(t') \quad (3.1c)$$

$$Q(t) = \int_{-\infty}^t dt' I(t') \quad (3.1d)$$

where \vec{r} is the parametric path of the circuit and \vec{l} is a closed path in a plane perpendicular to \vec{r} .

3.1.1 Capacitors

Looking at the components of the transmon, the capacitor is constructed from two parallel plates separated in space by either a vacuum or a dielectric material. The defining

characteristic of the capacitor is the relation between the voltage difference across the plates to the charge stored on the plates

$$\partial_t \Phi(t) = V_C(t) = \frac{1}{C} Q_C(t) = \frac{1}{C} \int_{-\infty}^t dt' I(t') \quad (3.2)$$

This linear function allows us to express the “kinetic” energy stored in the capacitor as a function of $\partial_t \Phi(t)$

$$K_C(t) = \int_{-\infty}^t dt' V_C(t') I(t') = \frac{1}{2} C (\partial_t \Phi(t))^2 \quad (3.3)$$

3.1.2 Josephson Junctions

Somewhat similar in construction to the capacitor, the Josephson junction itself is formed from two superconducting leads bridged by a thin insulator ($\sim 1\text{nm}$). Pairs of electrons in the superconducting material are bound into superposition states known as Cooper pairs, which cause the electron pair to behave as a boson. These pairs are then capable of tunneling across the insulator to the opposite superconducting lead, producing a current when they do so but experiencing a change in phase $\phi(t)$

$$V_J(t) = \frac{1}{2e} \partial_t \phi(t) \quad (3.4a)$$

$$I_J(t) = I_{cr} \sin(\phi(t)) \quad (3.4b)$$

where $2e$ is the charge per Cooper pair, and I_{cr} is the critical current of the superconductor. Eq.3.4a allows us to relate $\phi(t)$ to the branch flux $\Phi(t) = \frac{1}{2e} \phi(t)$. Substituting this into Eq.3.4b yields

$$I_J(t) = I_{cr} \sin\left(2\pi \frac{\Phi(t)}{\Phi_0}\right) \quad (3.4c)$$

where $\Phi_0 = \frac{1}{2e}$ is the magnetic flux quantum. As the current is a function of $\Phi(t)$, we find that the Josephson junction behaves like a non-linear inductor (the first order correction is precisely a linear inductor), and we can derive an effective inductance

$$L(t) = \frac{d\Phi}{dI} = \frac{\Phi_0}{2\pi I_{cr}} \sec\left(2\pi \frac{\Phi}{\Phi_0}\right) \quad (3.5a)$$

$$\partial_t \Phi(t) = V_J(t) = L \partial_t I(t) = L \partial_t^2 Q_J(t) \quad (3.5b)$$

which allows us to express the “potential” energy stored in the Josephson junction

$$\begin{aligned} P_J(t) &= \int_{-\infty}^t dt' V_J(t') I(t') = \frac{\Phi_0 I_{cr}}{2\pi} \left(1 - \cos\left(2\pi \frac{\Phi(t)}{\Phi_0}\right)\right) \\ &= \frac{\pi I_{cr} \Phi(t)^2}{\Phi_0} - \frac{\pi^3 I_{cr} \Phi(t)^4}{3\Phi_0^3} + O(\Phi^6) \end{aligned} \quad (3.6)$$

Before moving forward we will note that there is an opportunity during circuit construction to make the Josephson junction tunable. A Superconducting QUantum Interference Device (SQUID) is constructed from a Josephson junction that has been split along the circuit path and separated, resulting in two Josephson junctions in parallel. The area between the junction paths becomes a loop that is highly susceptible to external magnetic fluxes $\Phi_{ex}(t)$. This external flux modifies P_J as

$$P_J(t) = \frac{\Phi_0 I_{cr}}{\pi} \cos\left(\pi \frac{\Phi_{ex}(t)}{\Phi_0}\right) \left(1 - \cos\left(2\pi \frac{\Phi(t)}{\Phi_0}\right)\right) \quad (3.7)$$

We can then collect the terms $2I_{cr} \cos\left(\pi \frac{\Phi_{ex}(t)}{\Phi_0}\right) = I_{SQUID}(t)$ to effectively create a single Josephson junction with an externally adjustable critical current.

3.1.3 Deriving the Transmon Hamiltonian

Thus the Lagrangian for Fig.3.1 is

$$L_{tr} = K_C - P_J = \frac{1}{2} C (\partial_t \Phi)^2 - \frac{\Phi_0 I_{cr}}{2\pi} \left(1 - \cos\left(2\pi \frac{\Phi}{\Phi_0}\right)\right) \quad (3.8)$$

At this point we need to make a couple observations. First, L has a natural coordinate of Φ whose conjugate momentum is $p = \frac{dL}{d(\partial_t \Phi)} = Q$. Second, it will be simpler to work in a unitless basis. Therefore we exchange the charge for the number of Cooper pairs $Q = -2em$, and we exchange the branch flux for the superconducting phase $\Phi(t) = \frac{1}{2e}\phi(t)$. Finally, we will collect the coefficients of the function by defining the charging energy of the capacitor $E_C = \frac{e^2}{2C}$, as well as the Josephson energy $E_J = \frac{I_{cr}}{2e}$. This leaves us with the (classical) Hamiltonian

$$H_{tr} = m\partial_t\phi - L = 4E_C m^2 + E_J(1 - \cos\phi) \quad (3.9)$$

From this point we quantize the Hamiltonian by exchanging the continuous variables m and ϕ for operator equivalents which obey the commutation relation

$$[\Phi, Q] = \iota \quad (3.10)$$

$$[\phi, -m] = \iota \quad (3.11)$$

We choose a basis for the operators in which ϕ is diagonal, as this will make working with the non-linear term simpler. For this reason, we rewrite $m = -\iota\partial_\phi$.

Finally, we are left with the (quantized) Hamiltonian

$$H_{tr} = -4E_C\partial_\phi^2 + E_J(1 - \cos\phi) \quad (3.12a)$$

$$= -4E_C\partial_\phi^2 + \frac{E_J\phi^2}{2} + O(\phi^4) \quad (3.12b)$$

$$= -4E_C\partial_\phi^2 + \frac{E_J\phi^2}{2} - \frac{E_J\phi^4}{4!} + O(\phi^6) \quad (3.12c)$$

Figure 3.2 plots Eq.3.12, which gives three approximations for the potential energy of H . Eq.3.12a gives the proper expression for the Hamiltonian, however there are infinitely many orders of corrections to H and we are only interested in utilizing the lowest levels of the transmon for our qubit / qutrit. Therefore we consider the limit $E_J \gg E_C$, under which we expand the $\cos\phi$ potential and keep the lowest order correction.

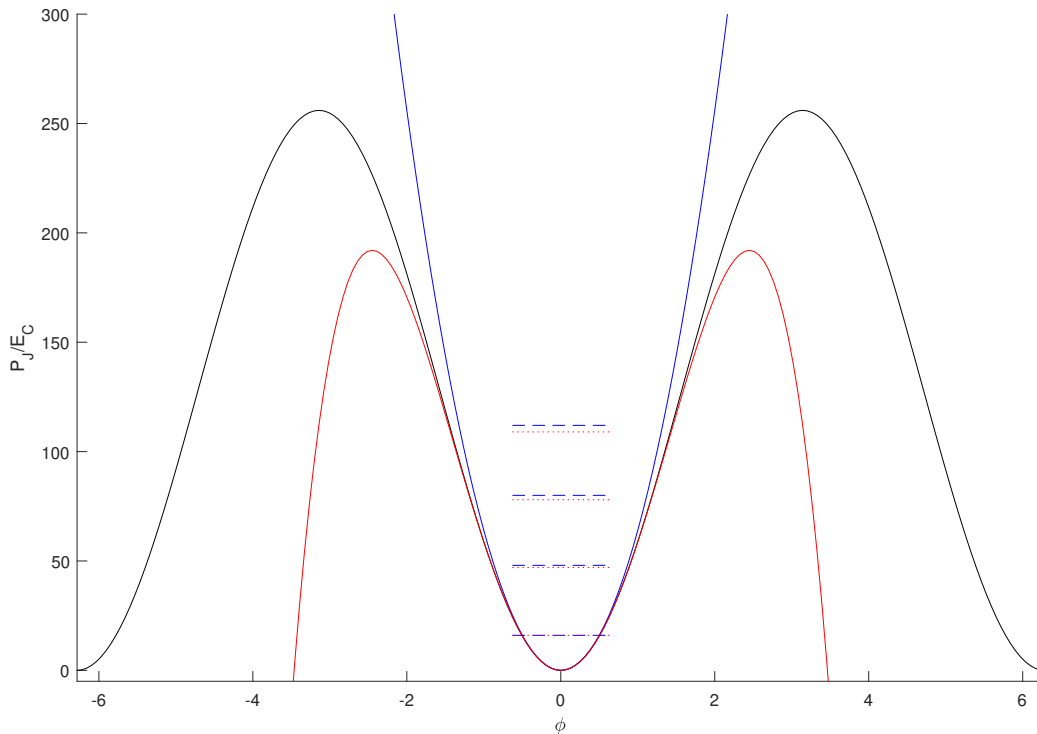


Figure 3.2. Transmon Potential Approximations: Shows the various potential approximations in Eq.3.12 when $\frac{E_J}{8E_C} = 16$. The proper potential Eq.3.12a is shown in black. The harmonic potential Eq.3.12b is shown in blue. The anharmonic potential Eq.3.12c is shown in red. In addition, the first four energy levels are plotted for the harmonic and anharmonic oscillators, with blue dashes for the harmonic oscillator, and red dots for the anharmonic oscillator. We see that the energy levels of the harmonic oscillator are evenly spaced, while the energy levels of the anharmonic oscillator are unevenly distributed. This unevenness allows us to drive specific pairs of levels when coupled to the cavity.

The result is Eq.3.12b, which has the form of a quantum harmonic oscillator (this is the result that we would have obtained by using a linear inductor instead of a Josephson junction). This suggests that we fully quantize H by defining creation (annihilation) operators b^\dagger (b) with commutation relation $[b, b^\dagger] = 1$

$$b = \frac{1}{\sqrt{2}} \left(\sqrt[4]{\frac{E_J}{8E_C}} \phi - i \sqrt[4]{\frac{8E_C}{E_J}} m \right) \quad (3.13a)$$

$$b^\dagger = \frac{1}{\sqrt{2}} \left(\sqrt[4]{\frac{E_J}{8E_C}} \phi + i \sqrt[4]{\frac{8E_C}{E_J}} m \right) \quad (3.13b)$$

$$\phi = \sqrt[4]{\frac{2E_C}{E_J}} (b + b^\dagger) \quad (3.13c)$$

$$m = \sqrt[4]{\frac{E_J}{32E_C}} (b - b^\dagger) \quad (3.13d)$$

These operators allow us to express H as

$$H_{tr} \approx \sqrt{8E_C E_J} \left(b^\dagger b + \frac{1}{2} \right) \quad (3.14)$$

with an associated eigenbasis $|n_b\rangle$ where $n \in \mathbb{Z}^{0+}$. The solutions of this Hamiltonian provide a good approximation for the lowest energy levels of the transmon, but come with a physical consequence. Since we have approximated Eq.3.12b to a quantum harmonic oscillator, we have been left with energy levels that have even spacing. We know phenomenologically that the energy levels of the transmon will not be evenly spaced, and this is an important physical property as it allows us to address specific energy gaps in the transmon.

To remedy this, we include the next highest correction order in Eq.3.12c. We can still make use of b and b^\dagger to express Eq.3.12c as

$$H_{tr} \approx \sqrt{8E_C E_J} \left(b^\dagger b + \frac{1}{2} \right) - \frac{\alpha}{12} (b + b^\dagger)^4 \quad (3.15)$$

We refer to $\alpha = E_C$ as the anharmonicity produced by the fourth order correction term. This term can be expanded in normal ordering to produce a long list of potentials, many of which will not conserve the number of excitations in a state. For this reason we will leave

expanding the anharmonicity until later on when we transform into the rotating frame, as we can effectively remove these non-conserving potentials.

3.2 Quantization of the Cavity

Consider a cavity inside of a conductor in the shape of an elongated cylinder $r \ll h$. Due to the geometry of the cavity we can approximate electromagnetic waves inside the cavity as traveling along the rotational axis of the cylinder, while the polarization of the electric and magnetic fields are along the xy -plane. We align the rotational axis of the cylinder to the z -axis, and set the polarization of the electric field \vec{E} inside the cavity to the x -axis.

3.2.1 Maxwell's Equations

Now consider the four Maxwell's equations which describe the electric and magnetic fields within the cavity

$$\vec{\nabla} \cdot \vec{E} = \frac{\rho}{\epsilon_0} \quad (3.16a)$$

$$\vec{\nabla} \cdot \vec{B} = 0 \quad (3.16b)$$

$$\vec{\nabla} \times \vec{E} = -\partial_t \vec{B} \quad (3.16c)$$

$$\vec{\nabla} \times \vec{B} = \mu_0 \vec{J} + \epsilon_0 \mu_0 \partial_t \vec{E} \quad (3.16d)$$

where $\vec{\nabla}$ is the spacial gradient, ρ is the distribution of charge sources, \vec{J} is the distribution of currents, and ϵ_0 (μ_0) is the vacuum permittivity (permeability). The cavity will not have external currents or charge sources present, so these terms are eliminated. This, combined with our choice of polarization, yield the following second order differential equations

$$\partial_z^2 E_x(z, t) = \frac{1}{c^2} \partial_t^2 E_x(z, t) \quad (3.17a)$$

$$\partial_z^2 B_y(z, t) = \frac{1}{c^2} \partial_t^2 B_y(z, t) \quad (3.17b)$$

where $c = \frac{1}{\sqrt{\epsilon_0\mu_0}}$ is the speed of light. The solutions to these equations are plane waves

$$E_x(k, z, t) = Ae^{ik(z-ct)} \quad (3.18a)$$

$$B_y(k, z, t) = \frac{A}{c}e^{ik(z-ct)} \quad (3.18b)$$

where A is an arbitrary normalization factor. However, the presence of the conductive walls of the cavity forces the electric field at the walls to 0. This requires that the solutions form standing waves (modes) within the cavity

$$E_x(k, z, t) = A \sin(kz) \sin(kct) \quad (3.19a)$$

$$B_y(k, z, t) = \frac{A}{c} \cos(kz) \cos(kct) \quad (3.19b)$$

where $k = \frac{\pi n_k}{L}$, $n_k \in \mathbb{Z}^+$, and L is the height of the cavity.

3.2.2 Deriving the Cavity Hamiltonian

Finally, we can calculate the energy of the cavity per mode through

$$H_k = \int_V dV \frac{\epsilon_0}{2} |E_x(k, z, t)|^2 + \frac{1}{2\mu_0} |B_y(k, z, t)|^2 = \frac{\epsilon_0 V A^2}{2} \quad (3.20)$$

We can now move to quantize the electromagnetic field in the cavity. The trick will be to note that we can express

$$E_x(k, z, t) = A \sin(kz) f(t) \quad (3.21a)$$

$$B_y(k, z, t) = \frac{A}{kc^2} \cos(kz) \partial_t f(t) \quad (3.21b)$$

by obfuscating the temporal components of $E_x(k, z, t)$ and $B_y(k, z, t)$. This results in the energy appearing as a simple harmonic oscillator with coordinate $f(t)$ after integration

$$H_k = \frac{\epsilon_0 V}{2} A^2 \left(\frac{1}{2} f(t)^2 + \frac{1}{2(kc)^2} (\partial_t f(t))^2 \right) \quad (3.22)$$

$$= \frac{(kc)^2}{2} f(t)^2 + \frac{1}{2} g(t)^2 \quad (3.23)$$

where we have set $A = \sqrt{\frac{2(kc)^2}{\epsilon_0 V}}$, and $g(t) = \partial_t f(t)$ is the canonical momentum for our “temporal function” coordinate. We then express H_k in creation (annihilation) operators a_k^\dagger (a_k) with commutation relation $[a_k, a_l^\dagger] = \delta_{kl}$

$$a_k = \frac{1}{\sqrt{2}} \left(\sqrt{kc} f(t) + i \frac{1}{\sqrt{kc}} g(t) \right) \quad (3.24a)$$

$$a_k^\dagger = \frac{1}{\sqrt{2}} \left(\sqrt{kc} f(t) - i \frac{1}{\sqrt{kc}} g(t) \right) \quad (3.24b)$$

$$E_x(k, z, t) = \sqrt{\frac{kc}{\epsilon_0 V}} \sin(kz) (a_k + a_k^\dagger) \quad (3.24c)$$

$$B_y(k, z, t) = -i \sqrt{\frac{k}{c\epsilon_0 V}} \cos(kz) (a_k - a_k^\dagger) \quad (3.24d)$$

This makes the diagonalized H_k

$$H_k = kc \left(a_k^\dagger a_k + \frac{1}{2} \right) \quad (3.25)$$

with the Fock states $|n_a, k\rangle$, $n \in \mathbb{Z}^{0+}$ as a basis for each mode of the electromagnetic field.

3.3 Cavity-Circuit Interaction

The next piece we need is to determine how the transmon and the cavity interact. We place the transmon circuit at the center of the cavity, and seek to couple two levels of the transmon with the lowest mode of the cavity $k_1 = \frac{\pi}{L}$. The two-level submanifold of the transmon we wish to couple to the cavity has an associated dipole moment, which we can

describe in terms of the Pauli matrices of the submanifold. This dipole then couples to the electric field of the cavity, giving us the interaction potential

$$H_{int} = -\vec{d} \cdot \vec{E}(k, \frac{L}{2}, t) = -J (b + b^\dagger) (a_k + a_k^\dagger) \quad (3.26)$$

where $J = d_x \sqrt{\frac{kc}{\epsilon_0 V}}$. Note that the strength of the coupling is normally chosen $J \ll \sqrt{8E_C E_J}$ (if the transmon energy spacing is GHz range, then the coupling will be MHz range). Then, the full Hamiltonian for the cavity coupled transmon circuit is

$$\begin{aligned} H &= H_{tr} + H_k + H_{int} \\ &= \sqrt{8E_C E_J} \left(b^\dagger b + \frac{1}{2} \right) - \frac{\alpha}{12} (b + b^\dagger)^4 + kc \left(a_k^\dagger a_k + \frac{1}{2} \right) - J (b + b^\dagger) (a_k + a_k^\dagger) \end{aligned} \quad (3.27)$$

3.3.1 Rotating Wave Approximation

To significantly reduce the complexity of H , we now take a rotating wave approximation of the system. We start by transforming H to the interaction picture H_I

$$H_I = U^\dagger H U + i(\partial_t U^\dagger) U \quad (3.28a)$$

$$U = e^{-itH_0} \quad (3.28b)$$

$$H_0 = kca_k^\dagger a_k + \sqrt{8E_C E_J} b^\dagger b \quad (3.28c)$$

where H_0 is the frame of reference that rotates between the transmon and the cavity. Note the transformation properties of the creation and annihilation operators in the rotating frame

$$U^\dagger b U = e^{-i\sqrt{8E_C E_J} t} b \quad (3.29a)$$

$$U^\dagger b^\dagger U = e^{i\sqrt{8E_C E_J} t} b^\dagger \quad (3.29b)$$

$$U^\dagger a U = e^{-ikct} a \quad (3.29c)$$

$$U^\dagger a^\dagger U = e^{ikct} a^\dagger \quad (3.29d)$$

From these, we observe that many of the normal ordered potentials in Eq.3.27 pick up a time-dependent phase with a large frequency. The “approximation” aspect of the rotating wave approximation will be to treat most of these “rapidly rotating” potentials as if they average out of the problem over the $\sim \mu s$ timescale that we are interested in observing. For this reason, we now reduce H_I to H_{RWA} by removing any potentials which

- Operate only on the transmon, and do not conserve excitation number n_b .
- Operate only on the cavity, and do not conserve excitation number n_a .
- Operate on both the transmon and cavity, but which rotate with a frequency $|\sqrt{8E_C E_J} - kc| \gg J$.

Thus we arrive at the rotating wave Hamiltonian

$$H_{RWA} = \omega_{tr} \left(b^\dagger b + \frac{1}{2} \right) - \frac{\alpha}{2} b^\dagger b^\dagger b b + \omega_k \left(a_k^\dagger a_k + \frac{1}{2} \right) - J \left(e^{i\omega_J t} b^\dagger a_k + e^{-i\omega_J t} a_k^\dagger b \right) + \frac{\alpha}{2} \quad (3.30)$$

where $\omega_{tr} = \sqrt{8E_C E_J} - \alpha$, $\omega_k = kc$, and $\omega_J = \sqrt{8E_C E_J} - kc$. Our final step will be to truncate the levels of the transmon to the two or three lowest levels in order to form our qubit / qutrit. For the qubit, selecting the bottom two levels of the transmon and transforming to rotating with the cavity alone leaves us with

$$H_{2tr} = (\omega_{tr} - \omega_k) \sigma_z - J \sigma_x + \omega_k \left(a_k^\dagger a_k + \frac{1}{2} \right) = -2H_2 + H_k \quad (3.31)$$

3.4 Measuring Dissipation

The final consideration we are missing is how to implement the Lindblad dissipators so that the system will be governed by \mathcal{L} rather than H . Unlike in the previous sections where the source of the potentials were derivable from physical laws, the sources of decoherence are often somewhat random. The Lindblad dissipators that describe spontaneous emission and phase noise often arise stochastically on short timescales from a variety of sources. Some of these effects include impurities in the transmon circuit, imperfections in the cavity geometry, and collisions with particles remaining in the cavity after pumping. In most circumstances

the more practical approach is to characterize the dissipative effects on the experiment apparatus once it has been assembled. The components of the Hamiltonian component of \mathcal{L} can then be varied to explore the desired phenomena.

3.4.1 Spontaneous Emission

The simpler of the two dissipators to characterize is the spontaneous emission. For a cavity coupled transmon which is initialized with a combined excitation number $n = n_a + n_b$, Eq.3.30 predicts that n will be a conserved quantity. However, both the transmon circuit and the cavity have mechanisms through which the n can be irreversibly reduced. For this reason there is a natural tendency of the system to fall toward the state $|0_b 0_a k\rangle$.

In order to make a measurement of this effect, we first need to excite the transmon into an excited state $|j_b 0_a k\rangle$. We begin by sending an electromagnetic signal (usually a coherent state) through the cavity, representing an excitation of the cavity field to $|j_b 0_a k\rangle$ for each k present in the signal. For frequencies at which the cavity and transmon are on resonance this will drive the transmon between $|0_b j_a k\rangle$ and $|j_b 0_a k\rangle$. This effect will be observable in the transmittance spectrum of the cavity as a frequency shift of the peak transmittance. We can then characterize the time it takes to fully drive the transmon into $|j_b 0_a k\rangle$ as a π -shift of the transmon.

In order to measure the spontaneous emission rate, we perform a π -shift of the transmon, wait for a time t , then a measurement of the current transmon state. What we will observe is that there will be an exponential decay in the population of $|j_b 0_a k\rangle$ over time. Thus by finding the decay rate we can determine γ_- .

3.4.2 Phase Noise

In addition to determining the driving time for a π -shift of the transmon we can also determine a $\frac{\pi}{2}$ -shift of the transmon. Performing this rotation will place the transmon and cavity in a superposition $\frac{1}{\sqrt{2}}(|0_b j_a k\rangle + |j_b 0_a k\rangle)$. We can use this superposition state to determine γ_z through Ramsey interferometry.

First, we use a $\frac{\pi}{2}$ -shift to drive the system into the superposition state, which corresponds to a σ_x eigenstate. The phase noise dissipator will cause $\langle x \rangle$ to decay over time, however this is complicated by the fact that we are in a rotating frame $H_0 = -\frac{1}{2}\omega_{tr}\sigma_z$. Finally, we perform a $-\frac{\pi}{2}$ -shift to return the superposition state to $|j_b 0_a k\rangle$ and make a measurement. What we will observe is an underdamped oscillation of the population in $|j_b 0_a k\rangle$. We can then determine γ_z from the decay of the envelope of this oscillation.

4. CONNECTING NON-HERMITIAN PHYSICS TO QUANTUM MAPS

In the previous chapters we introduced two schemes for creating non-conservative dynamics in quantum systems. Non-Hermitian physics was developed in the language of states and operators, and acts as a working model of coherent gain and loss to a system. On the other hand open quantum maps were developed in the language of state densities, measurements, and super-operators, and are capable of describing the dynamics of decohering systems. In this chapter we will seek to connect the two theories, as well as develop experimental procedures through which non-Hermitian physics can be addressed through Lindbladian platforms.

4.1 Master Equations for Non-Hermitian Hamiltonians

With the Lindblad master equation defined, we are interested in extending the concepts of quantum maps to systems generated by non-Hermitian Hamiltonians. We immediately encounter a problem however, as the definition of the state density operator is no longer unambiguous with three possible definitions listed in Eq.4.1

$$\rho \stackrel{?}{=} \begin{cases} \sum_{ij} p_{ij} |\psi_i\rangle \langle\langle\psi_j| & \iff \text{Tr}(\rho) = \sum_j p_{jj} \langle\langle\psi_j|\psi_j\rangle \\ \sum_{ij} p_{ij} |\psi_i\rangle \langle\psi_j| & \iff \text{Tr}(\rho) = \sum_j p_{jj} \langle\psi_j|\psi_j\rangle \\ \sum_{ij} p_{ij} |\psi_i\rangle \langle\psi_j| & \iff \text{Tr}(\rho) = \sum_j p_{jj} \langle\psi_j|\psi_j\rangle_n \end{cases} \quad (4.1)$$

where we are working once again with a bi-orthogonal basis such that $(\langle\langle\psi_j|)^\dagger \neq |\psi_j\rangle$.

The first possibility is that all operators acting on a Hilbert space (state density operator included) are decomposed into the right-eigenstates and left-eigenstates of H . This definition for ρ maintains the form of the quantum von-Liouville equation $\partial_t \rho = [H, \rho]$, but has solutions $\rho(t) = U\rho(0)U^{-1}$ as $\langle\langle\psi_j|$ evolve under U^{-1} rather than U^\dagger . Such a definition leverages the property that $|\psi_j\rangle$ and $\langle\langle\psi_j|$ form a bi-orthogonal basis to make mathematical operations easier to perform. However this results in the loss of hermiticity for ρ , and so information

on the imbalances between state coherences would be required to fully describe ρ in an experiment.

The second possibility is that ρ is constructed from right-eigenstates, while utilizing the Dirac inner product. This definition for ρ maintains the form of the solutions to the quantum von-Liouville equation $\rho(t) = U\rho(0)U^\dagger$, but must be generated by an altered master equation $\partial_t\rho = H\rho - \rho H^\dagger$. This convention is experimentally relevant as the hermiticity of ρ is maintained and there is no need for additional information on the coherence terms. However, ρ will not be trace preserving as $\mathbb{1}$ is not a constant of motion, and thus the statistical interpretation of ρ is broken.

The final possibility is that ρ is constructed from right-eigenstates, but that the inner products of states are taken with respect to a metric specified by H . This convention is commonly used in pseudo-Hermitian studies of non-Hermitian systems, and maintains the trace of $\rho(t)$ as the system evolves under H . Similar to H it is possible to maintain the “effective” hermiticity of ρ if η is positive definite, as there will exist a Dyson map from the seemingly non-Hermitian system to an equivalent Hermitian system. However, there only exists a positive definite η in the \mathcal{PT} -symmetric regime, and so the physical interpretation of p_{jj} as probabilities is lost when transitioning to the \mathcal{PT} -broken regime.

To settle on a definition for ρ we will make an analogy to the Lindbladian. In the derivation for \mathcal{L} we expanded K_0 to first order as $K_0 = \mathbb{1} + \delta t(-\imath H + C)$ where $H^\dagger = H$ was a Hermitian operator and $C^\dagger = -C$ was an anti-Hermitian operator. Cast in the conventions of non-Hermitian Hamiltonians, this expansion is equivalent to

$$K_0 = \mathbb{1} + \delta t(-\imath H_h + \Gamma) = \mathbb{1} + -\imath H \delta t \tag{4.2}$$

Proceeding further with the derivation of \mathcal{L} , but grouping the anti-commuting term (3) with the commuting term (1) rather than the Kraus operator like term (2) yields a new expression for \mathcal{L}

$$\mathcal{L}[\rho] = -\imath \underbrace{(H\rho - \rho H^\dagger)}_{(4)} + \sum_{\mu} \gamma_{\mu} \underbrace{L_{\mu}\rho L_{\mu}^\dagger}_{(2)} \quad (4.3)$$

$$H = H_h - \imath \sum_{\mu} \frac{\gamma_{\mu}}{2} L_{\mu}^\dagger L_{\mu} \quad (4.4)$$

where we can see that term (4) is identical to the generating master equation for the second possible definition of ρ . Furthermore, removing term (2) corresponds to reducing the number of Kraus operators in \mathcal{V} until $\rho(t) = K_0\rho(0)K_0^\dagger$ which will describe coherent but non-unitary evolution (though this will require that we disregard the trace preserving requirement or be forced to alter H).

Based on these similarities, we define the state density

$$\rho = \sum_{ij} p_{ij} |\psi_i\rangle \langle \psi_j| \quad (4.5)$$

$$\text{Tr}(\rho) = \sum_j p_{jj} \langle \psi_j | \psi_j \rangle \quad (4.6)$$

This results in a definition for the time evolution of ρ , which we can cast in the conventions of quantum maps

$$\rho(t) = \mathcal{U}[\rho(0)] = U\rho(0)U^\dagger \quad (4.7)$$

$$\partial_t \rho = \mathcal{H}[\rho] = -\imath (H\rho - \rho H^\dagger) \quad (4.8)$$

where \mathcal{U} is the quantum map of coherent evolution and \mathcal{H} is the non-Hermitian extension of the quantum von-Liouville equation, which we will refer to as the Liouvillian (\mathcal{H}) as opposed to the Hamiltonian (H) or Lindbladian (\mathcal{L}).

We will note that in many works concerning the Lindblad master equation, the term “Liouvillian” is used interchangeably with the term “Lindbladian” [7]. For our purposes

however, the two are distinct and the Liouvillian is the generator of coherent but non-unitary time evolution.

4.1.1 The Renormalized Master Equation

With our definition of ρ settled on, we now need to confront the statistical interpretation of non-Hermitian systems. Obviously since $\mathbb{1}$ is not a conserved quantity in these systems the coefficients p_{ij} are not the statistical weights for the states when making a measurement. However, this measurement-oriented statistical interpretation may give a hint at an answer.

Any measurement that we make of a system whose trace is not 1 will inevitably be normalized relative to the total number of measurements taken. For a static measurement operator Q , this amounts to normalizing the final state density $\tilde{\rho}(t) = \frac{1}{A}\mathcal{U}[\rho(0)]$ such that $\text{Tr}(\tilde{\rho}(t)) = 1$ where A is the normalization factor. One approach we could take then would be to set the normalization as the growth of the initial state over the evolution time, which would make the final state density

$$\tilde{\rho}(t) = \frac{\mathcal{U}[\rho(0)]}{\text{Tr}(\mathcal{U}[\rho(0)])} = \frac{\mathcal{U}|\rho(0)\rangle}{\langle\mathbb{1}|\mathcal{U}|\rho(0)\rangle} = \frac{\sum_{ij} p_{ij} U |\psi_i(0)\rangle \langle\psi_j(0)| U^\dagger}{\sum_j p_{jj} \langle\psi_j(0)| U^\dagger U |\psi_j(0)\rangle} \quad (4.9)$$

Taking this approach means that the coefficients p_{ij} are not the measurement probabilities, but are proportional to them. Therefore, as a particular p_{jj} grows relative to the rest of the system, the likelihood that state is measured grows with it. However, the other consequence of this approach is that $\tilde{\rho}$ must be governed by a non-linear master equation

$$\partial_t \tilde{\rho} = -\imath (H \tilde{\rho} - \tilde{\rho} H^\dagger) + \imath \text{Tr}((H - H^\dagger) \tilde{\rho}) \tilde{\rho} \quad (4.10a)$$

$$\imath \partial_t |\tilde{\psi}\rangle = (H - \langle H \rangle) |\tilde{\psi}\rangle \quad (4.10b)$$

$$-\imath \partial_t \langle \tilde{\psi} | = \langle \tilde{\psi} | (H^\dagger - \langle H^\dagger \rangle) \quad (4.10c)$$

and we expect to see non-linear complications such as accelerations under static H , and the development of sources and sinks on the surface of the Bloch sphere.

4.2 Pseudo-Hermiticity from Vectorization

The definition of the Liouvillian prompts us to investigate its properties from the perspective of quantum maps. We can define eigen-densities and eigen-measurements for \mathcal{H} just as we could with \mathcal{L}

$$\mathcal{H} |\rho_j\rangle = \lambda_j |\rho_j\rangle \quad (4.11a)$$

$$\langle\langle Q_j | \mathcal{H} = \lambda_j \langle\langle Q_j | \quad (4.11b)$$

However, now that the map is not trace preserving we will see several eigen-densities with non-zero trace.

We can further characterize the set of λ_j . The vectorized form of \mathcal{H} can be written as

$$\mathcal{H} = -\imath (\mathbb{1} \otimes H - H^* \otimes \mathbb{1}) \quad (4.12)$$

we know that the set of λ_j contains purely real or complex conjugate pairs if H is pseudo-Hermitian. From this we see that for pseudoHermitian systems we can classify λ_j into three broad categories based on the combinations

$$\lambda_k \rightarrow \lambda_{ij} = -\imath (\epsilon_i - \epsilon_j^*) \quad (4.13)$$

where the indices i and j count over d indices, and the index k counts over d^2 indices.

First, there is the set over identical indices $\lambda_{jj} = -\imath (\epsilon_j - \epsilon_j^*) = 2 \text{Im}(\epsilon_j)$. This set consists of purely real eigenvalues, as well as $\lambda_k = 0$ for all purely real ϵ_j . Second, there is the set over complex conjugate paired indices $\lambda_{jj^*} = -\imath (\epsilon_j - \epsilon_{j^*}) = 0$. This set only contains members if H is pseudo-Hermitian, but is empty otherwise. Finally, there is the set of unrelated indices $\lambda_{ij} = -\imath (\epsilon_i - \epsilon_j^*)$, $\forall i \neq j \neq j^*$. This set consists of complex valued λ_k , which may contain purely real, purely imaginary, or zero eigenvalues depending on the spectrum of H .

We note that if there are no degenerate eigenvalues in H , we expect d zero eigenvectors among the first and second sets, which mark an important group of λ_j . Consider the super-

operator \mathcal{H}^\dagger , which time evolves measurements in the Heisenberg picture. \mathcal{H}^\dagger in the operator sum representation is written

$$\mathcal{H}^\dagger[Q_j] = \lambda_j Q_j = \imath (H^\dagger Q_j - Q_j H) \quad (4.14)$$

for $\lambda_j = 0$ we are left with the right hand side of the equation, which becomes

$$Q_j H = H^\dagger Q_j \quad (4.15)$$

and so we have reproduced the intertwining relation Eq.1.18. Therefore we can quickly obtain a full set of intertwining operators η_j simply by diagonalizing \mathcal{H} .

This procedure also reveals that there are a set of operators related to η_j which experience an exponential decay rather than remain constant. For $\lambda_{jj} \neq 0$, we can displace a particular eigenvalue to zero by providing a complex shift $H' = H - \imath \lambda_{jj}$. Doing so will break the pseudo-hermiticity of the system into a loss (or gain) favored system, and yet there will be an operator that remains a constant of motion.

4.2.1 Intertwining Operators for Periodic Systems

We can use this definition of intertwining operators to quickly find the η_j for a Floquet Hamiltonian. We will consider the \mathcal{PT} -dimer with a time dependent gain and loss

$$H_2(t) = J\sigma_x + \imath\gamma(t)\sigma_z \quad (4.16)$$

This system is \mathcal{P} -pseudo-Hermitian regardless of the modulation we choose, and so we know that $\eta_0 = \sigma_x$. The system is also \mathcal{PT} -symmetric if $\int_0^T dt' \mathcal{H}(t') = 0$. The eigenvalues and eigenvectors for the instantaneous $H(t)$ are the same as those calculated in Chapter 1.3 once substituted with $\frac{J}{2} \rightarrow J$ and $\frac{\gamma}{2} \rightarrow \gamma(t)$. For each potential we calculate the Q_{F_j} by setting $\mathcal{U}_F = U_F^* \otimes U_F$ and solving for the left-eigenvectors.

The first case we consider will be square wave modulation with $\delta = 2$

$$\gamma(t) = \begin{cases} \gamma & t < \frac{T}{2} \\ -\gamma & t \geq \frac{T}{2} \end{cases} \quad (4.17)$$

for $t \in [0, T)$. We can explicitly evaluate U_F as

$$U_F = \mathcal{T}_o e^{\int_0^T dt' H(t')} = G_0 \mathbb{1} + iG_x \sigma_x + G_y \sigma_y \quad (4.18)$$

where $G_0 = [J^2 \cos(\epsilon T) - \gamma^2]/\epsilon^2$, $G_x = -J \sin(\epsilon T)/\epsilon$ and $G_y = -J\gamma[1 - \cos(\epsilon T)]/\epsilon^2$ are real for all ϵ_{\pm} . We will note that as $\epsilon \rightarrow 0$, the power series for U_F terminates as second order in T . For the static \mathcal{H}_2 , the maximum correction order we expect at the exceptional point is a first order correction as there are a maximum of two eigenvectors becoming degenerate. For the Floquet case, this shows that the order of the exceptional point, the correction order of the time evolution operator, and the rank of the Jordan block are not equivalent in time dependent dynamics.

The eigenvalues of U_F are

$$e^{-\imath\epsilon_{Fj}T} = G_0 \pm \imath\sqrt{G_x^2 - G_y^2} \quad (4.19)$$

From the eigen-measurements of \mathcal{U}_F we have the two intertwining operators $\eta_1 = \sigma_x$ and $\eta_2 = G_0 \mathbb{1} + G_y \sigma_z$, as well as the related Q_3 and Q_4 . Note that since Q_3 and Q_4 correspond to $\epsilon_{Fj} \neq 0$ that they cannot be Hermitianized, though they do have the relations $e^{-\imath\epsilon_{F3}T} = e^{-\imath\epsilon_{F4}T}$ and $Q_3 = Q_4^\dagger$.

Figure 4.1 compares the behavior of the intertwining operators of U_F during the time evolution as opposed to the predicted evolution $e^{-\imath\epsilon_{Fj}T}$. We see that at intermittent times the instantaneous $\langle Q_j \rangle(t)$ diverges from the predicted $e^{-\imath\epsilon_{Fj}T}$, but always converges on $e^{-\imath\epsilon_{Fj}T}$ at stroboscopic times $t = nT$. The one exception is η_1 which is a constant of motion for all instantaneous $H_2(t)$, and therefore is also a constant of motion for U_F .

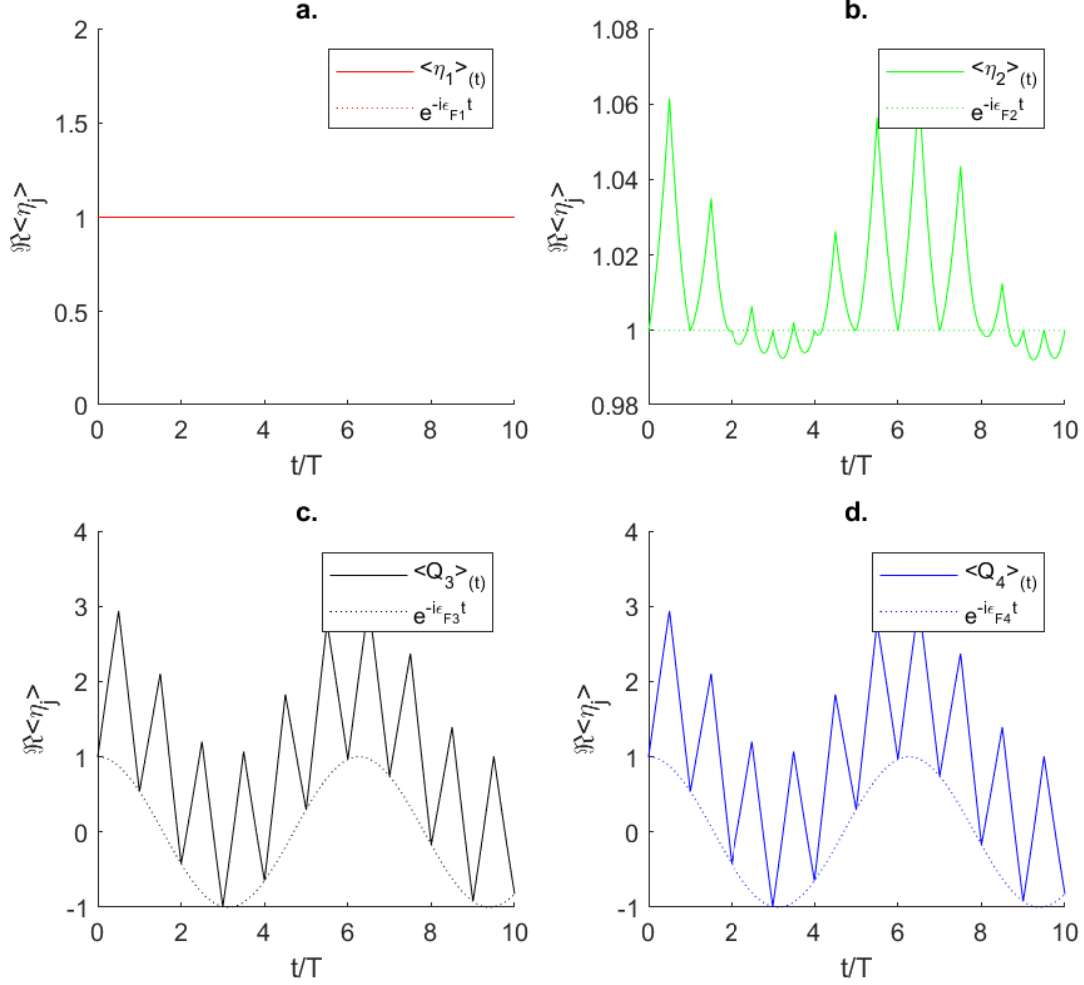


Figure 4.1. Intertwining Operators and Eigen-Measurements of Square Wave: Shows the expectation values $\langle Q_j \rangle$ for the four eigenmeasurements of $\mathcal{H}_2(t)$ under square wave modulation with $\frac{\gamma}{J} = 0.5$, $JT = 1$, and $\rho(0) = |\uparrow\rangle\langle\uparrow|$. Figure 4.1a shows η_1 , Figure 4.1b shows η_2 , Figure 4.1c shows Q_3 , and Figure 4.1d shows Q_4 . In each figure, the solid line shows the real-time value of $\langle Q_j \rangle$, while the dashed line shows the trend predicted by $e^{\lambda_{F_j} T}$. We see that at stroboscopic points the two trends converge in all four figures, while only η_1 is a constant of motion at all times.

The second case we consider will be a non-Hermitian “kicked” potential

$$\gamma(t) = \gamma\delta(t - T) - \gamma\delta(t - \frac{T}{2}) \quad (4.20)$$

for $t \in (0, T]$. We can explicitly evaluate U_F as

$$U_F = G_0\mathbb{1} + \imath G_x\sigma_x + G_y\sigma_y + G_z\sigma_z \quad (4.21)$$

$$G_0 = \cos^2(\frac{JT}{4}) - \sin^2(\frac{JT}{4}) \cosh(\gamma T) \quad (4.22)$$

$$G_x = -\sin(\frac{JT}{2}) \sinh^2(\frac{\gamma T}{2}) \quad (4.23)$$

$$G_y = \sin(\frac{JT}{2}) \sinh(\gamma T)/2 \quad (4.24)$$

$$G_z = -\sin^2(\frac{JT}{4}) \sinh(\gamma T) \quad (4.25)$$

The eigenvalues of U_F are

$$e^{-\imath\epsilon_{Fj}T} = G_0 \pm \imath\sqrt{G_x^2 - G_y^2 - G_z^2} \quad (4.26)$$

From the eigen-measurements of U_F we have the two intertwining operators $\eta_1 = \sigma_x$ and $\eta_2 = G_x\mathbb{1} - G_z\sigma_y + G_y\sigma_z$, as well as the related Q_3 and Q_4 . As in the first potential, Q_3 and Q_4 cannot be Hermitianized but have the relations $e^{-\imath\epsilon_{F3}T} = e^{-\imath\epsilon_{F4}T}$ and $Q_3 = Q_4^\dagger$.

Figure 4.2 compares the behavior of the intertwining operators of U_F during the time evolution as opposed to the predicted evolution $e^{-\imath\epsilon_{Fj}T}$. We see that at intermittent times the instantaneous $\langle Q_j \rangle(t)$ diverges from the predicted $e^{-\imath\epsilon_{Fj}T}$, but always converges on $e^{-\imath\epsilon_{Fj}T}$ at stroboscopic times $t = nT$. The one exception is η_1 which is a constant of motion for all instantaneous $H_2(t)$, and therefore is also a constant of motion for U_F .

4.3 Postselection of the Lindbladian

The next issue we need to address is how to go about removing the jump operators from \mathcal{L} . Physically the jump operators produce instantaneous changes in ρ , but these events occur sporadically during the evolution of ρ at a rate controlled by γ_μ . We also cannot continuously

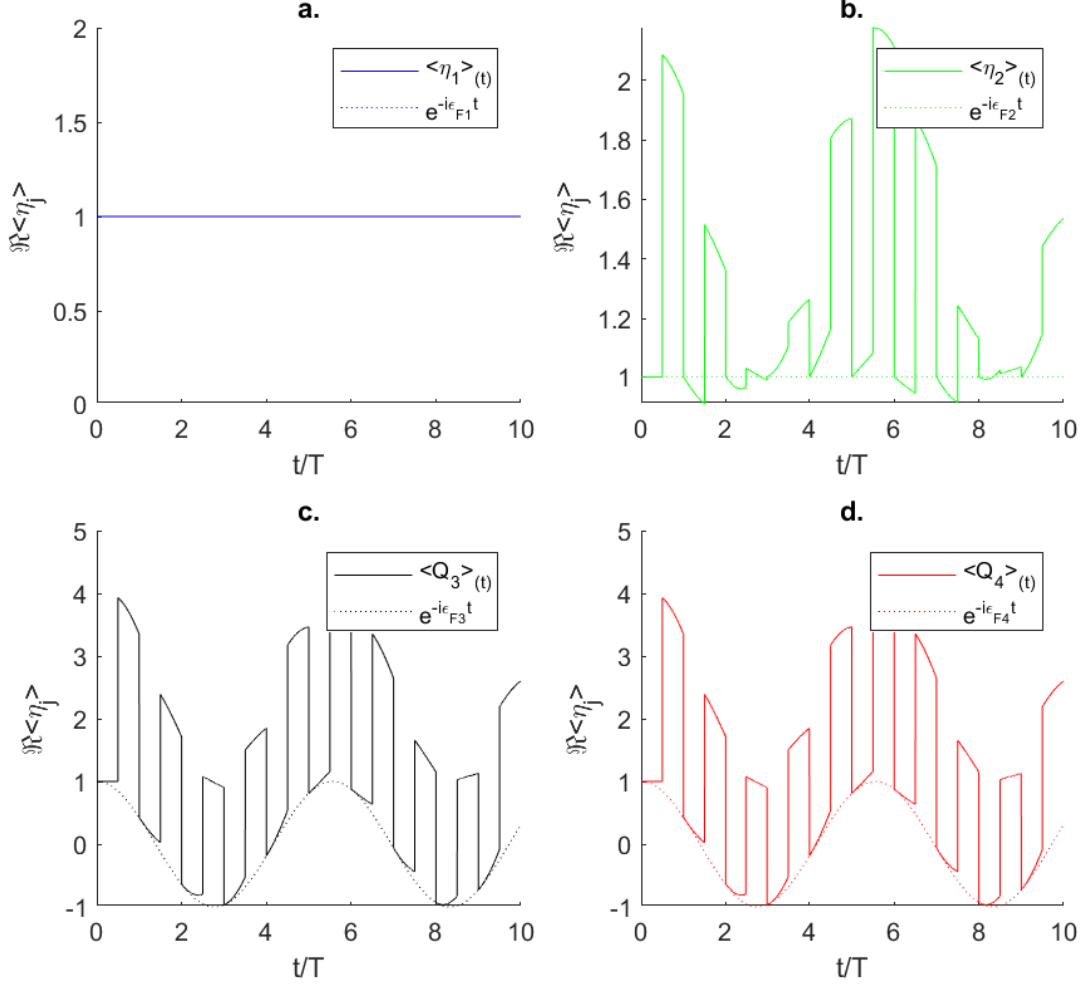


Figure 4.2. Intertwining Operators and Eigen-Measurements of Kicked Potential: Shows the expectation values $\langle Q_j \rangle$ for the four eigenmeasurements of $\mathcal{H}_2(t)$ under non-Hermitian δ potential kicks with $\frac{\gamma}{J} = 0.5$, $JT = 1$, and $\rho(0) = |\uparrow\rangle\langle\uparrow|$. Figure 4.2a shows η_1 , Figure 4.2b shows η_2 , Figure 4.2c shows Q_3 , and Figure 4.2d shows Q_4 . In each figure, the solid line shows the real-time value of $\langle Q_j \rangle$, while the dashed line shows the trend predicted by $e^{\lambda_{F_j}T}$. We see that at stroboscopic points the two trends converge in all four figures, while only η_1 is a constant of motion at all times.

measure the system to try and detect the jumps, as such a strong measurement would result in a back action on the system. What we require then is a herald of the jump event that is long lived or detectable without interfering with the system.

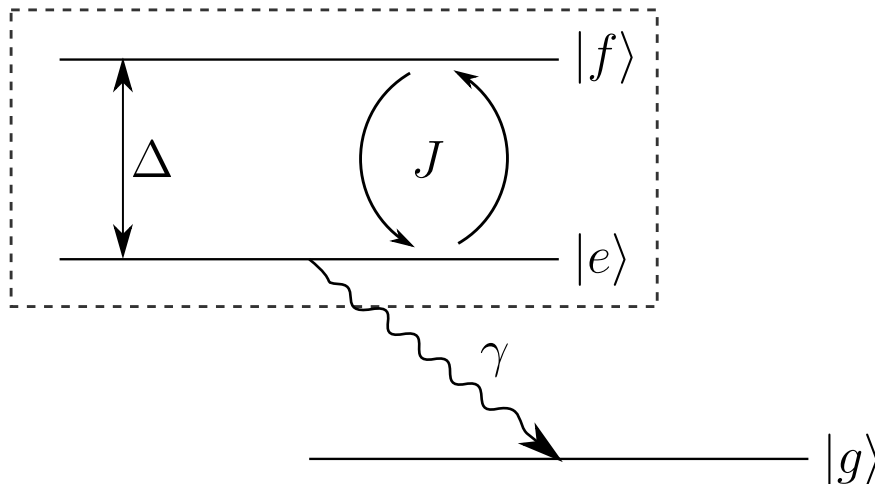


Figure 4.3. Transmon Qutrit Postselection Scheme: Illustration depicting a ideal transmon qutrit. The system consists of three energy levels with unequal spacing, allowing the excited states $|f\rangle$ and $|e\rangle$ to be driven independent of the ground state $|g\rangle$. The ideal system has only one Lindblad dissipator of the form $L_{ge} = |g\rangle \langle e|$, allowing the detection of quantum jumps simply by non-zero measurement of $|g\rangle$.

One way that we can accomplish this is by implementing a postselection process using an ancillary state, similar to what we saw in Figure 1.1b. By increasing the anharmonicity we can select the lowest three levels of the transmon circuit. We then select the two excited

states $|f\rangle$ and $|e\rangle$ with detuning Δ to be driven by the coupling J . The isolation of the two level manifold is then broken by a single Lindblad dissipator of the form

$$L_{ge} = |g\rangle \langle e| \quad (4.27a)$$

$$L_{ge}^\dagger L_{ge} = |e\rangle \langle e| \quad (4.27b)$$

which results in term (2) in \mathcal{L} being isolated within the two level manifold, while any jump event that occurs transitions out of the two level manifold to $|g\rangle$. Furthermore, since there is no driving between $|g\rangle$ and the other states, the population flow is unidirectional and can be detected during any future measurement event. In this way $|g\rangle$ acts as the ancillary state herald we require, and the three level system can be postselected by removal of measurement results $|g\rangle$.

If we interpret this process statistically, the jump events will be expected at a rate governed by γ_{ge} resulting in an expected population

$$\langle \Pi_g \rangle (t) = \langle g | \rho(t) | g \rangle \quad (4.28)$$

where Π_g is the projector onto the ground state. Therefore, the removal of trials where $|g\rangle$ is detected amounts to the removal of $\langle \Pi_g \rangle (t)$ from the overall probability. We can therefore express the postselection of \mathcal{L} as a renormalization relative to the trace of the remaining two level submanifold.

$$\bar{\rho}(t) = \frac{\mathcal{V}[\rho(0)]}{1 - \text{Tr}(\Pi_g \mathcal{V}[\rho(0)])} = \frac{\mathcal{V}|\rho(0)\rangle}{1 - \langle \Pi_g | \mathcal{V} | \rho(0) \rangle} \quad (4.29)$$

Over time the system is expected to fall into the ground state naturally, and so the renormalization becomes increasingly large as the system approaches the resting state.

4.3.1 Transmon Qutrit Experimental Procedure

During an ongoing experiment the system is prepared in $|f\rangle$ using a π -shift from $|g\rangle$, which is the resting state for the system. From here, a short timescale resonant rotation can

transition the system to any state on the ef -Bloch sphere. The system then time evolves under \mathcal{L} , but until a quantum jump occurs the system effectively evolves under \mathcal{H} . After evolving for the specified time, a measurement of the system is made through the frequency shift of an input cavity coherent state. In the event that $|f\rangle$ or $|e\rangle$ are measured, the trial and the measurement are added to the ongoing statistics. However, if $|g\rangle$ is detected then the result is removed, and the total number of trials is not incremented [15].

For a real world transmon circuit, L_{ge} and L_{gf} are not the only dissipators that will be present in the experiment. There will be an additional spontaneous emission dissipator L_{ef} , as well as a phase noise dissipator L_{efz} . As these dissipators are internal to the two level manifold, their quantum jumps cannot be removed through post selection. Luckily, both γ_{ef} and γ_{efz} can be minimized relative to γ_{ge} and the postselection of \mathcal{L} will approximate \mathcal{H} .

4.4 Comparing \mathcal{PT} -Symmetric and Lindbladian Behavior

We are now ready to compare our modified state densities. Inspecting the forms of Eq.4.9 and Eq.4.29, we see that we can neatly express both functions relative to the identity of the two level manifold of the transmon qutrit

$$|\tilde{\rho}(t)\rangle = \frac{\mathcal{U}|\rho(0)\rangle}{\langle \mathbb{1}_{ef} | \mathcal{U} | \rho(0) \rangle} \quad (4.30a)$$

$$|\bar{\rho}(t)\rangle = \frac{\mathcal{V}|\rho(0)\rangle}{\langle \mathbb{1}_{ef} | \mathcal{V} | \rho(0) \rangle} \quad (4.30b)$$

where $\mathbb{1}_{ef} = |f\rangle\langle f| + |e\rangle\langle e|$.

Figure 4.4 compares the time evolution of $\tilde{\rho}(t)$ to $\bar{\rho}(t)$ expressed through their expectation values $\langle \sigma_j \rangle$. The left column lists $\text{Tr}(\sigma_j \tilde{\rho}(t))$, the middle column lists $\text{Tr}(\sigma_j \bar{\rho}(t))$, and the right column lists the difference between the two. We can see from the rightmost column that the two schemes have the same expectation values. This taken together with $\text{Tr}(\tilde{\rho}(t)) = \text{Tr}(\bar{\rho}(t)) = 1$ guarantee that $\tilde{\rho}(t) = \bar{\rho}(t)$.

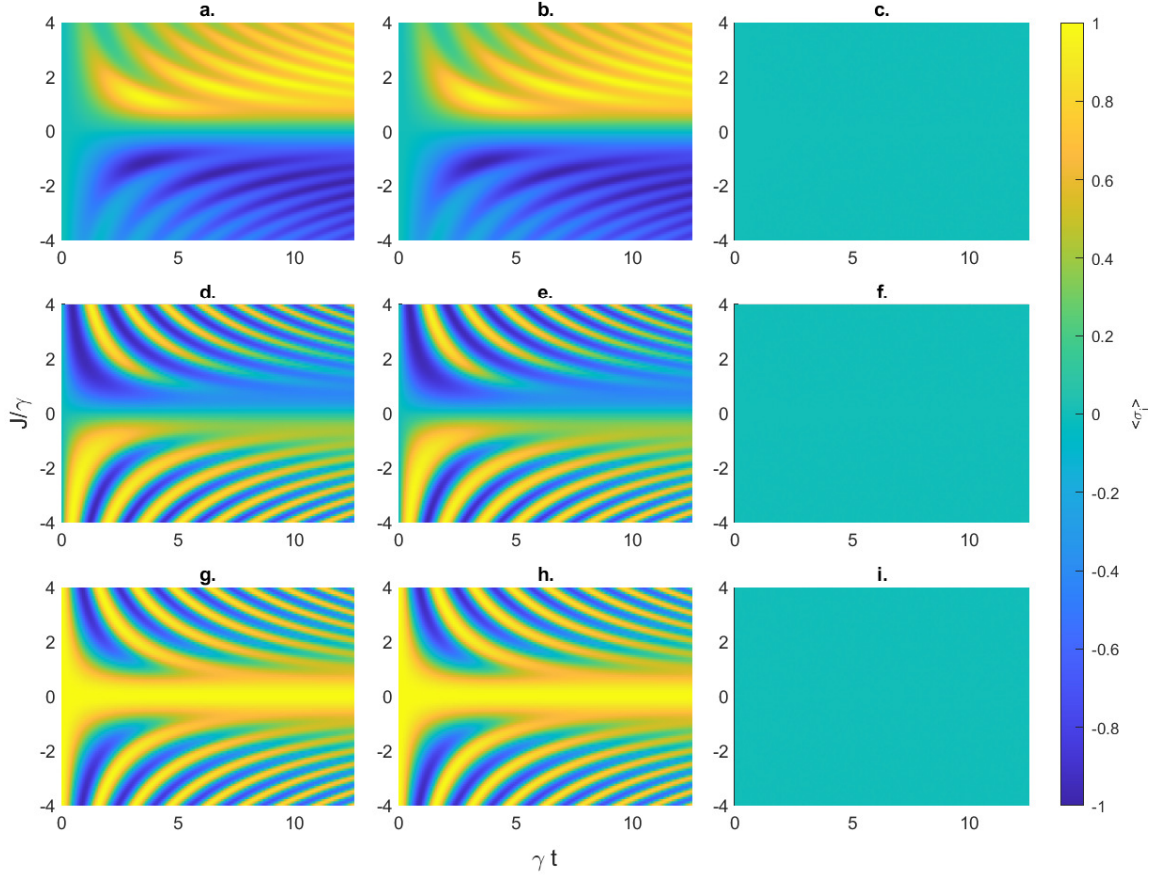


Figure 4.4. Equivalence of Renormalized Non-Hermitian Hamiltonian and Postselected Lindbladian Evolutions: Phase Diagrams comparing the renormalized Liouvillian evolved $\tilde{\rho}$ (Figure 4.4a,d,g) vs the postselected Lindbladian evolved $\bar{\rho}$ (Figure 4.4b,e,h). The difference between the two is then plotted in Figure 4.4c,f,i. Figure 4.4a,b compares $\langle \sigma_x \rangle$, Figure 4.4d,e compares $\langle \sigma_y \rangle$, and Figure 4.4g,h compares $\langle \sigma_z \rangle$. We see from the difference plots that the expectation values are equal. Since the identity element is identical in both cases, all of the elements of the 2×2 state density matrix must be identical, and the evolutions are equivalent. The initial parameters are $\rho(0) = |f\rangle\langle f|$ and $\frac{\Delta}{\gamma_{ge}} = 0.5$.

We have one last subject to cover, which is the interpretation of measurements for renormalized / postselected systems. From Eq.4.30, the forms of measurements for our altered evolutions are

$$\langle Q|\tilde{\rho}(t)\rangle = \frac{\langle Q|\mathcal{U}|\rho(0)\rangle}{\langle \mathbb{1}_{ef}|\mathcal{U}|\rho(0)\rangle} = \frac{\langle Q|\mathcal{V}|\rho(0)\rangle}{\langle \mathbb{1}_{ef}|\mathcal{V}|\rho(0)\rangle} \quad (4.31)$$

However, the exact information that is conveyed through the measurement has some subtleties that require care. For this reason, we now investigate two constructions of the measurements Q through two-time measurement problems used to characterize quantum systems.

4.4.1 Measurement with respect to an External Basis: Leggett-Garg Inequality

The first and simpler of the two possible constructions is to utilize a measurement operator constructed in a basis that is independent of the basis of the measured system. When considering non-Hermitian systems H , measurements of this type are performed with the intention of projecting non-Hermitian states onto an orthonormal basis. We can use measurements of this type to investigate the Leggett Garg Inequality (LGI), which is a temporal correlation function used to characterize if a system requires quantum mechanics to describe effectively [34]–[36].

The LGI parameter K_3 compares the two time sequential correlations of a system

$$K_3 = C_{01} + C_{12} - C_{02} \quad (4.32)$$

where C_{ij} is the correlation function between measurements made at times t_i and t_j . Measurements made at $t_0 = 0$ are made immediately following the preparation of the initial state density $\rho(t)$, and subsequent measurements are normally made under the conditions

$t_1 = t$ and $t_2 = 2t$. We can then express each of the correlation functions in terms of the measurement operator Q and the transition probabilities P_{ij}

$$C_{ij} = \sum_{ij} q_i q_j P_{ij}(\psi_i, \psi_j) \quad (4.33)$$

$$P_{ij}(q_i, q_j) = \frac{|\langle q_j | U_{ij} | q_i \rangle|^2}{|\langle q_i | U_{ij}^\dagger U_{ij} | q_i \rangle|} \frac{|\langle q_i | U_{0i} | \psi_0 \rangle|^2}{|\langle \psi_0 | U_{0i}^\dagger U_{0i} | \psi_0 \rangle|} \quad (4.34)$$

where $|q_j\rangle$ is an eigenstate of Q with eigenvalue q_j , and $U_{ij} = U(t_j, t_i)$ is the time evolution operator from time t_i to t_j . Normally the measurement operator is chosen to be bimodal with $q_\pm = \pm$.

In the standard construction of K_3 in Hermitian systems the normalization in Eq.4.34 is simply 1, but for open systems we require that the transition probabilities sum to 1, and so the normalization is required in our case [37]. Utilizing Eq.4.30, we can cast the transition probabilities in the vectorized representation

$$P_{ij}(q_i, q_j) = \frac{\langle \Pi_j | \mathcal{U} | \Pi_i \rangle \langle \Pi_i | \mathcal{U} | \rho(0) \rangle}{\langle \mathbb{1}_{ef} | \mathcal{U} | \Pi_i \rangle \langle \mathbb{1}_{ef} | \mathcal{U} | \rho(0) \rangle} \quad (4.35a)$$

$$= \frac{\langle \Pi_j | \mathcal{V} | \Pi_i \rangle \langle \Pi_i | \mathcal{V} | \rho(0) \rangle}{\langle \mathbb{1}_{ef} | \mathcal{V} | \Pi_i \rangle \langle \mathbb{1}_{ef} | \mathcal{V} | \rho(0) \rangle} \quad (4.35b)$$

Doing so allows us to investigate K_3 from the perspectives of both non-Hermitian Hamiltonians as well as Lindbladians.

LGI parameter K_3 is utilized as a test of quantum nature by looking for values that are classically forbidden. We will assume that C_{ij} are normalized to $-1 \leq C_{ij} \leq 1$. For a system characterized by definite coordinates and momenta, K_3 can vary from $K_3 = 1$ (an unmoving system) to $K_3 = -3$ (a system that returns to its original configuration). $K_3 > 1$ are algebraically possible, but not physically possible if the motion of the object is deterministic. However, Hermitian quantum systems can reach K_3 as high as $K_3 = 1.5$ (Lüders bound). Thus, systems with $q \leq K_3 \leq 1.5$ are purely quantum in nature, but this marks the physical limit of unitary dynamics. In order to achieve $K_3 > 1.5$ some form of non-linear dynamics are necessary.

For a testing model we will use the passive \mathcal{PT} -dimer ($H_2 - \frac{i\gamma}{2}\mathbb{1}$) with zero detuning. The equivalent Lindbladian model is the Transmon qutrit under the restriction that $\gamma_{ef}, \gamma_{efz} \ll \gamma_{ge}, J$. This makes our Hamiltonian in the energy levels of the transmon qutrit

$$H = -\frac{J}{2}\sigma_x + \frac{i\gamma}{2}\sigma_z - \frac{i\gamma}{2}\mathbb{1} = \begin{bmatrix} 0 & -\frac{J}{2} & 0 \\ -\frac{J}{2} & -i\gamma_1 & 0 \\ 0 & 0 & -\epsilon_g \end{bmatrix} \quad (4.36)$$

For a measurement operator we choose $Q = \sigma_y$ as it lies transverse to the two potentials of H . We will also initialize the system in the eigenstate of Q corresponding to $|q_+\rangle = \frac{1}{\sqrt{2}}(|\uparrow\rangle + \frac{i}{\sqrt{2}}|\downarrow\rangle)$

Figure 4.5 shows the calculation of K_3 as the time between measurements increases. Figure 4.5a shows K_3 calculated using the renormalized Liouvillian approach. Figure 4.5c shows K_3 calculated using the postselected Lindbladian approach (Figure 4.5b shows the proper Lindbladian evolution for reference). We see that near the unitary limit $\frac{J}{\gamma} \rightarrow \infty$ parameter K_3 oscillates between $-3 \leq K_3 \leq 1.5$, with the minimum shown in deep blue and the points near Lüders bound in dull orange. Approaching the exceptional point from the unitary limit, we see that the oscillations occur over an increasing timescale corresponding to $\sqrt{J^2 - \gamma^2}t$. During this approach K_3 increases at the peak of the oscillation from $K_3 = 1.5$ toward the algebraic limit of $K_3 = 3$. At the exceptional point this algebraic limit is finally achieved, but this occurs at $\gamma t \rightarrow \infty$ and so is not observable. Beyond the exceptional point K_3 does not develop much, and the parameter is instead pulled toward $K_3 = 0$ signifying that measurements are completely uncorrelated with each other.

This however is not a complete description of the system. If we optimize our choice of Q and $\rho(0)$ for the maximum achievable K_3 at each $\frac{J}{\gamma}$, we will find that the maximum for both is always achieved on the yz plane of the Bloch sphere. For the \mathcal{PT} -symmetric regime the choice any point along the geodesic will maximize K_3 so long as $\rho(0) = |q_+\rangle\langle q_+|$, though

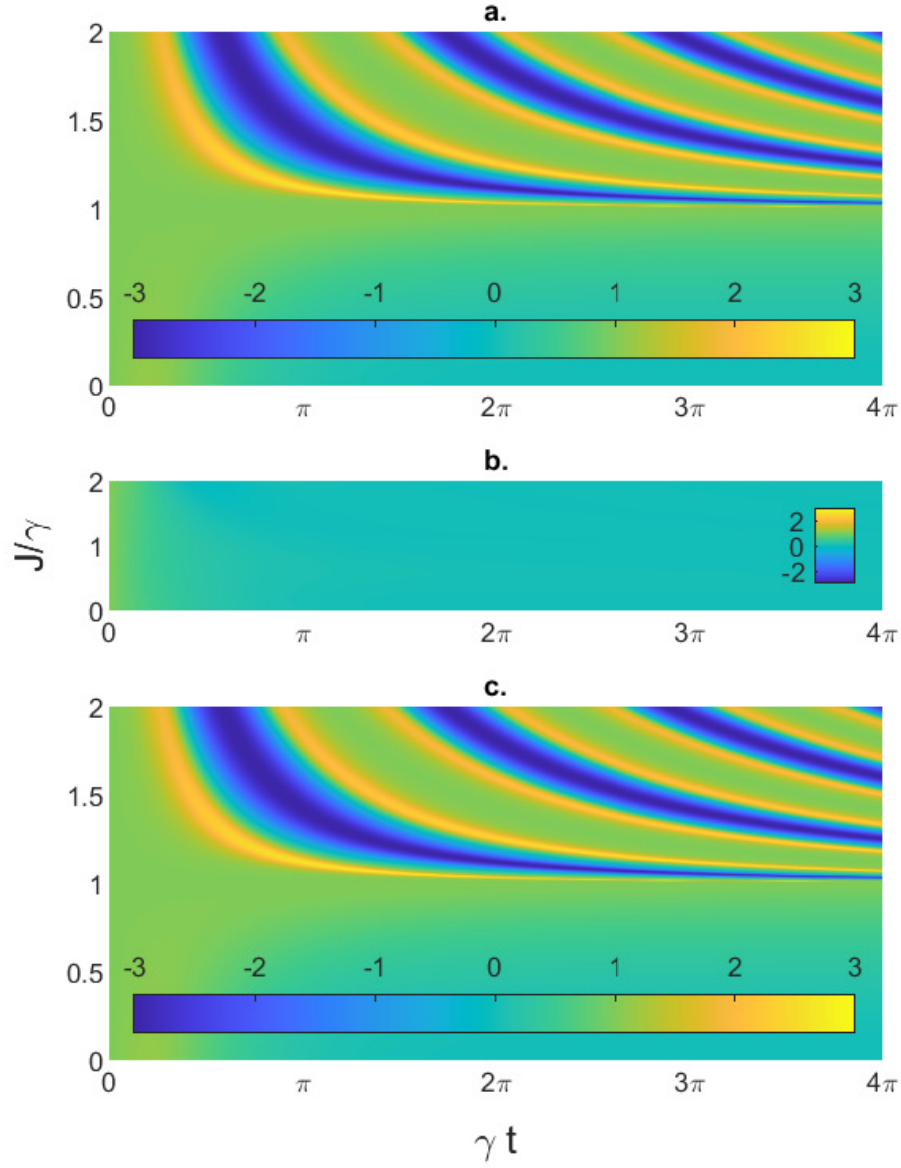


Figure 4.5. K_3 Parameter Comparison: Phase Diagrams comparing K_3 calculated from the renormalized Liouvillian evolved $\tilde{\rho}$ (Figure 4.5a) vs the postselected Lindbladian evolved $\bar{\rho}$ (Figure 4.5c). The full Lindbladian evolution is shown for reference in Figure 4.5b. We can clearly see the presence of oscillatory behavior near the unitary limit $\frac{J}{\gamma} \rightarrow \infty$. As we approach the exceptional point $\frac{J}{\gamma} = 1$ the timescale of the oscillations increase, while the peak K_3 during the oscillation approaches the algebraic limit $K_3 \rightarrow 3$, and achieves the limit at the exceptional point. In the \mathcal{PT} -broken regime we observe $K_3 \rightarrow 0$, signifying the system becoming highly uncorrelated.

they will maximize at different initial times. However, in the \mathcal{PT} -broken regime we must choose a starting state and measurement slightly off of a particular eigenstate of H

$$\rho(0) \approx |\epsilon_{-}\rangle \langle \epsilon_{-}| \quad (4.37)$$

$$Q \approx |\epsilon_{-}\rangle \langle \epsilon_{-}| - \frac{|\epsilon_{+}\rangle \langle \epsilon_{+}|}{\langle \langle \epsilon_{+} | \epsilon_{+} \rangle \rangle} \quad (4.38)$$

The two eigenstates of H are $|\epsilon_{\pm}\rangle$ and divide geodesic along the yz -plane into a major arc and minor arc, and the specific perturbation we need to maximize K_3 places us on the major arc. For our perturbation we rotate from $|\epsilon_{\pm}\rangle$ using $R(\delta\theta) = e^{i\delta\theta\sigma_x}$, where $\delta\theta$ is a small perturbation strength $\approx 10^{-3}$. We cannot choose to remove the perturbation entirely as the eigenstate is “stable” and the system will not evolve away from $|\epsilon_{\pm}\rangle$.

Figure 4.6 shows the phase diagram for K_3 once the optimization is implemented. We see that the \mathcal{PT} -symmetric regime is identical to before, as our initial choice of Q and $\rho(0)$ happened to already be optimal in this region. The \mathcal{PT} -broken regime however looks strikingly different. We now see a large wavefront that does not repeat in t and spans the entire \mathcal{PT} -broken regime. At the peak of this wavefront $K_3 \approx 3$. The approximation is caused by the perturbation $R(\delta\theta)$, where reducing $\delta\theta \rightarrow 0$ causes $K_3 \rightarrow 3$, but also causes $t_{peak} \rightarrow \infty$.

We can find a simple understanding of the system by casting $\rho(t)$ as a Bloch vector $\vec{S}(t)$ whose elements are

$$\vec{S} = \sum_{j=x,y,z} S_j \hat{j} \quad (4.39)$$

$$S_j(0) = \langle \sigma_j | \rho(0) \rangle \quad (4.40)$$

$$S_k(0) = \sum_{j=x,y,z} \langle \sigma_k | \mathcal{U} | \sigma_j \rangle S_j \quad (4.41)$$

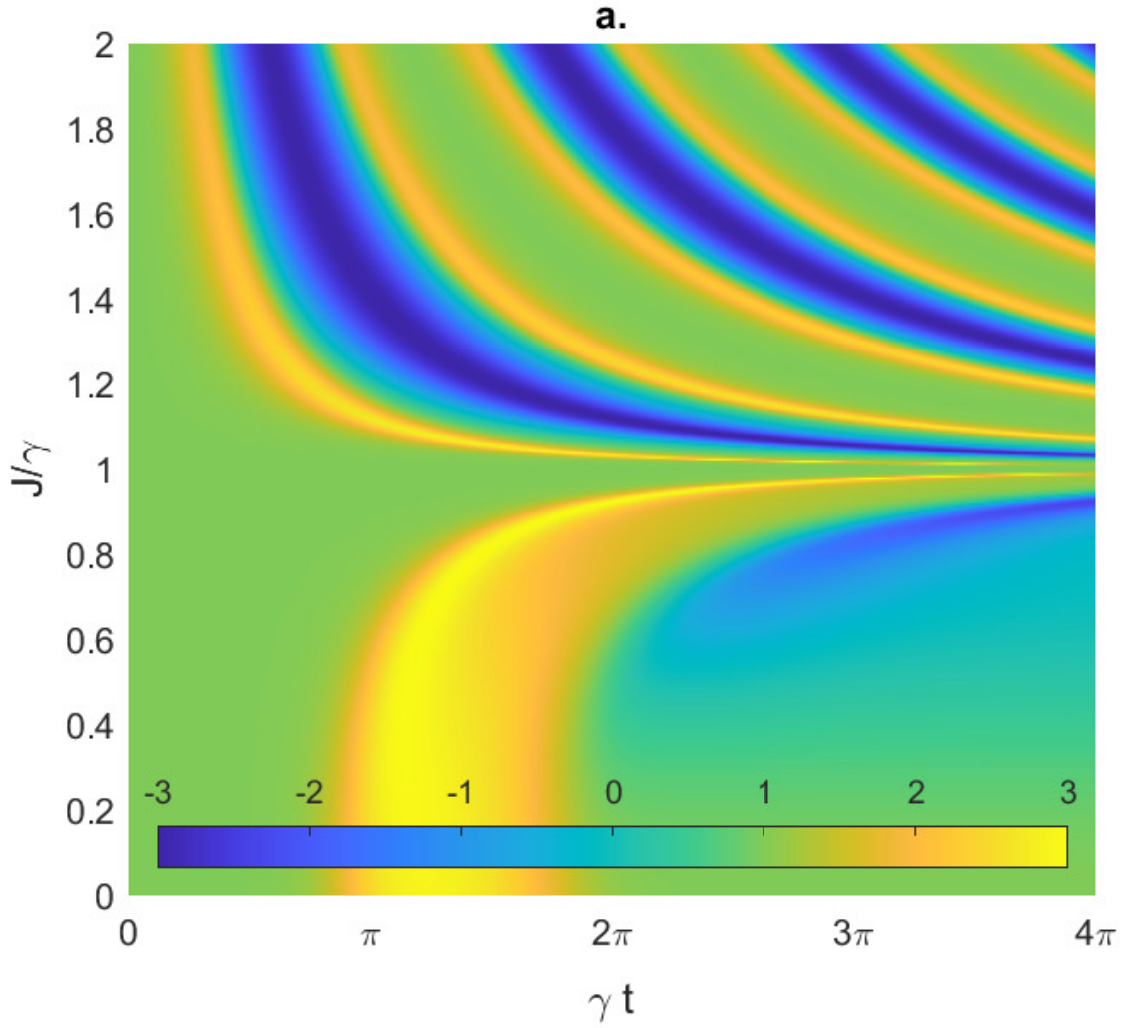


Figure 4.6. K_3 Parameter Maximization: Phase Diagram showing K_3 maximized for each $\frac{J}{\gamma}$ utilizing the optimal Q and $\rho(0)$ listed in Eq.4.37. The \mathcal{PT} -symmetric regime is identical to before. On the other hand, the \mathcal{PT} -broken regime now hosts a single major wavefront where $K_3 \approx 3$. The height of K_3 increases as the perturbation off of $|\epsilon_{-}\rangle$ is reduced, however doing so pushes the peak of the wavefront out to longer times.

where \hat{x} , \hat{y} , and \hat{z} are unit vectors of cartesian space. If we implement this Bloch vector representation in the non-linear master equation Eq.4.10 we are left with

$$\partial_t \vec{S} = \underbrace{\vec{A} \times \vec{S}}_{(1)} + \underbrace{\vec{B} - \text{Tr}(\vec{B} \cdot \vec{S})\vec{S}}_{(2)} \quad (4.42a)$$

$$\vec{A} = \sum_{j=x,y,z} \frac{1}{2} (\langle \sigma_j | H \rangle + \langle \sigma_j | H^\dagger \rangle) \hat{j} \quad (4.42b)$$

$$\vec{B} = \sum_{j=x,y,z} \frac{1}{2i} (\langle \sigma_j | H \rangle - \langle \sigma_j | H^\dagger \rangle) \hat{j} \quad (4.42c)$$

where \vec{A} is the vector representation of the Hermitian components of H , and \vec{B} is the vector representation of the anti-Hermitian components of H . Term (1) in Eq.4.42 produces rotations with axis \vec{A} as found in the traditional Rabi problem. Term (2) in Eq.4.42 is equivalent to the component of \vec{B} tangent to the Bloch sphere at the point \vec{S} . This term will result in a source forming on the Bloch sphere at $-\vec{B}$ and a sink forming at \vec{B} . The combination of these two potentials will result in either stable orbits or sources and sinks existing on the Bloch sphere.

We can find an analytic solution to Eq.4.42 by changing from the cartesian basis to a basis aligned with \vec{A} , \vec{B} , and the orthogonal direction $\vec{n} = \vec{A} \times \vec{B}$

$$\partial_t S_A = -|B| S_A S_B \quad (4.43)$$

$$\partial_t S_B = -|A| S_n + |B| - |B| S_B^2 \quad (4.44)$$

$$\partial_t S_n = |A| S_B - |B| S_B S_n \quad (4.45)$$

Considering that the maximal K_3 occurs on the plane perpendicular to \vec{A} , we can set $S_A = 0$ and solve the other two components

$$S_B(t) = -\frac{\Omega \sin(\Omega t + C)}{A + B \cos(\Omega t + C)} \quad (4.46)$$

$$S_n(t) = \frac{B + A \cos(\Omega t + C)}{A + B \cos(\Omega t + C)} \quad (4.47)$$

where $\Omega = \sqrt{A^2 - B^2}$

In our example case, \vec{A} and \vec{B} are perpendicular which causes the source and sink to exist on the yz -plane. Beginning near the source, $\vec{S}(t)$ will spend a large amount of time with low velocity until deviating far enough from the source to experience a large acceleration that suddenly transitions $\vec{S}(t)$ near the sink state. The act of measuring the $\vec{S}(t)$ projects \vec{S} either to a point near the source or a point midway along the “fall”, and so if done soon enough acts to realign the system to its initial conditions. The wavefront we observe in Figure 4.6 represents the time at which this realignment can no longer occur, and so the short time correlations $C_{01} = C_{12}$ remain near one, while the slightly longer time correlation C_{02} experiences a complete inversion of the system. The peak of the wavefront where $K_3 = 3$ occurs when the measurement time $2t$ would occur precisely when $\vec{S}(t)$ is falling past the point opposite the source.

Finally, we will consider the effect that the dissipators L_{ef} and L_{efz} will have upon K_3 . Figure 4.7 shows the effect of non-removable quantum jumps on the phase diagram of K_3 . We see in Figure 4.7b the effect of L_{ef} . The decoherences have depressed K_3 across the phase diagram, but the strongest effect is seen near the non-Hermitian exceptional point $\frac{J}{\gamma} = 1$ where K_3 is pulled near $K_3 = 1$. Figure 4.7c shows L_{efz} has a similar effect that is even worse in the \mathcal{PT} -broken regime. In both figures the only regions with $K_3 \approx 3$ are $\frac{J}{\gamma} < 0.25$. As a relative strength of $\frac{\gamma_{ef}}{\gamma_{ge}} = \frac{\gamma_{efz}}{\gamma_{ge}} = 10^{-2}$ is about the limit of what can be currently engineered in the transmon circuit, observing $K_3 = 3$ will prove difficult.

4.4.2 Measurement with respect to a Non-Orthogonal Basis: Jarzynski Equality

The second, and more subtle, construction of measurement operators seek to identify the current components of ρ . For a Hermitian system this is identical to the previous construction, but for non-Hermitian systems this requires that we measure a non-Hermitian basis with another non-Hermitian basis.

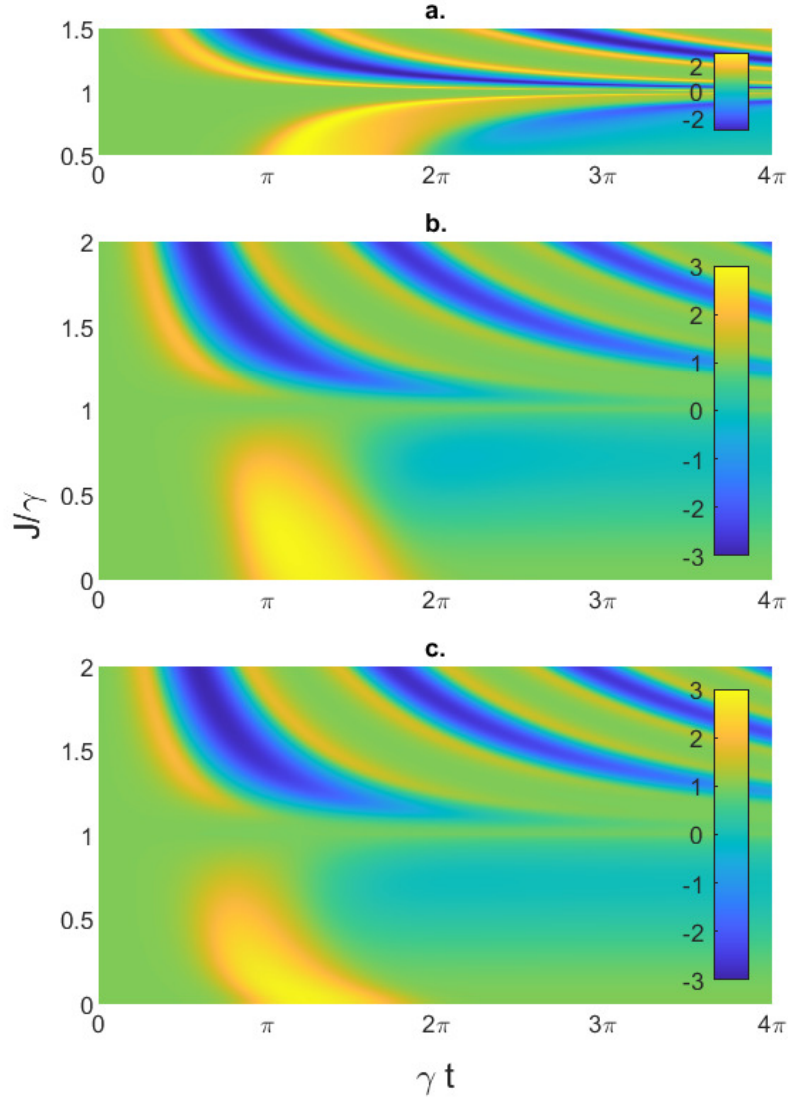


Figure 4.7. Effect of Non-removable Quantum Jumps on K_3 : Phase Diagram showing K_3 maximized for each $\frac{J}{\gamma}$ utilizing the optimal Q and $\rho(0)$ listed in Eq.4.37. This time we have included non-removable jumps originating from the dissipators L_{ef} and L_{efz} , with $\frac{\gamma_{ef}}{\gamma_{ge}} = \frac{\gamma_{efz}}{\gamma_{ge}} = 10^{-2}$. The effect of L_{ef} is shown in Figure 4.7b and the effect of L_{efz} is shown in Figure 4.7b. A section of Figure 4.6 near the exceptional point is provided in 4.7a for reference. We see that K_3 near the exceptional point has been forced to $K_3 = 1$, and the surrounding K_3 have been depressed. The only regions with $K_3 \approx 3$ are with strong dissipation.

We can use a measurement of this type to investigate Jarzynski's Equality (JE) [38]–[40], according to which the expectation of the exponentiated work is equivalent to the exponentiated Helmholtz free energy

$$\langle e^{-\beta W} \rangle = e^{-\beta \Delta F} \quad (4.48)$$

where β is related to temperature as $\beta = \frac{1}{k_b T}$, W is the work done during the evolution of the system, and ΔF is the Helmholtz free energy. For ΔF we will utilize the established definition related to the change of the partition function of the system [39]

$$e^{-\beta \Delta F} = \frac{Z(t)}{Z(0)} = \frac{\sum_j e^{-\beta \epsilon_j(t)}}{\sum_j e^{-\beta \epsilon_j(0)}} \quad (4.49)$$

The next major step will be clearly defining the average exponentiated work $\langle e^{-\beta W} \rangle$. Starting with a state density defined in the energy basis $|\epsilon_j\rangle$, we define the work done during time evolution from state $|\epsilon_i\rangle$ to state $|\epsilon_j\rangle$ as $W_{ij} = \epsilon_j - \epsilon_i$. The average work for a given evolution \mathcal{V} is then predicated on two factors:

1. p_i : the distribution of energy states $|\epsilon_i\rangle$ in the initial state density.
2. P_{ij} : the transition probability between each initial state $|\epsilon_i\rangle$ and each final state $|\epsilon_j\rangle$.

The average work is then defined by the double summation

$$\langle W \rangle = \sum_{i,j} W_{ij} P_{ij} p_i \quad (4.50)$$

or we can modify the relative weights for each possible configuration to obtain the average exponentiated work

$$\langle e^{-\beta W} \rangle = \sum_{i,j} e^{-\beta W_{ij}} P_{ij} p_i \quad (4.51)$$

where we have inserted a scaling parameter β with units of inverse energy which we interpret as $\beta = \frac{1}{k_b T}$. Setting the initial probabilities as

$$p_i = \frac{e^{-\beta \epsilon_i}}{\sum_i e^{-\beta \epsilon_i}} \quad (4.52)$$

will then associate the initial state density with the thermal state.

The goal of an experimental validation then is to determine each of the transition probabilities P_{ij} . However, unlike in Hermitian systems the trace cannot simply be decomposed as a sum of projections onto the energy basis. The choice of measurement operators is therefore a subtle, but deeply important convention. If we were to propose utilizing measurement operators constructed from the right-eigenstate basis

$$\Pi_j = |\epsilon_j\rangle \langle \epsilon_j| \quad (4.53)$$

$$Q = \sum_j q_j \Pi_j \quad (4.54)$$

$$\rho(0) = \sum_j \eta_j \Pi_j \quad (4.55)$$

Such projectors can be experimentally produced from resonant rotations of the intended projector onto a preferred basis. In the case of the superconducting qutrit, this amounts to $\Pi_j \rightarrow \Pi_f = R \Pi_j R^\dagger$. The problem with such a measurement stems from the non-orthogonality of the eigenbasis. Consider the TLS with a static or periodic Hamiltonian $H(t)$. Beginning with a pure state $|\epsilon_+\rangle$, the final state density takes the form

$$|\rho(t)\rangle = \mathcal{V} |\Pi_+\rangle = P_{++} \Pi_+ + P_{+-} \Pi_- + P_{+g} \Pi_g \quad (4.56)$$

where $0 \leq \{P_{++}, P_{+-}, P_{+g}\} \leq 1$ and $P_{++} + P_{+-} + P_{+g} = 1$. Performing a projective measurement onto the $|\epsilon_+\rangle$ would then yield

$$\langle \Pi_+ | \rho(t) \rangle = P_{++} + \alpha P_{+-} \quad (4.57)$$

where $\alpha = |\langle \epsilon_+ | \epsilon_- \rangle|^2$. Therefore, measurements onto the right-projectors overestimate the transition probabilities by an amount proportional to the non-orthogonal overlap factor α . Seeing this one could attempt to correct for α by renormalizing with respect to the new probability total, but this would yield for Eq.4.51

$$\frac{\langle e^{-\beta W} \rangle}{N} = \frac{\sum_{i,j} e^{-\beta W_{ij}} \langle \Pi_j | \mathcal{V} | \Pi_i \rangle p_i}{\sum_{i,j} \langle \Pi_j | \mathcal{V} | \Pi_i \rangle p_i} \quad (4.58)$$

$$= \frac{\langle e^{-\beta W} \rangle + \langle e^{2\beta E_{av}} \rangle \alpha}{1 + \alpha} \quad (4.59)$$

The proper way to form measurement operators of this construction is from the left-eigenstate basis

$$\Xi_j = \frac{|\epsilon_j\rangle\langle\epsilon_j|}{\langle\epsilon_j|\epsilon_j\rangle} \quad (4.60)$$

$$Q = \sum_j q_j \Xi_j \quad (4.61)$$

$$\rho(0) = \sum_j p_j \Pi_j \quad (4.62)$$

Taking a measurement then yields the transition probability as intended

$$\langle \Xi_j | \mathcal{V} | \Pi_i \rangle = P_{ij} \quad (4.63)$$

which can be used to properly determine Eq.4.51.

To test the Jarzynski Equality for non-Hermitian systems we will use the time periodic \mathcal{PT} -dimer $H_2(t)$ with sinusoidal modulation

$$H_2(t) = \frac{J(t)}{2} \sigma_x + i \frac{\gamma}{2} \sigma_z \quad (4.64a)$$

$$J(t) = \frac{J_{max} + J_{min}}{2} \cos\left(\frac{2\pi}{T}t\right) \quad (4.64b)$$

Just as with the Floquet Lindbladians (Ch.2.4.1), an analytic solution is not available for sinusoidal modulation, and so we discretize \mathcal{U}_F and calculate $\langle e^{-\beta W} \rangle$ numerically. The reason we have chosen to use this periodic potential is it simplifies the interpretation of ΔF . As the

system returns to its original configuration, we expect that there is no change in the state variables, and so

$$e^{-\beta\Delta F} = 1 \tag{4.65}$$

Figure 4.8 shows the phase diagram for $\langle e^{-\beta W} \rangle$ as J_{min} and T are varied. We see that above the exceptional point $\frac{J_{min}}{\gamma} = 1$ the phase diagram asymptotically approaches the value predicted by the free energy $e^{-\beta\Delta F} = 1$. Below the exceptional point we see large oscillations that stretch from $0.75 \leq \langle e^{-\beta W} \rangle \leq 1.5$. One possible explanation for this feature is that below the exceptional point $J(t)$ will trace a path that encircles the exceptional point, leading to a mode switching behavior that inverts the system. However, the transition between the regions begins to occur before the exceptional point is encircled, and becomes especially noticeable in the high frequency regime $T \rightarrow 0$. Further down we see thin breaks in the oscillations that approach the opposite exceptional point $\frac{J_{min}}{\gamma} = -1$. A likely cause of these are a resonant effect requiring both exceptional points which should have opposing residues.

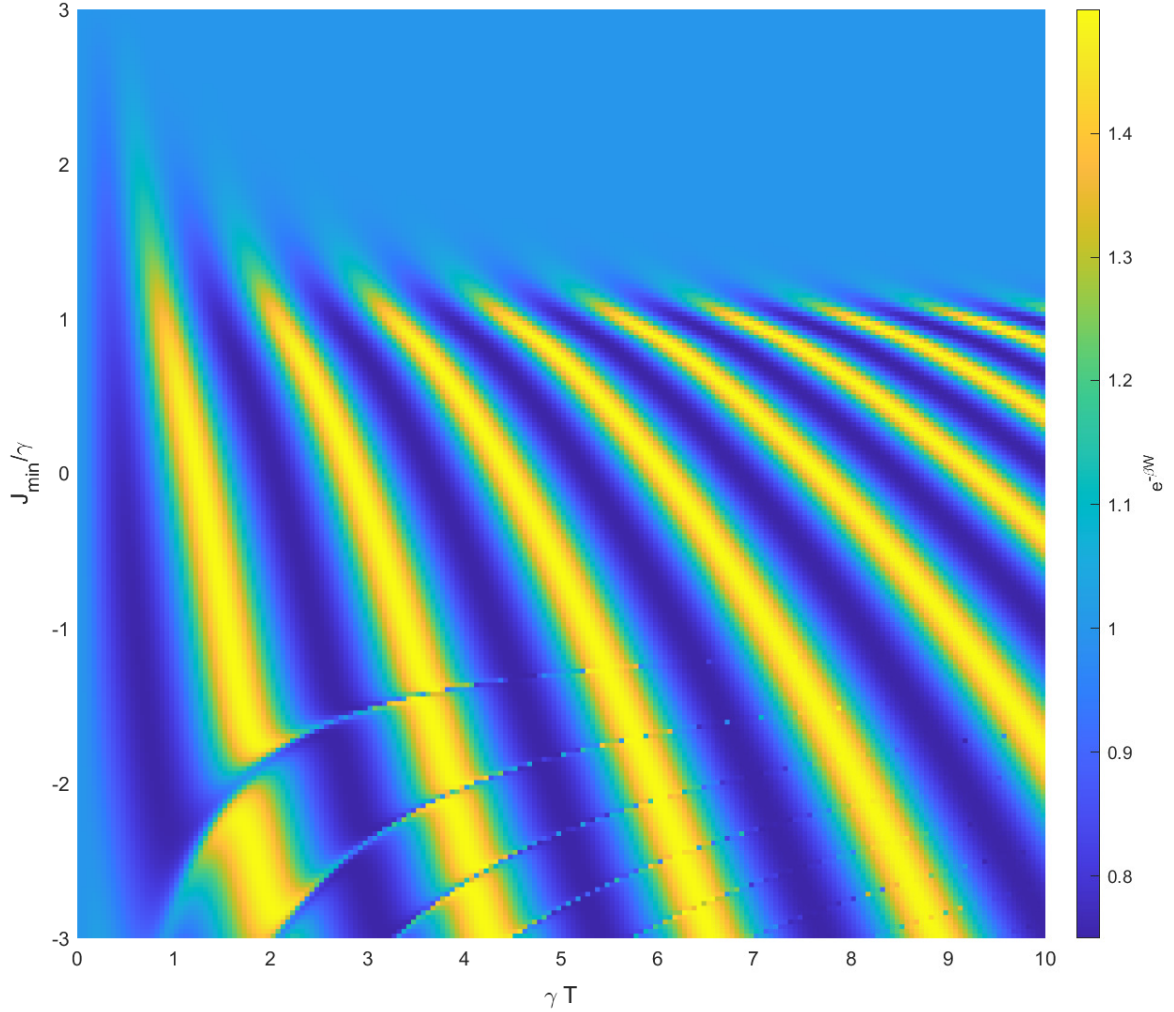


Figure 4.8. Exponentiated Work for Jarzynski's Equality: Phase Diagram showing $\langle e^{-\beta W} \rangle$ with $\frac{J_{max}}{\gamma} = 3$, $\gamma\beta = 1$, and ρ_0 in the thermal state. Above the exceptional point $\frac{J_{min}}{\gamma} = 1$ the function $\langle e^{-\beta W} \rangle$ approaches the predicted value of 1, while below the exceptional point the path traced by $J(t)$ encircles the exceptional point and large oscillations in $\langle e^{-\beta W} \rangle$ occur. However, the transition is smooth and we see deviations from the predicted value grow before the exceptional point is encircled. After passing the opposite exceptional point $\frac{J_{min}}{\gamma} = -1$, we see thin resonance lines appear.

5. SUMMARY

Throughout this work we have investigated the behavior of open quantum system through a variety of approaches. In Chapter 1, we introduced non-Hermitian Hamiltonians, non-unitary evolution, the concept of exceptional points. Through the lenses of \mathcal{PT} -symmetry and pseudo-hermiticity, we examined how symmetries and constants of motion diverge under such non-conservative systems. In Chapter 2, we introduced quantum maps, Kraus operators, and Lindbladian evolution. Utilizing Floquet analysis, we then investigated the presence of exceptional points in these periodically driven, decohering systems. In Chapter 3, we specified how to construct a cavity coupled transmon circuit for studying Lindbladian evolution. Finally, in Chapter 4 we illustrated the similarities between non-Hermitian evolution and Lindbladian evolution, and found that under specific circumstances we can use postselected Lindbladians to study renormalized non-Hermitian Hamiltonians. We then used this equivalence to study two tests of quantum reality in non-conservative systems.

Over the last quarter century, the concepts of \mathcal{PT} -symmetry and pseudo-hermiticity have developed and expanded under intense scrutiny. The non-unitary but coherent evolution they give rise to pose deep physical questions that test the limits of unitary quantum mechanics. However, experiments in evanescently coupled waveguides [3], ultra-cold atoms [5], and superconducting circuits [6] demonstrate that exceptional points are real, physically observable, and fully quantum phenomena.

The field still has many avenues for growth. Effective models of gain in \mathcal{PT} -symmetric systems require non-linear analysis, as their continuous growth eventually results in physically impossible state-densities theoretically, and saturation effects experimentally. Similarly, models for the recoherence of systems at long timescales are still being worked on. Our efforts show that non-linear effects arising from renormalized linear maps pose an intriguing avenue for developing such theories.

We look forward to the development of this field, and our continued inquiry into open quantum systems, for many years to come.

REFERENCES

- [1] Y. Ashida, Z. Gong, and M. Ueda, “Non-hermitian physics,” 2020. DOI: [10.48550/ARXIV.2006.01837](https://doi.org/10.48550/ARXIV.2006.01837).
- [2] C. M. Bender and S. Boettcher, “Real spectra in non-hermitian hamiltonians having pt symmetry,” *Physical Review Letters*, vol. 80, no. 24, pp. 5243–5246, Jun. 1998. DOI: [10.1103/physrevlett.80.5243](https://doi.org/10.1103/physrevlett.80.5243).
- [3] C. E. Rüter, K. G. Makris, R. El-Ganainy, D. N. Christodoulides, M. Segev, and D. Kip, “Observation of parity–time symmetry in optics,” *Nature Physics*, vol. 6, no. 3, pp. 192–195, Jan. 2010. DOI: [10.1038/nphys1515](https://doi.org/10.1038/nphys1515).
- [4] Y. N. Joglekar and A. K. Harter, “Passive parity-time-symmetry-breaking transitions without exceptional points in dissipative photonic systems [invited],” *Photonics Research*, vol. 6, no. 8, A51, Jul. 2018. DOI: [10.1364/prj.6.000a51](https://doi.org/10.1364/prj.6.000a51). [Online]. Available: <https://doi.org/10.1364/prj.6.000a51>.
- [5] J. Li, A. K. Harter, J. Liu, L. de Melo, Y. N. Joglekar, and L. Luo, “Observation of parity-time symmetry breaking transitions in a dissipative floquet system of ultracold atoms,” *Nature Communications*, vol. 10, no. 1, Feb. 2019. DOI: [10.1038/s41467-019-08596-1](https://doi.org/10.1038/s41467-019-08596-1).
- [6] M. Naghiloo, M. Abbasi, Y. N. Joglekar, and K. W. Murch, “Quantum state tomography across the exceptional point in a single dissipative qubit,” *Nature Physics*, vol. 15, no. 12, pp. 1232–1236, Oct. 2019. DOI: [10.1038/s41567-019-0652-z](https://doi.org/10.1038/s41567-019-0652-z). [Online]. Available: <https://doi.org/10.1038/s41567-019-0652-z>.
- [7] F. Minganti, A. Miranowicz, R. W. Chhajlany, and F. Nori, “Quantum exceptional points of non-hermitian hamiltonians and liouvillians: The effects of quantum jumps,” *Physical Review A*, vol. 100, no. 6, Dec. 2019. DOI: [10.1103/physreva.100.062131](https://doi.org/10.1103/physreva.100.062131). [Online]. Available: <https://doi.org/10.1103/physreva.100.062131>.
- [8] J. Sakurai and J. Napolitano, *Modern Quantum Mechanics*, ser. . Addison-Wesley, 2011, ISBN: 9780805382914. [Online]. Available: <https://books.google.com/books?id=N4I-AQAACAAJ>.
- [9] C. Bender, R. Tateo, P. Dorey, *et al.*, *Pt Symmetry: In Quantum And Classical Physics*. World Scientific Publishing Company, 2018, ISBN: 9781786345974. [Online]. Available: <https://books.google.com/books?id=5PF9DwAAQBAJ>.
- [10] F. Ruzicka, K. S. Agarwal, and Y. N. Joglekar, “Conserved quantities, exceptional points, and antilinear symmetries in non-hermitian systems,” *Journal of Physics: Conference Series*, vol. 2038, no. 1, p. 012021, Oct. 2021. DOI: [10.1088/1742-6596/2038/1/012021](https://doi.org/10.1088/1742-6596/2038/1/012021).

- [11] A. Mostafazadeh, “Pseudo-hermitian representation of quantum mechanics,” 2008. DOI: [10.48550/ARXIV.0810.5643](https://doi.org/10.48550/ARXIV.0810.5643).
- [12] A. Mostafazadeh, “PSEUDO-HERMITIAN REPRESENTATION OF QUANTUM MECHANICS,” *International Journal of Geometric Methods in Modern Physics*, vol. 07, no. 07, pp. 1191–1306, Nov. 2010, [arXiv:0810.5643v4 \[quant-ph\]](https://arxiv.org/abs/0810.5643v4). DOI: [10.1142/s0219887810004816](https://doi.org/10.1142/s0219887810004816). [Online]. Available: <https://doi.org/10.1142/s0219887810004816>.
- [13] A. Fring, *An introduction to pt -symmetric quantum mechanics – time-dependent systems*, 2022. DOI: [10.48550/ARXIV.2201.05140](https://doi.org/10.48550/ARXIV.2201.05140).
- [14] A. K. Harter, “Aspects of parity-time symmetry breaking in discrete, classical and quantum open systems,” Ph.D. dissertation, Purdue University, West Lafayette, 2018.
- [15] M. Naghiloo, *Introduction to experimental quantum measurement with superconducting qubits*, 2019. DOI: [10.48550/ARXIV.1904.09291](https://doi.org/10.48550/ARXIV.1904.09291).
- [16] G. E. Santoro, “Introduction to floquet,” ser. SISSA, 2017. [Online]. Available: https://www.ggi.infn.it/sft/SFT_2019/LectureNotes/Santoro.pdf.
- [17] M. A. Quiroz-Juárez, Z. A. Cochran, J. L. Aragón, Y. N. Joglekar, and R. de J. León-Montiel, “Parity-time symmetry via time-dependent non-unitary gauge fields,” Sep. 2021. [arXiv: 2109.03846 \[physics.class-ph\]](https://arxiv.org/abs/2109.03846).
- [18] M. A. Quiroz-Juárez, K. S. Agarwal, Z. A. Cochran, J. L. Aragón, Y. N. Joglekar, and R. d. J. León-Montiel, *On-demand parity-time symmetry in a lone oscillator through complex, synthetic gauge fields*, 2021. DOI: [10.48550/ARXIV.2109.03846](https://doi.org/10.48550/ARXIV.2109.03846).
- [19] S. Milz, F. A. Pollock, and K. Modi, “An introduction to operational quantum dynamics,” *Open Systems & Information Dynamics*, vol. 24, no. 04, p. 1740016, Dec. 2017. DOI: [10.1142/s1230161217400169](https://doi.org/10.1142/s1230161217400169). [Online]. Available: <https://doi.org/10.1142/s1230161217400169>.
- [20] M.-D. Choi, “Completely positive linear maps on complex matrices,” *Linear Algebra and its Applications*, vol. 10, no. 3, pp. 285–290, 1975, ISSN: 0024-3795. DOI: [https://doi.org/10.1016/0024-3795\(75\)90075-0](https://doi.org/10.1016/0024-3795(75)90075-0). [Online]. Available: <http://www.sciencedirect.com/science/article/pii/0024379575900750>.
- [21] T. F. Havel, “Robust procedures for converting among lindblad, kraus and matrix representations of quantum dynamical semigroups,” *Journal of Mathematical Physics*, vol. 44, no. 2, pp. 534–557, 2003. DOI: [10.1063/1.1518555](https://doi.org/10.1063/1.1518555). eprint: <https://aip.scitation.org/doi/pdf/10.1063/1.1518555>. [Online]. Available: <https://aip.scitation.org/doi/abs/10.1063/1.1518555>.

- [22] S. Milz and K. Modi, “Quantum stochastic processes and quantum non-markovian phenomena,” *PRX Quantum*, vol. 2, no. 3, p. 030 201, Jul. 2021. DOI: [10.1103/prxquantum.2.030201](https://doi.org/10.1103/prxquantum.2.030201).
- [23] P. Figueroa–Romero, F. A. Pollock, and K. Modi, “Markovianization with approximate unitary designs,” *Communications Physics*, vol. 4, no. 1, Jun. 2021. DOI: [10.1038/s42005-021-00629-w](https://doi.org/10.1038/s42005-021-00629-w).
- [24] P. Figueroa-Romero, F. A. Pollock, and K. Modi, *Markovianization by design*, 2020. arXiv: [2004.07620](https://arxiv.org/abs/2004.07620) [quant-ph].
- [25] A. Schnell, A. Eckardt, and S. Denisov, “Is there a floquet lindbladian?” *Physical Review B*, vol. 101, no. 10, Mar. 2020. DOI: [10.1103/physrevb.101.100301](https://doi.org/10.1103/physrevb.101.100301). [Online]. Available: <https://doi.org/10.1103/physrevb.101.100301>.
- [26] V. V. Albert and L. Jiang, “Symmetries and conserved quantities in lindblad master equations,” *Physical Review A*, vol. 89, no. 2, p. 022 118, Feb. 2014. DOI: [10.1103/physreva.89.022118](https://doi.org/10.1103/physreva.89.022118).
- [27] V. V. Albert, “Lindbladians with multiple steady states: Theory and applications,” 2018. DOI: [10.48550/ARXIV.1802.00010](https://doi.org/10.48550/ARXIV.1802.00010).
- [28] T. E. Lee and Y. N. Joglekar, “Pt-symmetric rabi model: Perturbation theory,” *Physical Review A*, vol. 92, no. 4, p. 042 103, Oct. 2015. DOI: [10.1103/physreva.92.042103](https://doi.org/10.1103/physreva.92.042103).
- [29] F. Bloch and A. Siegert, “Magnetic resonance for nonrotating fields,” *Physical Review*, vol. 57, no. 6, pp. 522–527, Mar. 1940. DOI: [10.1103/physrev.57.522](https://doi.org/10.1103/physrev.57.522).
- [30] C. Cohen-Tannoudji, J. Dupont-Roc, and C. Fabre, “A quantum calculation of the higher order terms in the bloch-siegert shift,” *Journal of Physics B: Atomic and Molecular Physics*, vol. 6, no. 8, pp. L214–L217, Aug. 1973. DOI: [10.1088/0022-3700/6/8/007](https://doi.org/10.1088/0022-3700/6/8/007).
- [31] C. Cohen-Tannoudji, J. Dupont-Roc, and C. Fabre, “An experimental check of higher order terms in the radiative shift of a coherence resonance,” *Journal of Physics B: Atomic and Molecular Physics*, vol. 6, no. 8, pp. L218–L221, Aug. 1973. DOI: [10.1088/0022-3700/6/8/008](https://doi.org/10.1088/0022-3700/6/8/008).
- [32] S. Rasmussen, K. Christensen, S. Pedersen, *et al.*, “Superconducting circuit companion—an introduction with worked examples,” *PRX Quantum*, vol. 2, no. 4, p. 040 204, Dec. 2021. DOI: [10.1103/prxquantum.2.040204](https://doi.org/10.1103/prxquantum.2.040204).
- [33] S. M. Girvin, “Circuit QED: Superconducting qubits coupled to microwave photons,” in *Quantum Machines: Measurement and Control of Engineered Quantum Systems*, Oxford University Press, Jun. 2014, pp. 113–256. DOI: [10.1093/acprof:oso/9780199681181.003.0003](https://doi.org/10.1093/acprof:oso/9780199681181.003.0003). [Online]. Available: <https://doi.org/10.1093/acprof:oso/9780199681181.003.0003>.

- [34] A. J. Leggett and A. Garg, “Quantum mechanics versus macroscopic realism: Is the flux there when nobody looks?” *Physical Review Letters*, vol. 54, no. 9, pp. 857–860, Mar. 1985. DOI: [10.1103/physrevlett.54.857](https://doi.org/10.1103/physrevlett.54.857).
- [35] A. J. Leggett, “Testing the limits of quantum mechanics: Motivation, state of play, prospects,” *Journal of Physics: Condensed Matter*, vol. 14, no. 15, R415–R451, Apr. 2002. DOI: [10.1088/0953-8984/14/15/201](https://doi.org/10.1088/0953-8984/14/15/201).
- [36] A. J. Leggett, “Realism and the physical world,” *Reports on Progress in Physics*, vol. 71, no. 2, p. 022 001, Jan. 2008. DOI: [10.1088/0034-4885/71/2/022001](https://doi.org/10.1088/0034-4885/71/2/022001).
- [37] A. V. Varma, I. Mohanty, and S. Das, “Temporal correlation beyond quantum bounds in non-hermitian PT- symmetric dynamics of a two level system,” *Journal of Physics A: Mathematical and Theoretical*, vol. 54, no. 11, p. 115 301, Feb. 2021. DOI: [10.1088/1751-8121/abde76](https://doi.org/10.1088/1751-8121/abde76).
- [38] F. Cerisola, Y. Margalit, S. Machluf, A. J. Roncaglia, J. P. Paz, and R. Folman, “Using a quantum work meter to test non-equilibrium fluctuation theorems,” *Nature Communications*, vol. 8, no. 1, Nov. 2017. DOI: [10.1038/s41467-017-01308-7](https://doi.org/10.1038/s41467-017-01308-7).
- [39] S. Deffner and A. Saxena, “Jarzynski equality in pt-symmetric quantum mechanics,” *Physical Review Letters*, vol. 114, no. 15, p. 150 601, Apr. 2015. DOI: [10.1103/physrevlett.114.150601](https://doi.org/10.1103/physrevlett.114.150601).
- [40] M. Naghiloo, J. Alonso, A. Romito, E. Lutz, and K. Murch, “Information gain and loss for a quantum maxwell’s demon,” *Physical Review Letters*, vol. 121, no. 3, p. 030 604, Jul. 2018. DOI: [10.1103/physrevlett.121.030604](https://doi.org/10.1103/physrevlett.121.030604).
- [41] A. V. Varma, J. E. Muldoon, S. Paul, Y. N. Joglekar, and S. Das, *Essential role of quantum speed limit in violation of leggett-garg inequality across a pt-transition*, 2022. DOI: [10.48550/ARXIV.2203.04991](https://doi.org/10.48550/ARXIV.2203.04991).
- [42] K. S. Agarwal, J. Muldoon, and Y. N. Joglekar, “Conserved quantities in non-hermitian systems via vectorization method,” *Acta Polytechnica*, vol. 62, no. 1, pp. 1–7, Feb. 2022. DOI: [10.14311/ap.2022.62.0001](https://doi.org/10.14311/ap.2022.62.0001).
- [43] J. Muldoon, “Floquet exceptional contours in lindblad dynamics with time-periodic drive and dissipation,” ser. Pseudo-Hermitian Hamiltonians in Quantum Physics (PTSeminar), London, United Kingdom, Sep. 2021.
- [44] J. Gunderson, J. Muldoon, K. W. Murch, and Y. N. Joglekar, “Floquet exceptional contours in lindblad dynamics with time-periodic drive and dissipation,” *Physical Review A*, vol. 103, no. 2, p. 023 718, Feb. 2021. DOI: [10.1103/physreva.103.023718](https://doi.org/10.1103/physreva.103.023718).

A. PARTIAL TRACE OPERATION

When studying the properties of physical systems it is often necessary to extract information stored in the state density operators ρ as a scalar valued function. The trace operation is defined as

$$\rho = \sum_{i,j=1}^d \rho_{ij} |i\rangle \langle j| = \sum_{j=1}^d p_j |\psi_j\rangle \langle \psi_j| \quad (\text{A.1})$$

$$\text{Tr}(\rho) = \sum_{j=1}^d \rho_{jj} = \sum_{j=1}^d p_j \quad (\text{A.2})$$

where $|j\rangle$ is a basis vector in the element-wise basis satisfying $\langle i|j\rangle = \delta_{ij}$, ρ_{ij} are the elements of the matrix ρ , $|\psi_j\rangle$ is a state in which ρ is diagonal so that p_j are probabilities, and $d = \text{rank}(\rho)$. In this way, the trace operation represents a reduction of all degrees of freedom to a single value. However, in certain circumstances it can be useful to remove some degrees of freedom while maintaining the statistical properties of the remaining system.

To accomplish this we introduce the partial trace over the degrees of freedom to be removed, for which there are two useful algorithms. If the form of ρ in Dirac notation is known, we can begin with a matrix that is separable into n distinct subspaces and write the elements of ρ as

$$\rho = \bigotimes_{m=1}^n \sum_{i,j=1}^{d_m} \rho_{j_1 j_2 \dots j_n}^{i_1 i_2 \dots i_n} |i_m\rangle \langle j_m| \quad (\text{A.3})$$

where the total rank of ρ is $D = \prod_{m=1}^n d_m$. The partial trace can then be derived from projection with respect to the dual space to $|j_l\rangle$

$$\text{Tr}_l(\rho) = \sum_{j_l=1}^{d_l} \langle\langle j_l | \rho | j_l \rangle\rangle \quad (\text{A.4})$$

which will produce a matrix with rank $D_{-l} = \prod_{m=1, \neq l}^n d_m$.

The second algorithm is more useful for computer computation. In this method ρ is reshaped into a multi-dimensional tensor so that each subspace can be addressed directly. For each element of the reduced matrix $\text{Tr}_l(\rho)$ then performs an individual trace calculation

$$\rho_{j_1 j_2 \dots j_{l-1} j_{l+1} \dots j_n}^{i_1 i_2 \dots i_{l-1} i_{l+1} \dots i_n} = \sum_{j_l=1}^{d_l} \rho_{j_1 j_2 \dots j_l \dots j_n}^{i_1 i_2 \dots j_l \dots i_n} \quad (\text{A.5})$$

either by direct summation or by reshaping a matrix constructed from all elements matching $i_m \neq i_l$ and $j_m \neq j_l$.

VITA

Jacob E. Muldoon

(317)429-6014

jemuldo@iupui.edu

5268 Ivy Hill Drive Carmel, IN 46033

Institution:

Department of Physics, LD 154
Indiana University Purdue University of Indianapolis (IUPUI)
402 N. Blackford Street, Indianapolis, IN 46202

Research Interests: PT Symmetry, Lindbladian Evolution, Quantum Maps, Non-Linear Analysis, Condensed Matter, Superconducting Circuits, Qudits & Quantum Information, Machine Learning

Education

Ph.D. (Physics)	(IUPUI), Ongoing
M.S. (Physics)	(IUPUI), May 2018
B.S. (Physics)	(IUPUI), May 2015
B.S. (Chemistry)	(IUPUI), December 2015

Professional & Teaching Experience

Research Assistant	Department of Physics (IUPUI), 2021 – Present
PT Symmetry Division Meeting Organizer	Department of Physics (IUPUI), 2020 - Present
SEED & STEM Program Mentor	Department of Physics (IUPUI), 2019 - Present
Recitation Leader	Department of Physics (IUPUI), 2019 - 2019
Laboratory Instructor	Department of Physics (IUPUI), 2017 - 2019
Physics Tutor	Department of Physics (IUPUI), 2014 - 2017
Laboratory Technician	Department of Physics (IUPUI), 2013 – 2014

Publications & Conferences

1. A. V. Varma, J. E. Muldoon, S. Paul, *et al.*, *Essential role of quantum speed limit in violation of leggett-garg inequality across a pt-transition*, 2022. DOI: [10.48550/ARXIV.2203.04991](https://doi.org/10.48550/ARXIV.2203.04991)
2. K. S. Agarwal, J. Muldoon, and Y. N. Joglekar, “Conserved quantities in non-hermitian systems via vectorization method,” *Acta Polytechnica*, vol. 62, no. 1, pp. 1–7, Feb. 2022. DOI: [10.14311/ap.2022.62.0001](https://doi.org/10.14311/ap.2022.62.0001)
3. J. Muldoon, “Floquet exceptional contours in lindblad dynamics with time-periodic drive and dissipation,” ser. Pseudo-Hermitian Hamiltonians in Quantum Physics (PTSeminar), London, United Kingdom, Sep. 2021
4. J. Gunderson, J. Muldoon, K. W. Murch, *et al.*, “Floquet exceptional contours in lindblad dynamics with time-periodic drive and dissipation,” *Physical Review A*, vol. 103, no. 2, p. 023 718, Feb. 2021. DOI: [10.1103/physreva.103.023718](https://doi.org/10.1103/physreva.103.023718)

Grants & Awards

(IUPUI) School of Science Outstanding Graduate Student Award	Spring 2022
(IUPUI) School of Science Dean's List, Fall 2011	Spring 2015
(IUPUI) School of Science Scholar's List Recipient	Fall 2011 – Spring 2015
(IUPUI) Honors College Member	Fall 2011 – Spring 2015
(BSA) Eagle Scout Award	October 2011